OBSERVATIONS OF THE RAYLEIGH-TAYLOR INSTABILITY IN LASER ACCELERATED TARGETS

by

Justin Stephen Wark

April 1985

A thesis submitted for the Degree of Doctor of Philosophy of the University of London and the Diploma of Membership of Imperial College.

The Blackett Laboratory
Imperial College of Science and Technology
London SW7 2BZ

ABSTRACT:

Non-uniformities in the laser irradiation of spherical targets at intensities of ~10^{14}W cm^{-2} have been measured for six beam illumination with f/1 optics. The optimum experimental focusing conditions are compared with analytical and computational models.

Variations in ρr have been observed in laser accelerated foils; it is shown that the instabilities grew from inhomogeneities in the drive beams caused by inherent defects in the final lenses. The observed amplitudes are compared with two dimensional hydrodynamic simulations.

The first observations of the R-T instability in ablatively accelerated mass-modulated microballoons have been recorded. Direct evidence of mass redistribution has been observed; the results are again compared with simulations.

The use of monoenergetic fusion produced alpha particles as a backlight for laser-driven targets is discussed, and the technique compared with the conventional method of X-ray backlighting. The results of a short experimental feasibility study are given.

Point projection spectrally resolved x-ray backlighting has been used to observe ablatively driven targets. The spatial resolution and effect of self emission from the target are discussed.

To my parents

Acknowledgements

I would like to thank my Supervisor, Dr.J.D.Kilkenny, for his valuable encouragement and guidance throughout the course of this work.

Thanks are also due to all those people, both in the Plasma Physics Group at Imperial College, and at the Rutherford Appleton Laboratory, with whom I have had many helpful discussions: most notably Deryck Bond and Brian MacGowan at Imperial College, and Roger Evans, Adrian Cole, Steve Rose, Tony Bell, Mike Key and Bill Toner at the Rutherford Laboratory.

The support of the Laser Operators, Target Area and Target Fabrication staff at the CLF is greatly appreciated, as is the help of the staff of the Laser System 'Phoenix' at the Lawrence Livermore National Laboratory, USA.

During the course of this work I was financed by the Science and Engineering Research Council.

Finally I wish to thank my wife, Tina, and my parents (to whom this thesis is dedicated), for their constant love, support and encouragement.

CONTENTS

Page

Title Page 1
Abstract 2
Dedication 3
Acknowledgements 4
Contents 5
List of Figures 8

CHAPTER ONE : INTRODUCTION

1.1 The D-T reaction 11
1.2 The Lawson criterion 12
1.3 The need for high density 13
1.4 Ablation pressure 14
1.5 The critical surface 15
1.6 Absorption of Laser light 17
1.7 Thermal smoothing 18
1.8 Illumination uniformity 19
1.9 The Rayleigh-Taylor instability 21
1.10 The Central Laser Facility 22
1.11 Role of the author/Outline of the thesis 22

CHAPTER TWO: UNIFORMITY OF ILLUMINATION

2.1 Introduction 26
2.2 Previous work 26
2.3 Experimental set up 27
2.4 Targets 27
2.5 Pinhole camera filtering 29
2.6 Illumination conditions 29
2.7 Calorimetry 31
2.8 Results 31
2.9 Quantitative results 33
2.10 X-ray shadowgraphy of implosions 45
2.11 Absorption results 45
2.12 Theoretical calculations 48
2.13 The absorption model 49
2.14 The inverse square distribution 50
2.15 Absorbed fraction 55
2.16 Computer simulation of uniformity 55
2.17 The ray-tracing subroutine 56
2.18 Results from Medusa 57
2.19 Discussion 57
2.20 Conclusion 58

CHAPTER THREE: X-RAY BACKLIGHTING OF R-T UNSTABLE FOILS

3.1 Introduction 59
3.2 Relevance to ICF 63
3.3 Breakdown of classical theory 64
3.4 The Kelvin-Helmholtz instability 68
3.5 Previous experimental measurements 68
3.6 Experiments 70
3.7 X-ray backlighting of plastic foils 71
3.8 Backlighting spectrum 72
3.9 Distance moved by the target 76
3.10 Results 77
3.11 Hydrocode simulation 85
3.12 Discussion 87
3.13 Conclusion 88

CHAPTER FOUR: THE R-T INSTABILITY IN IMPLODING MICROBALLOONS

4.1 Introduction 89
4.2 Targets 89
4.3 The experimental set up 91
4.4 Results 94
4.5 Comparison with Cole's results 100
4.6 Computer simulation 108
4.7 Limits on aspect ratio 108
4.8 Conclusion 114

CHAPTER FIVE: ALPHA PARTICLE BACKLIGHTING

5.1 Introduction 115
5.2 The concept of alpha particle backlighting 116
5.3 The CR39 plastic track detector 118
5.4 Experimental set up 119
5.5 Temporal resolution 123
5.6 Spatial resolution 124
5.7 Range as a function of temperature and density 127
5.8 Anisotropy in the parent distribution 134
5.9 Experimental results 136
5.10 The corrugated target spectrum 140
5.11 The plane target spectrum 140
5.12 Comparison of the two results 141
5.13 Conclusion 142

CHAPTER SIX: POINT PROJECTION RADIOGRAPHY OF FOILS

6.1 Introduction 144
6.2 Previous work 145
6.3 Comparison of extended and point source backlights 145
6.4 Experiments 148
6.5 The RAL experiment 148

6.6 Experimental set up 150
6.7 Resolution 151
6.8 Results 154
6.9 The Livermore experiment 158
6.10 Illumination conditions 161
6.11 Magnification 161
6.12 Resolution of unirradiated targets 161
6.13 Results 163
6.14 The backlighting spectrum 166
6.15 Conclusion 166

CHAPTER SEVEN: CONCLUSIONS AND SUGGESTIONS FOR FURTHER WORK 168

References 172

LIST OF FIGURES

(1.1) Reaction rates as a function of ion temperature.
(1.2) Compilation of planar and spherical mass ablation rate data.
(1.3) Thermal smoothing as a function of intensity for 1.05μm and 0.53μm light.
(1.4) The Vulcan Laser system.
(1.5) The six beam target chamber.

(2.1) Position of Pinhole camera showing overlaps visible on the surface of the microsphere.
(2.2) The defocusing parameter.
(2.3) Average x-ray yield versus plastic thickness.
(2.4) Typical pinhole pictures after colour enhancement.
(2.5) One dimensional scan through pinhole image showing the inner and outer radii of the limb.
(2.6) Uniformity as a function of defocus.
(2.7) Uniformity as a function of beam balance.
(2.8) Variations in mass ablation rate around the horizon of the microsphere.
(2.9) X-Ray shadowgraph of an imploding microballoon.
(2.10) Absorbed fraction as a function of defocus.
(2.11) Medusa and inverse square electron density distribution as a function of radius.
(2.12) Geometry used by Ross to calculate deposition via inverse bremsstrahlung for the inverse square distribution.
(2.13) Energy deposition as a function of radius at different overlap positions for the inverse square model.

(3.1) The classical Rayleigh-Taylor instability.
(3.2) Typical pressure and density profiles for a laser irradiated target.
(3.3) Density profile used by Colombant and Manheimer.
(3.4) Reduction in growth rate due to density profile.
(3.5) Experimental arrangement for the backlighting of plastic foils.
(3.6) A typical mass modulated foil.
(3.7) The copper backlighting spectrum.
(3.8) Results from the filter pack measurements.
(3.9) Distance moved by the target.
(3.10) Shadowgraphs of the driven foils.
(3.11) Beam profile through the f/1 lens.
(3.12) Target showing self emission.
(3.13) The intensity distribution used in the code run.
(3.14) Variation in ρr predicted by the hydrocode.

(4.1) A mass modulated microballoon.
(4.2) Microballoon with back removed.
(4.3) Experimental arrangement for the backlighting of mass modulated microballoons
(4.4) Densitometer trace of a streak camera picture of x-rays from the backlighting and drive pulses.
(4.5) The x-ray shadowgraphs of imploded mass modulated microballoons.
(4.6) An unmodulated irradiated hemisphere showing time smearing at the irradiated edge.
(4.7) Average spike amplitudes plotted as a function of the square root of the distance moved.
(4.8) Increase of shell thickness due to incompressibility.
(4.9) Experimental arrangement for the transmission measurement.
(4.10) Transmission result showing a horizontal bar corresponding to a R-T spike.
(4.11) Density contours at different times from the 2-D code 'Pollux'.
(4.12) Aspect ratio as a function of effective initial perturbation.

(5.1) The basic concept of alpha particle backlighting to detect the R-T instability.
(5.2) The shape of a typical etched track with the parameters by which the alpha particle energy may be determined.
(5.3) Experimental set up for the alpha particle backlighting of laser irradiated targets.
(5.4) Resolution due to multiple coulomb scattering.
(5.5) The stopping power of Aluminium to alpha particles for various densities and temperatures.
(5.6) Range in CR39 as a function of incident alpha particle energy.
(5.7) Thickness of Al foil as a function of exit energy of the alpha particle
(5.8) Error in measured ρr as a function of time for the Al run.
(5.9) Error in measured ρr as a function of time for the CH run.
(5.10) Fractional error in $\Delta(\rho r)$ as a function of $\Delta(\rho r)$ due to realistic density and temperature gradients.
(5.11) Arrangement for measuring the parent distribution on the same piece of CR39 as the foil distribution.
(5.12) Alpha particle range spectrum for the $3\mu m$ corrugated Al foil.
(5.13) Alpha particle range spectrum for the $3\mu m$ plane foil.
(5.14) Variation in thickness for the two foils.

(6.1) The concept of point projection backlighting.
(6.2) First order estimate of refraction effects for point

and extended sources.
(6.3) Experimental set up for the Rutherford point projection experiment.
(6.4) Shadow of the resolution grid in the Bi spectrum.
(6.5) Intensity of the point source as a function of distance.
(6.6) Shadow of an unirradiated 10μm thick plastic foil.
(6.7) Shadow af the irradiated foil probed at 5ns after the onset of the drive pulse.
(6.8) Target design for observing a thin absorbing region of the target.
(6.9) Shadowgraph of the irradiated target shown in Fig(6.8).
(6.10) Target design for the Livermore experiment.
(6.11) A plan view of the Livermore experiment.
(6.12) Shadowgraph of the grid.
(6.13) Backlit unirradiated target showing absorption at the Cl K edge.
(6.14) Irradiated target showing the effects of refraction of the x-rays.
(6.15) Irradiated target showing Cl emission lines.

CHAPTER ONE

INTRODUCTION

Abstract

One day Inertial Confinement Fusion (I.C.F.) may provide a clean, safe and abundant source of nuclear energy. However the scientific and technological problems still opposing the realisation of this goal are formidable. In this chapter the basic concepts of I.C.F. will be outlined along with some of the associated difficulties, in order to provide a backdrop to the experimental work described later and to show the relevance of that work to I.C.F and the more general field of the physics of the compression of matter to high densities.

1.1 The D-T Reaction

The Maxwellian-averaged reaction rates for the principle isotopes of interest to I.C.F. applications (1.1) (1.2) are plotted as a function of ion temperature in Fig(1.1). The fusion reaction with the largest cross section is the Deuterium - Tritium reaction:

$$D + T \rightarrow \alpha\ (3.5\ \text{Mev}) + n\ (14.1\ \text{Mev}) \qquad (1.1)$$

where the 17.6 Mev reaction energy is divided between a 3.5 Mev alpha particle and a 14.1 Mev neutron. Therefore this particular reaction has received most attention in fusion research.

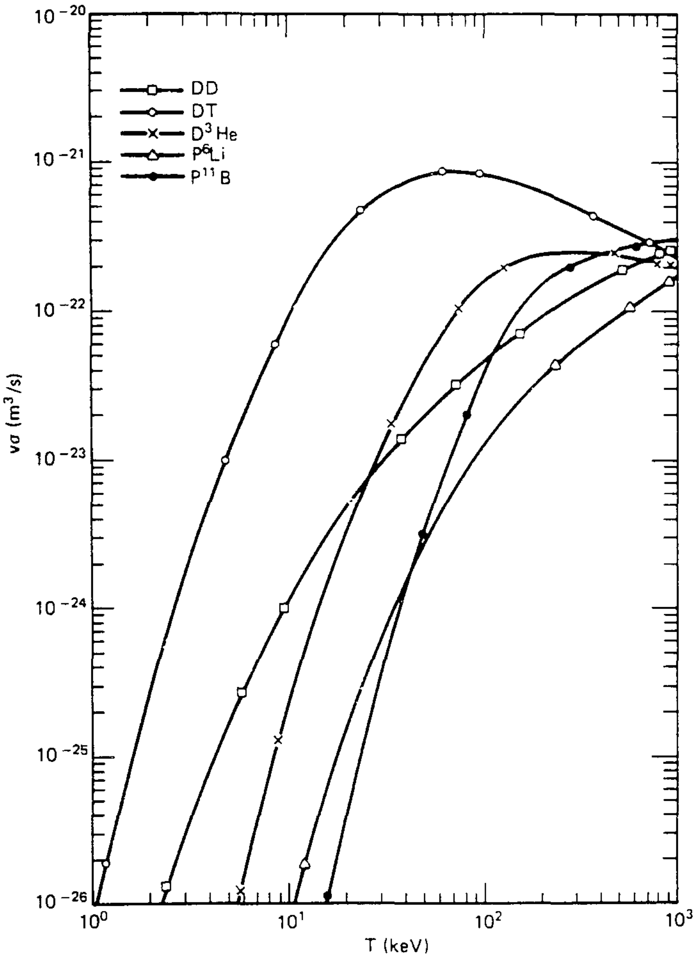

Fig(1.1) Reaction rates as a function of ion temperature from ref$^{(1.2)}$.

1.2 The Lawson Criterion

In order to achieve energy gain the reacting nuclei must be confined long enough for a sufficient number of them to fuse together. The fusion energy released per unit volume, E_f, in a D-T reaction can be written as:

$$E_f = n_d n_t \langle \nu\sigma \rangle W\tau \qquad (1.2)$$

where n is the number density of ions, $\langle \nu\sigma \rangle$ the Maxwellian averaged reaction rate, W the energy released per reaction, and τ the confinement time.

Therefore assuming $n_d=n_t=n/2$

$$E_f = n^2 \langle \nu\sigma \rangle W\tau/4 \qquad (1.3)$$

We can ignore energy losses due to radiation to first order; as the thermonuclear burn typically would occur at 20 to 100 Kev. The energy required to heat the fuel to thermonuclear temperature, E_t, is given by:

$$E_t = (3/2)nkT_i + (3/2)nkT_e = 3nkT \qquad (1.4)$$

(assuming $T_i=T_e$ for convenience)

For energy gain we have the condition $E_f > E_t$

$$\text{i.e } n\tau > 12kT/\langle \nu\sigma \rangle W \qquad (1.5)$$

This condition is known as the Lawson criterion (1.3) . At a temperature of 10 Kev for DT we require $n\tau > 10^{14} s/cm^3$.

1.3 The Need for High Density

The basic concept of I.C.F is to implode the fuel to such high densities that the thermonuclear reaction time is less than the target dissassembly time; i.e. the fuel is confined by its own inertia. This places a condition on the product of the fuel density, ρ, and the radius r (1.4).

The dissassembly time, τ_d, for a freely expanding sphere of radius r is (1.5)

$$\tau_d \simeq r/4c_s \qquad (1.6)$$

where c_s is the speed of sound in the pellet. The number density is

$$n = \rho/m_i \qquad (1.7)$$

where m_i is the ion mass. Therefore the Lawson criterion becomes

$$n\tau = \rho r/4c_s m_i > 10^{14} s/cm^3 \qquad (1.8)$$

which at 10 Kev yields $\rho r \sim 0.6$ g/cm^2.

We now estimate the driver energy required to achieve fusion at such densities. Substituting (1.6) into (1.3) we obtain:

$$E_f = n^2 \langle v\sigma \rangle Wr / 16c_s = E_t = 3nkT \qquad (1.9)$$

solving for r:

$$r = (kTc_s/n\langle v\sigma \rangle W)48 \qquad (1.10)$$

The total driver energy per pellet, E_d, is given by

$$E_d = (4\pi r^3/3)E_f \qquad (1.11)$$

substituting (1.9) and (1.10) into (1.11) we obtain

$$E_d = 4\pi(48)^3(kTc_s/n\langle v\sigma \rangle W)^3 nkT$$
$$= 2.2 \times 10^{12}/\eta^2 \text{ J} \qquad (1.12)$$

where $\eta = n/n_0$ (n_0 is the density of liquid D-T).

We see that with this very simplified model we would require a driver energy of over 10^6 MJ; over a factor of 10^7 greater than any driver in existence! But the driver energy scales as the inverse square of the compression: if we could compress the fuel by a factor of 10^4 then we would only need 22 KJ (using this simple model), i.e. within the capabilities of present driver systems. Hence to achieve I.C.F. with existing driver technology, we need to compress the fuel to very high densities.

1.4 Ablation Pressure

The pressure required for a given fuel compression is at a minimum for an isentropic compression and is given by (1.6) :

$$P \simeq (2n_e\varepsilon_f/3)\left[3/5 + (\pi kT/2\varepsilon_f)^2 + ...\right] \qquad (1.13)$$

where ε_f is the Fermi energy. For fuel compressed by a factor of 10^4 at $\simeq$ 5 Kev, $P \simeq 10^{13}$atm.

The idea of I.C.F. is to achieve such high pressures by using a laser (or ion) beam to heat the surface of a hollow sphere containing the D-T fuel. The surface of the sphere rapidly ionizes and ablates off into the surrounding vacuum, imploding the remaining shell and the fuel contained in it; i.e. it acts like a spherical rocket.

Much work(1.7)(1.8)(1.9)(1.10)has been done to measure mass ablation rates, and hence ablation pressures, in both planar and spherical geometry. The pressure has been found to be greater for shorter wavelength light for a given incident irradiance as shown in Fig(1.2). The final pressure of the D-T fuel can be significantly amplified above the ablation pressure (of the order 10 to 100 Mbar) as the result of the acceleration of the imploding shell to high velocity.

1.5 The Critical Surface

The imploding pellet is surrounded by ionized ablating material forming a plasma atmosphere with solid density at the ablation surface, becoming less dense as it expands into the surrounding vacuum. The refractive index of a plasma, μ, is given by:

$$\mu = \left[1-(\omega_p/\omega)^2\right]^{1/2} \qquad (1.14)$$

where ω_p, the plasma frequency is given by:

$$\omega_p{}^2 = n_e e^2/\varepsilon_0 m_e \qquad (1.15)$$

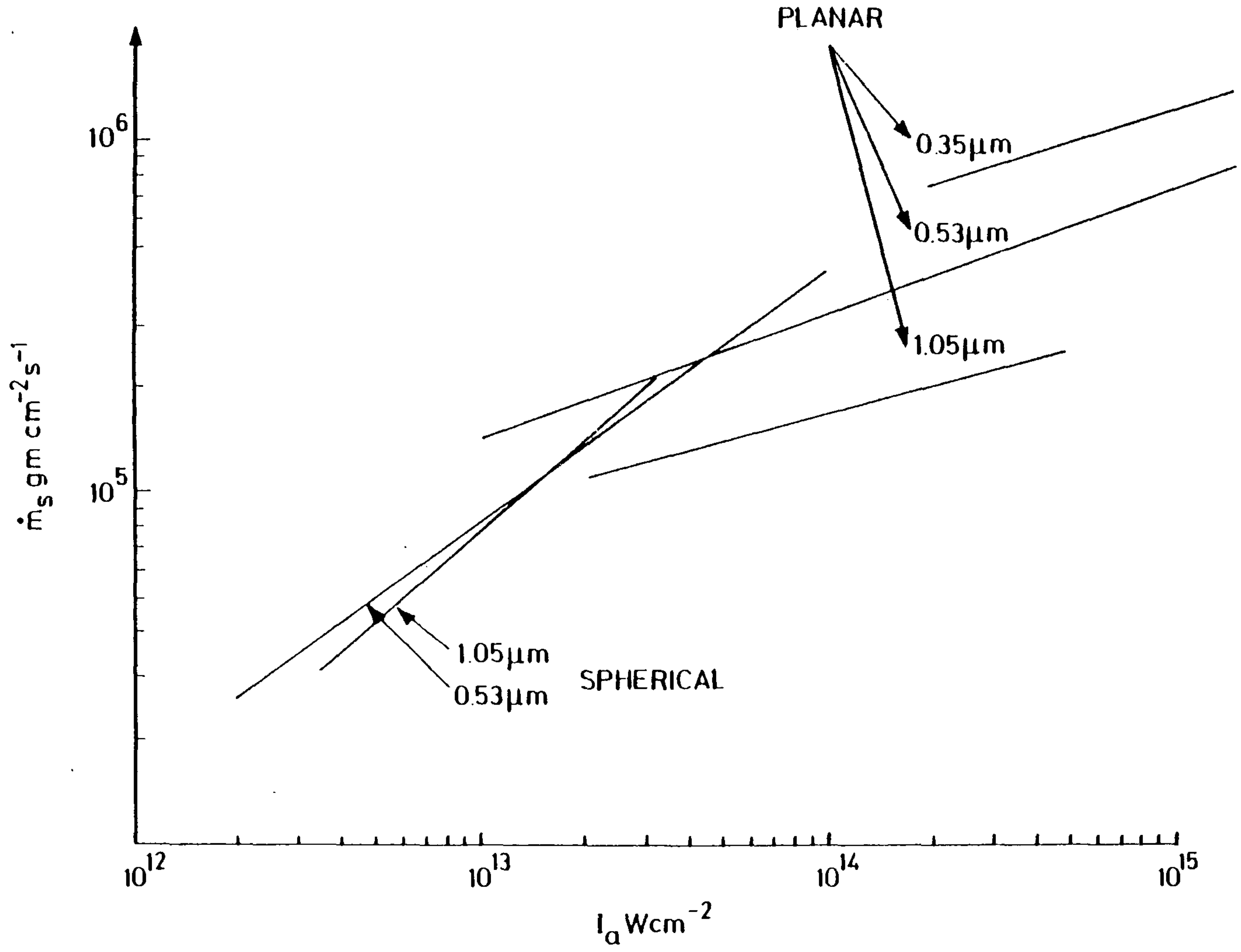

Fig(1.2) Compilation of planar and spherical geometry mass ablation rate data as a function of absorbed irradiance from refs (1.8) and (1.9). The absorbed fraction is greater at shorter wavelengths, and thus the mass ablation rate higher for a given incident irradiance.

and ω is the frequency of the incident laser light.

Therefore the light can only penetrate the plasma when

$$n_e < \omega\varepsilon_0 m_e/e^2$$

The surface corresponding to $n_e=n_c=(\omega\varepsilon_0 m_e/e^2)$ is known as the critical surface, and n_c is the critical density; the incident laser light will be reflected at or before the critical surface.

1.6 Absorption of Laser Light

The two main mechanisms by which the laser energy is absorbed are inverse bremsstrahlung and resonance absorption (and to a lesser extent, parametric instabilities).

i)Inverse bremsstrahlung: An electron in binary collision with an ion can absorb a photon(1.11). The absorption coefficient κ may be written:

$$\kappa = \frac{10^6 \times \rho^2 Z \lambda^2(\mu m)}{[kT(Kev)]^{3/2}[1-\rho/\rho_c]^{1/2}} \quad cm^{-1} \qquad (1.16)$$

i.e. most collisional absorption takes place as $\rho \to \rho_c$, where ρ_c is the critical density.

ii)Resonance absorption: Resonance absorption of laser energy takes place when the electric field of the laser drives an electrostatic plasma wave at the critical surface. Wave-breaking causes the energy to be transferred to a relatively small number of surrounding electrons, which can attain energies of an order of magnitude greater than the typical plasma electrons(1.12)(1.13) ; such electrons have been named hot or fast electrons.

If the laser light is incident at an angle θ to the electron density gradient it is refracted through the plasma atmosphere and is reflected at a density $n_c \cos^2\theta$ (in planar geometry), i.e. it never reaches the critical surface. However Freidberg et al(1.14) have shown that if the light has a p polarised component of $\underline{E}$ on reflection the $\underline{E}$ field can tunnel through to the critical surface and so still cause resonance absorption.

The temperature of the hot electrons has been found to scale as $(I\lambda^2)^x$ (1.15)(1.16), where the exponent has been found to be within 0.25 and 0.33. The fraction of energy coupled into the hot electrons falls off rapidly with increasing pulse length (1.17) and is negligible for the pulse lengths and irradiances relevant to the work described in this thesis. However, under extreme conditions the hot electrons can penetrate the shell of the target, preheating the fuel. This increases the entropy of the fuel and hence limits the achievable density, degrading the compression. Preheat due to hot electrons and x-rays from the ablation surface is one of the major problems in I.C.F.

1.7 Thermal Smoothing

The absorbed energy is deposited up to and outside of the critical surface. From there it is transported by thermal conduction to the ablation surface. Due to the finite number of laser beams used, and hot spots in those beams, the energy deposition will not be totally symmetric.

However, between the critical and ablation surfaces some lateral thermal transport will take place, smoothing out any inhomogeneities.

Thermal smoothing has been investigated by several workers using different methods (1.18)(1.19)(1.20) and has been found to be most effective for long wavelength incident light at high intensities, as shown in Fig(1.3). This is due to the larger distance between the ablation and critical surfaces for longer wavelengths.

However, as noted in section (1.4), the ablation pressure decreases with increasing wavelength; the optimum laser wavelength will be a complex function of realistic values of ablation pressure, thermal smoothing, illumination uniformity (as related to the required number of beams) and other restrictions on the optics.

1.8 Illumination Uniformity

An isentropic compression requires a spherically symmetric drive pressure. For instance, to achieve a compression ratio of 10^4, the radius of the target must decrease by a factor of 22. If we require the final shell to be uniform over a scale length of half the final radius then the initial drive uniformity should be better than ±2 %.

This restraint on drive uniformity puts conditions on the illumination uniformity - which is in turn a function of the number of laser beams used and their focusing conditions. This will be discussed more fully in chapter 2

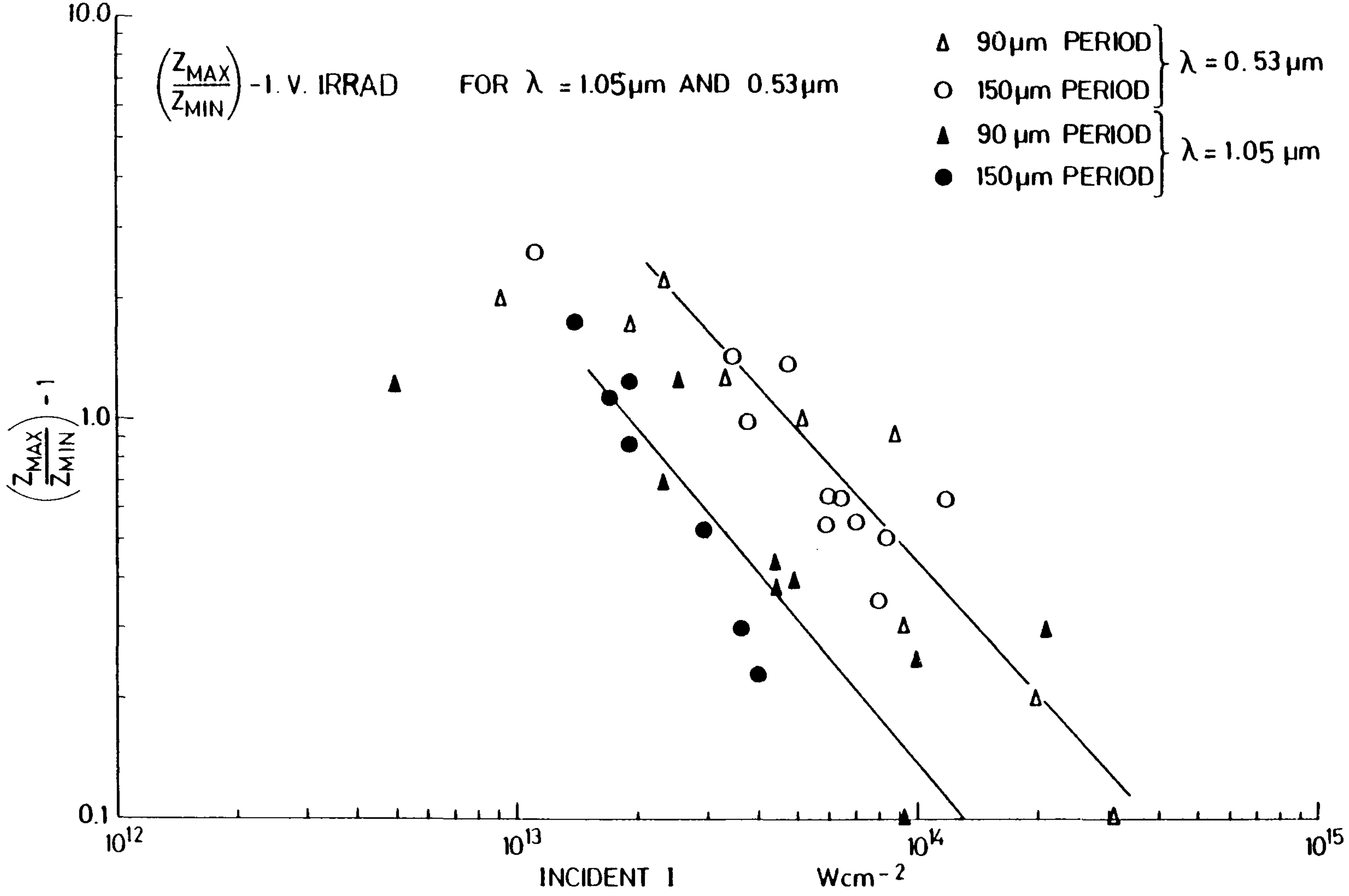

Fig(1.3) Thermal smoothing as a function of intensity for 1.05 and 0.53μm light from ref (1.21).
Foils were irradiated with a spatially periodic irradiance of wavelength λ. Z_{max} and Z_{min} are the maximum and minimum distances travelled by the rear surface of the target at a set time after the onset of acceleration.

and forms part of the experimental work described in this thesis.

1.9 The Rayleigh-Taylor Instability

The classical Rayleigh-Taylor (R-T) instabilty (3.1) (3.2) takes place in a fluid when the density and pressure gradients are opposed; e.g. a heavy fluid on top of a light fluid in a gravitational field.

The pressure and density profiles of a typical target irradiated with a high power laser beam are shown in Fig(3.2). It can be seen that there is a small region at the ablation surface in which the pressure and density gradients are opposed and the target is R-T unstable.

The classical R-T growth rate, γ_c, of any small amplitude perturbations between two fluids of densities ρ_1 and ρ_2 ($\rho_1 > \rho_2$) under an effective acceleration a is

$$\gamma_c = \surd(A\ ka) \qquad (1.17)$$

where $A = (\rho_1+\rho_2)/(\rho_1-\rho_2)$ the Attwood number, and k is the wavenumber of the perturbation. The amplitude at time t is

$$A = A_0 e^{\gamma\ t} \qquad (1.18)$$

where A_0 is the amplitude of the initial perturbation. The accelerations involved in I.C.F. are extremely high. typically $\sim 10^{16}$cm/s^2, and so during a 1ns laser pulse γt could be in the range ~ 8 for a perturbation of wavelength 10µm. The R-T instability thus disrupts the symmetry of the implosion and it may even break up the shell before peak compression occurs.

Measurement of R-T growth rates in I.C.F. targets is therefore of great importance - and such measurements form the major part of the experimental work described in this thesis.

1.10 The Central Laser Facility

The experimental work described in this thesis was performed at the Science and Engineering Research Councils Central Laser Facility at the Rutherford Appleton Laboratory. The C.L.F. houses the multiwavelength, multiterrawatt, variable pulse length Neodymium glass laser VULCAN. This laser can deliver 150 J of 1.05 μm light into each of six beams in a pulse of ≈ 1ns, or 50J per beam in 70ps. The infra-red can be frequency doubled (0.53 μm) with an efficiency of up to 50%.

The laser is shown in Fig(1.4) and the six beam target chamber in Fig(1.5). The details of the experimental set ups will be discussed more fully in the appropriate chapters.

1.11 Role of the Author/Outline of the Thesis

Chapter Two describes an experiment to measure the uniformity of illumination in six beam f/1 geometry for 0.53μm ablative implosions. The data collection and analysis in this experiment were entirely the work of the author.

Chapter three describes the observation of ring like structures in ablatively driven planar foils. The measurements of the rings in the beams were made by Dr. R. Eason. Whilst acknowledging the great practical help of Dr. A.J.Cole, it must be said that the data collection and analysis was essentially performed by the author.

The experiment discussed in chapter four describes the first direct observation of the R-T instability in mass modulated ablatively driven microballoons, again this is solely the work of the author with practical help from Dr.A.J.Cole.

Chapter five includes a discussion of the concept of monoenergetic alpha particle backlighting. Although the original idea to use alpha particles as a backlight was conceived by W.Toner of RAL, the discussion of the factors determining the spatial and temporal resolution and experimental conditions are the work of the author. The chapter also describes a feasibility study of the technique performed by the author with practical help from Dr.P.Fews and W.Toner. The measurements of the track lengths in CR39 were performed by Dr.P.Fews, and the calculations of the stopping power of Aluminium and Plastic as a function of density and temperature were carried out by Dr.S.Rose from RAL. The subsequent data analysis and conclusions are the work of the author.

Chapter six describes the use of a point source of x-rays as a backlight for laser accelerated targets. The spatial resolution afforded by such a source is presented and problems due to self emission from the target discussed. The work described was performed by the author with practical help from Dr A.J.Cole and Dr O.Landen.

Chapter seven acts as a conclusion to the thesis; the ideas and suggestions for further work belong entirely to the author.

Fig(1.4) The Vulcan Laser system showing the six final amplifiers.

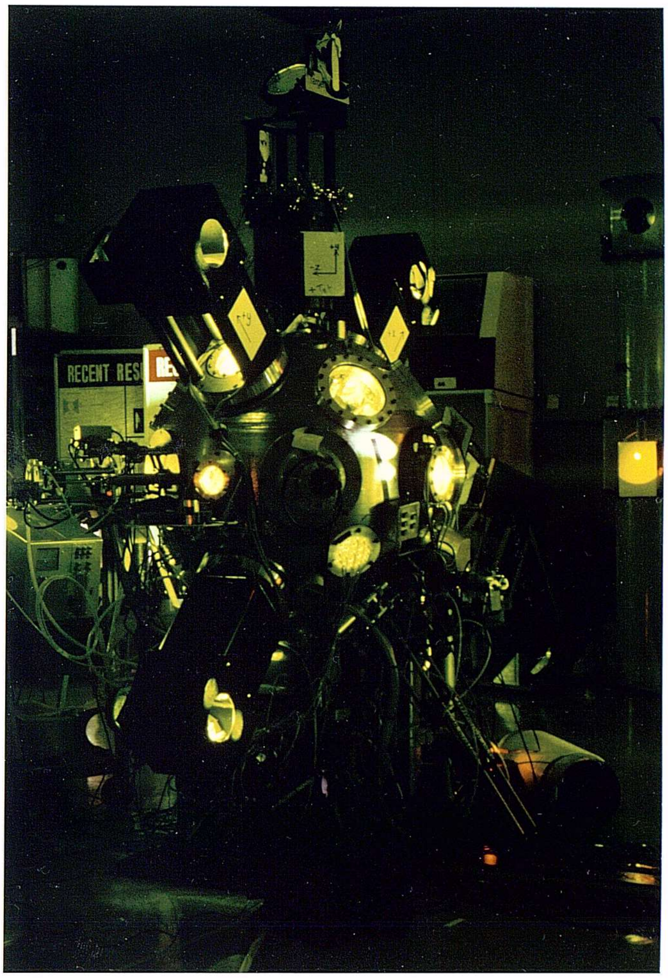

Fig(1.5) The six beam target chamber at the CLF.

CHAPTER TWO

UNIFORMITY OF ILLUMINATION

Abstract

For energy gain in I.C.F. at modest drive energy high compression ratios are needed; therefore the drive pressure must possess a high degree of spherical symmetry. This chapter describes measurements of the uniformity of mass ablation rate in six beam geometry with f/1 optics. The observed higher ablation rate at triple beam overlaps is shown to agree qualitatively with simple inverse bremsstrahlung absorption models and with the 1-D Lagrangian code "Medusa" employing raytracing.

2.1 Introduction

The relationship between the uniformity of illumination and the drive uniformity is a complex one: first the laser light is refracted through the underdense plasma atmosphere, depositing energy via inverse bremsstrahlung, undergoing refractive smoothing(2.1); secondly, resonance absorption will take place on reflection which dominates inverse bremsstrahlung at high incident irradiances. Both the thermal and refractive smoothing should mean that constraints on the illumination uniformity may be less severe than first appearances suggest.

2.2 Previous work

A qualitative experimental study of the uniformity of illumination has been carried out by Rumsby[2.2] at the CLF using 1.06μm light. They found that the uniformity (judged from X-Ray pinhole pictures) improved if the beams were defocused so as to overlap each other on the target surface.

More quantative work performed at the University of Rochester[2.3] shows that uniformities of 20% can be achieved with six beams using 1.06μm light and f/4 optics.

The aim of the work described here was to measure the uniformity for six beam illumination with the f/1 optics at the CLF as a function of defocus. This would give information on the optimum focusing conditions for subsequent implosion experiments as well as giving experimental input for theoretical investigations of uniformity as a function of the number of beams etc.

2.3 Experimental set-up

The uniformity was studied by recording the variation in brightness of x-rays emitted from irradiated microspheres. The x-ray images were recorded on Kodak "No screen" film using a pinhole camera with a 10μm pinhole in 15μm Pt. The camera was positioned half way between two of the six orthogonal beams; thus on the horizon of the microsphere were both double and triple beam overlap positions, as well as two single beams, as shown in Fig(2.1). This camera position was chosen as it gave maximum information about the variation in ablation rates.

2.4 Targets

The targets used were solid glass microspheres of 150

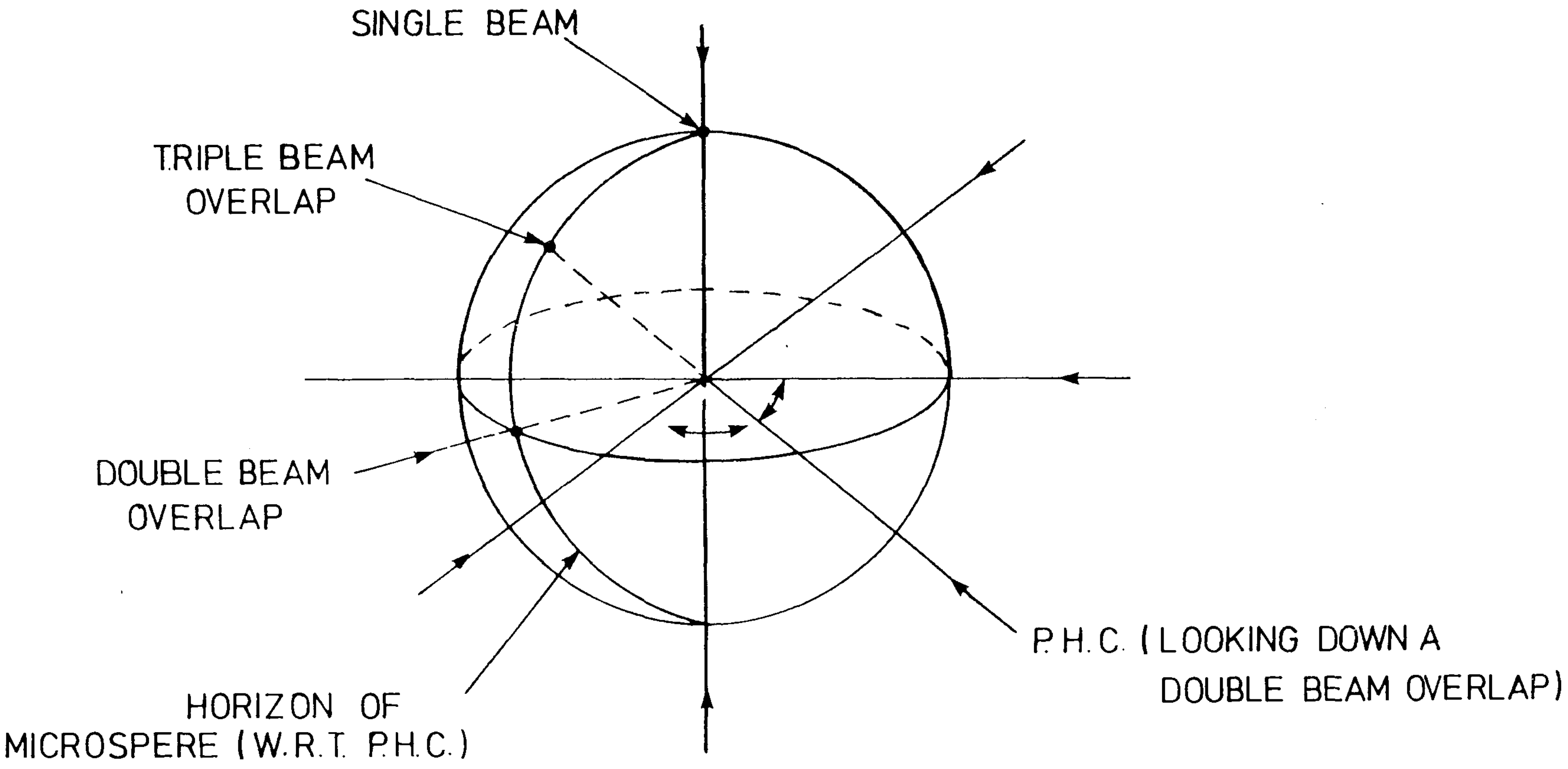

Fig(2.1) The position of the pinhole camera showing the overlaps visible on the horizon of the target.

- 200 μm diameter, coated with various thicknesses (3 - 6 μm) of plastic. Solid targets were used so that the ablation surface (where most of the x-rays in the spectral range of observation were produced) moved a relatively short distance during the laser pulse; whereas the implosion of a hollow target would confuse the analysis of the uniformity due to the time smearing of x-rays from the ablation surface. Thus the images consisted of a well defined limb-broadened ring. The glass targets were coated with plastic in order to enhance the effect of any non-uniformities in the mass ablation rate. In the regions of higher ablation rate the plastic would be ablated more quickly, revealing the brighter x-ray source of the glass.

2.5 Pinhole Camera Filtering

Filtering of 15 μm of Berylium was used to filter out the soft x-rays (this thickness of Be has a 1/e absorption coefficient at an x-ray energy of 1.2Kev). Over this was placed 5 μm of Aluminium, the k edge of Al is at 7.95Å (1.49Kev) thus it supressed the relatively long lived Si He-α which would persist into the corona.

2.6 Illumination Conditions

The targets were irradiated with 200 J of 0.53 μm light in a pulse length (FWHM) of 0.6 ns. The beams were focused at a variable distance D beyond the target to study the effect of defocusing on the uniformity. The focusing can thus be defined in terms of the parameter D/R, where R is the target radius. For an f/1 lens, as used here, the

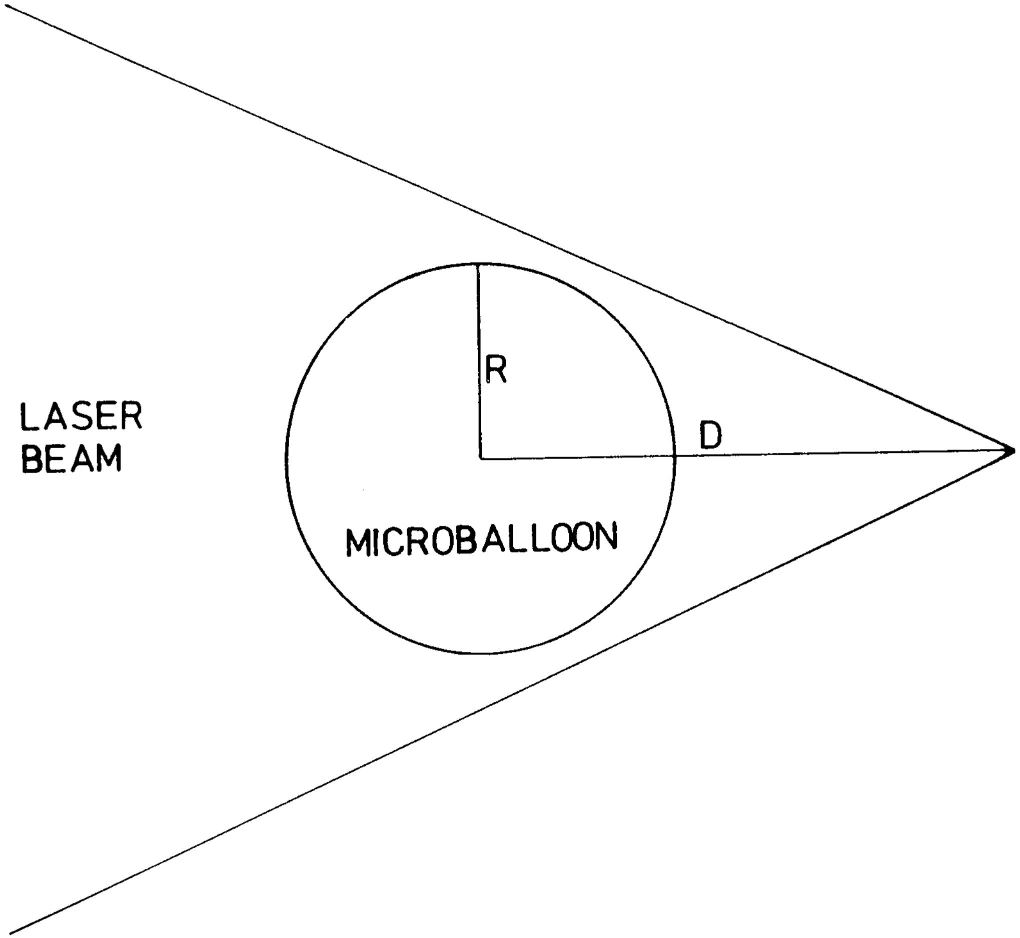

Fig(2.2) The defocusing parameter D/R.

target just obscures all of the beam at a defocus of 2.25 as shown in Fig(2.2) .

2.7 Calorimetry

The absorbed energy was measured using six ion calorimeters. These were placed around the chamber at double, triple and intermediate overlap positions. The random error was found to be ± 10% of the measured reading.

The energy in each beam is measured by splitting a small known fraction of the drive beam using a partially transmitting mirror, onto a calorimeter. The absorbed fraction is simply calculated from these two calorimetry measurements.

2.8 Results

Over 15 shots were fired, the beams being focused between 3.0 and 5.5 target radii beyond the target, at typical incident irradiances of $2 \rightarrow 5\times10^{14}$ $\mathrm{Wcm^{-2}}$. To obtain quantative information about uniformity it is necessary to know the relative brightness of x-rays produced from the glass and plastic with the filtering used. Fig(2.3) shows average relative x-ray yields against plastic thickness for shots with similar absorbed irradiances. With 6 μm of plastic, burn through to the glass is not achieved; and it is not until the plastic thickness is reduced to 4 μm that the x-ray yield increases due to glass x-rays. From this we can estimate the average mass ablation rate to be $\simeq 7\times10^{5}$gm $\mathrm{cm^{-2}s^{-1}}$, which is about 30% higher than previous measurements using layered targets(1.8) . This is probably

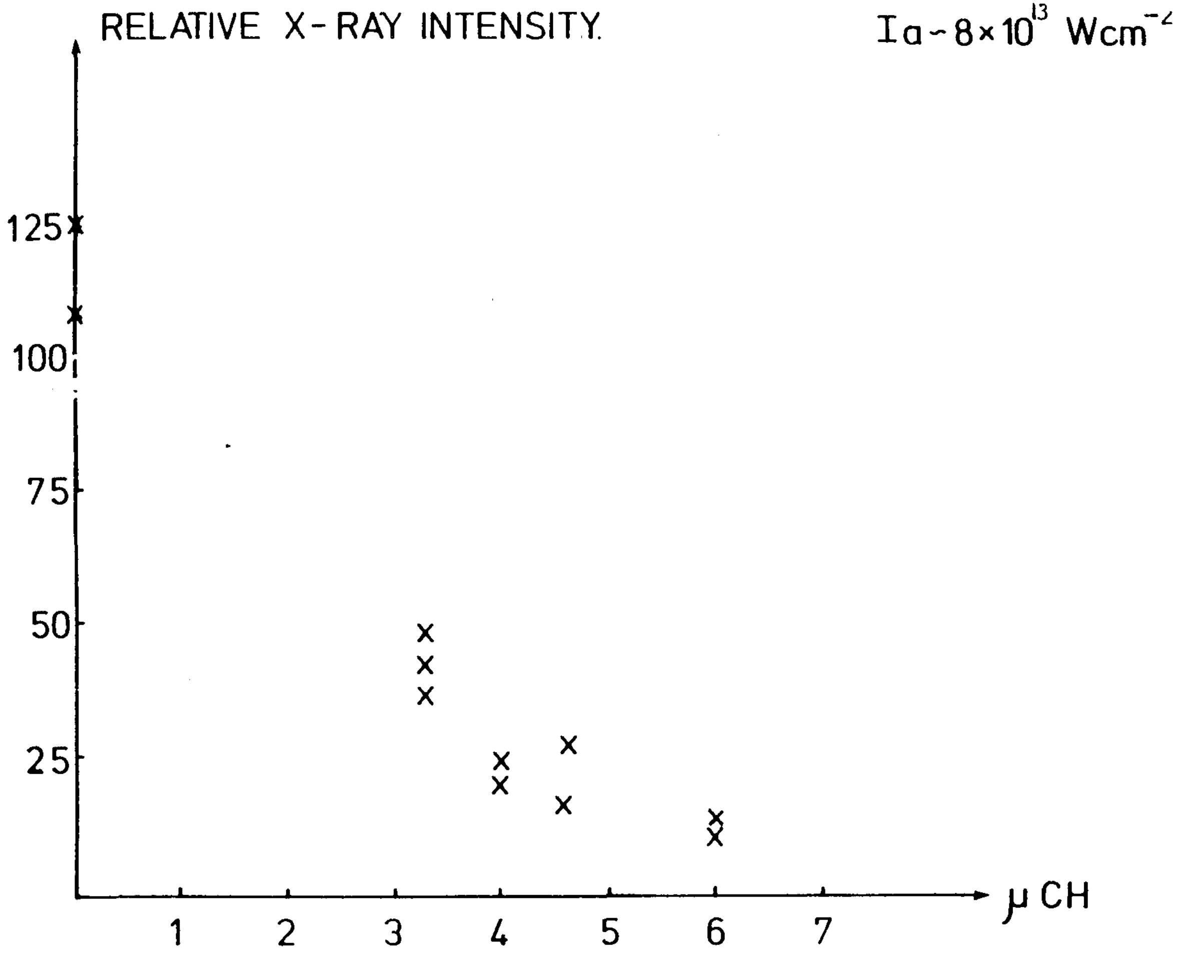

Fig(2.3) Relative x-ray yield as a function of the thickness of the plastic coating.

because the results recorded here are time integrated, whereas those in (1.8) are time resolved. Mass ablation still occurs for a short time after the end of the laser pulse, and thus the time integrated result is larger than the time resolved.

The shot parameters are tabulated below.

Shot number	E_{inc} J	%abs	D/R	X-ray Unifmty	Beam Balance
01270483	281	22	4.5	45%	6%
11280483	280	20	4.5	52%	11%
16280483	254	15	5.5	29%	15%
18280483	193	27	3.5	59%	8%
20280483	225	19	5.0	39%	24%
21280483	169	19	5.25	39%	17%
23280483	163	21	4.25	76%	36%
03290483	238	21	4.5	30%	13%
06290483	277	29	3.5	50%	16%
09290483	246	19	4.5	20%	6%
14290483	258	17	5.0	37%	7%
04070783	183	17	4.5	99%	49%
09070783	192	21	4.5	70%	8%
12070783	214	17	5.5	84%	10%
13070783	233	18	4.5	42%	13%

Typical results are shown in Figs(2.4). The width of the ring on the horizon (15 μm at FWHM of intensity) is in good agreement with Medusa simulations of the distance moved by the ablation surface convolved with the pinhole response. Thus the emitting ring is thin, the bright ring gives information about a thin band around the target passing through the different beam overlap positions.

2.9 Quantitative Results

Two dimensional densitometer tracings of the pinhole pictures were scanned using a Joyce Loebl densitometer linked to a GEC 4080 computer. The results are outputted as

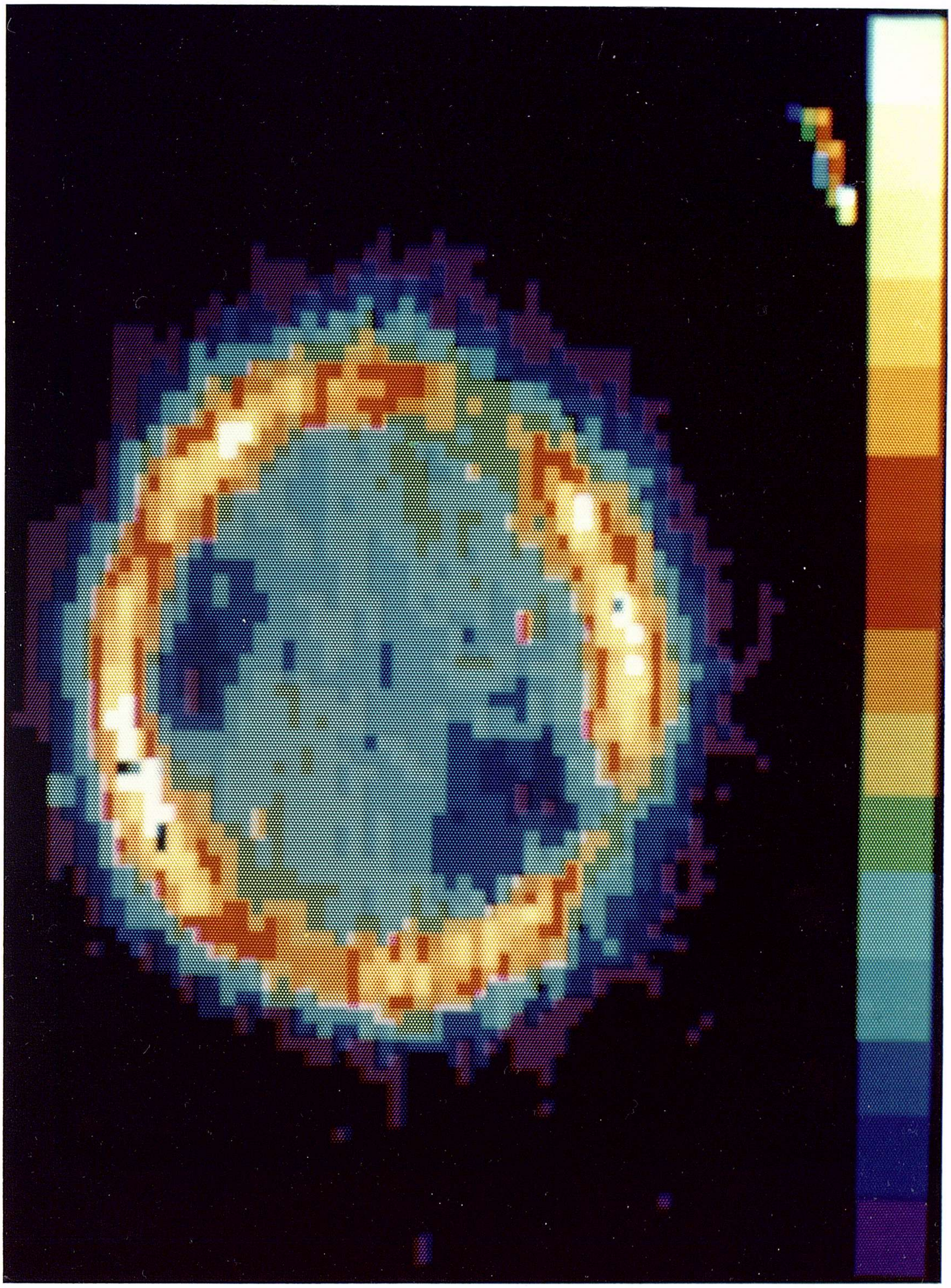

Fig(2.4a) Computer coloured picture of the x-rays from an irradiated microsphere, Shot 09290483. White corresponds to the greatest intensity, and blue the lowest. E_{inc} = 246 J, 19% absorbed, 20% uniformity, 6% beam balance.

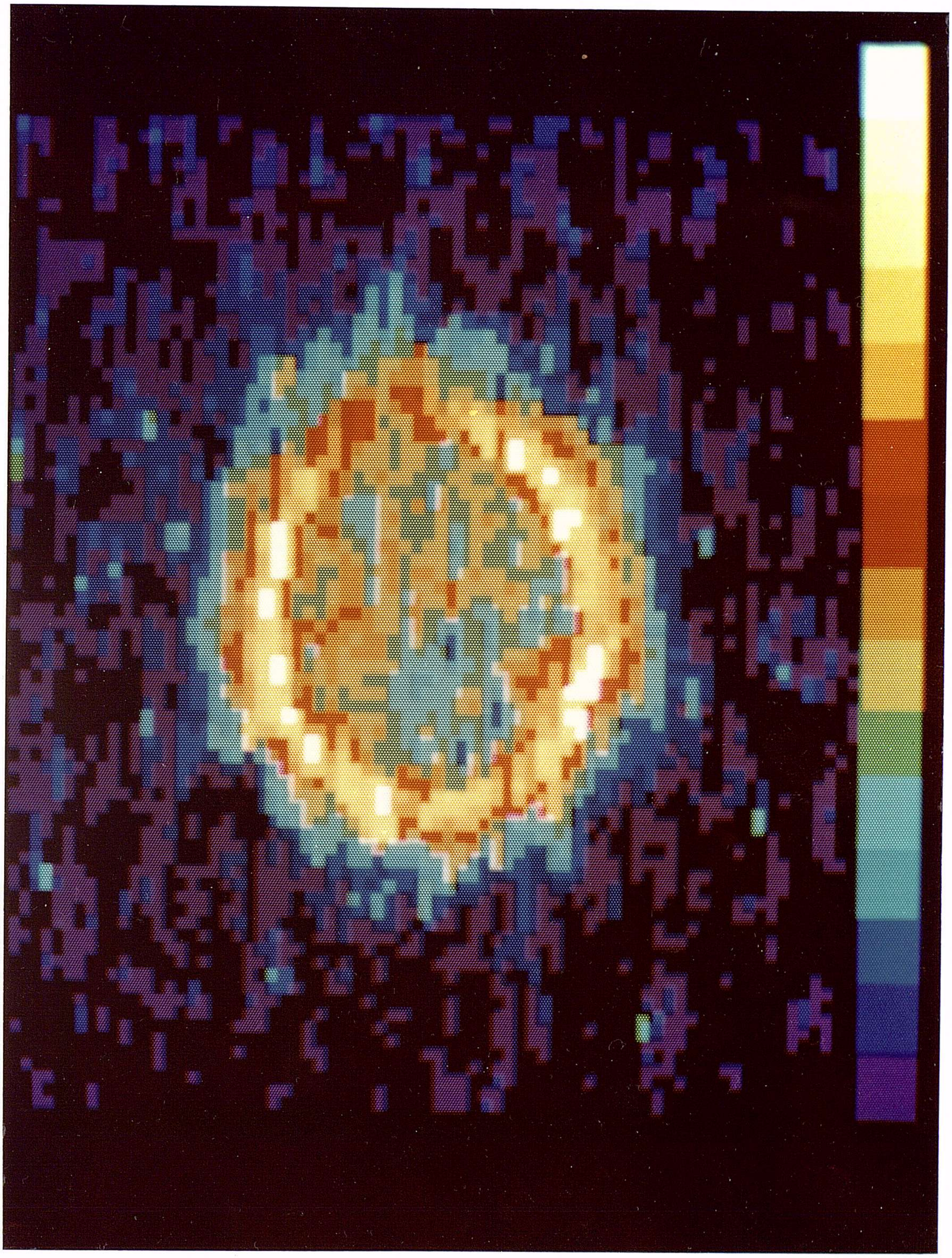

Fig(2.4b) Shot 01270483.
E_{inc} = 281 J, 22% absorbed, D/R = 4.5, beam balance of 6%, x-ray uniformity of 45%.

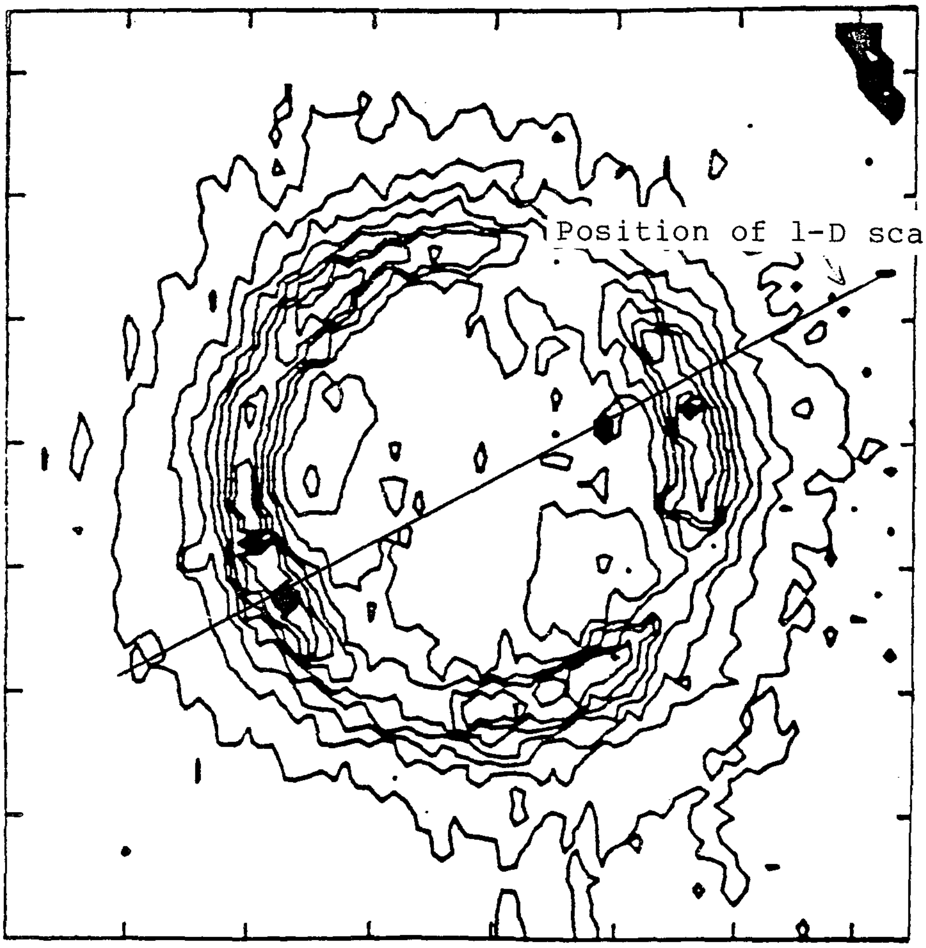

Position of 1-D scan in Fig(2.5b).

Fig(2.5a) Isodensity plot of Shot 09290483.

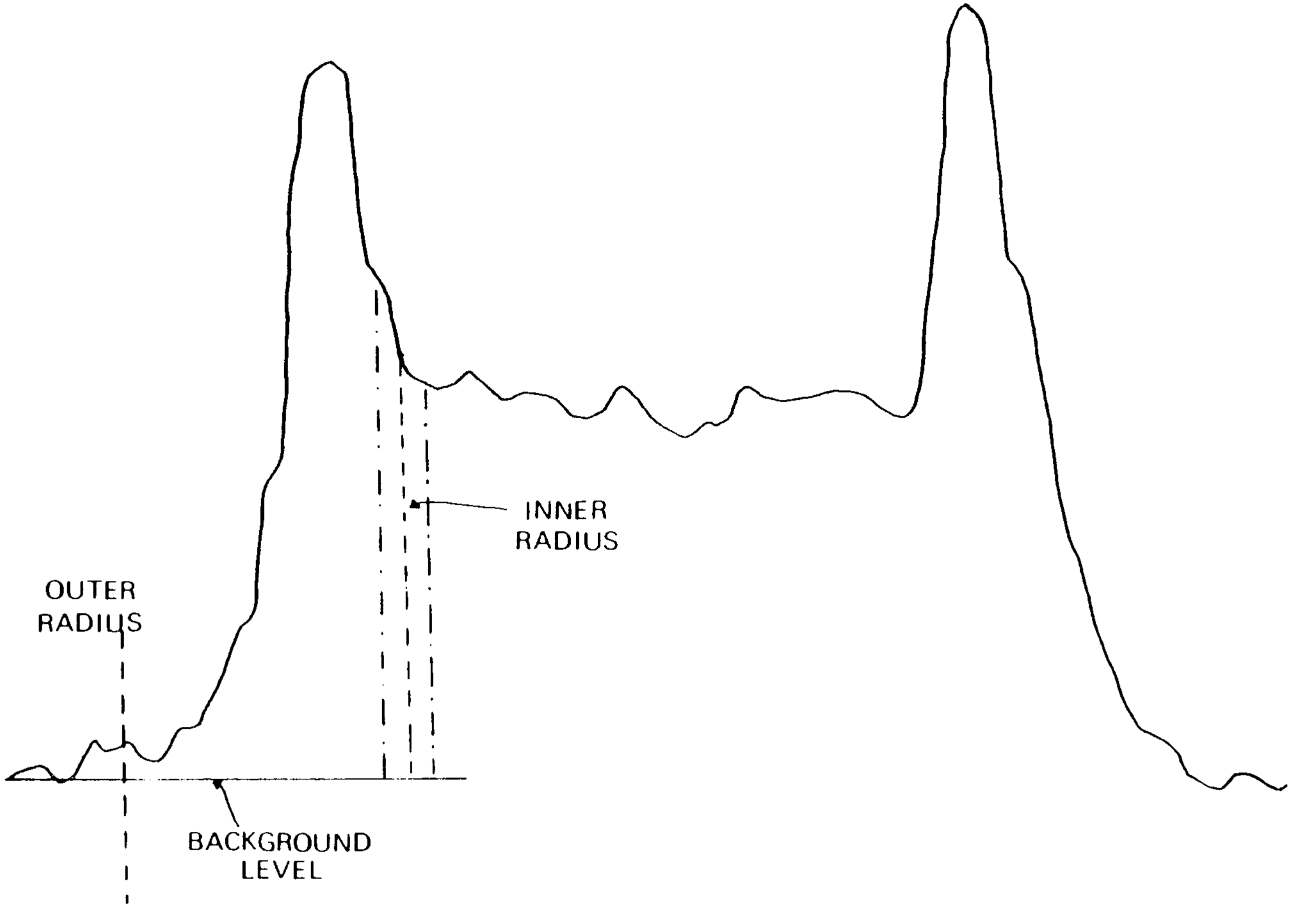

Fig(2.5b) 1-D scan in film density through Shot 09290483.

contour maps of isodensity, or as a 1-D scan through the target, as shown in Figs(2.5). The intensity of the x-rays at any position around the limb broadened ring was calculated by dividing the ring into a set number of bins, integrating from an inner to an outer radius, subtracting off the background, and allowing for the film response using the results of Dozier et al(2.4) . The outer radius is made quite large, ≈30 μm beyond the centre of the limb, beyond which the x-ray yield is negligible. The inner radius is more difficult to position, as it can not be said objectively where the x-rays from the central region of the target start to contribute. Nominally it was set at a position where the intensity was 10% higher than that in the centre of the ring. Two other positions were tried, as shown in Fig(2.5), which gave answers differing by less than ± 5%; thus the degree of subjectivity in the definition of the inner radius does not lead to large errors.

To first order we can assume that the x-ray yield from the plastic or glass is proportional to the time the laser spends burning through the respective material. The emission is optically thin; the Al filter transmits 1% above the Al K edge; below the edge, for a typical density of 5×10^{-2}gcm^{-3} (where most x-rays are produced) the light will be reduced to 1/e of its initial intensity after passing through 140μm of glass.

Therefore we can write:

$$I = A(0.6 - T) + BT \qquad (2.1)$$

where I is the relative x-ray intensity, T the time the laser spends burning through the plastic in nanoseconds, and A and B are constants determining the relative brightness of glass and plastic respectively. From Fig(2.3) we see that at T = 0 for $I_a = 10^{14}\mathrm{Wcm}^{-2}$

$$I = 117 \pm 8 = 0.6A \qquad (2.2)$$

Therefore A = 195 ± 13.

And at T = 0.6 (i.e. no burn through to the glass)

$$I = 11 \pm 1 = 0.6B \qquad (2.3)$$

Therefore B = 18.3 ± 2 Using these values it is possible to convert x-ray intensities around the ring to time spent in the plastic, and hence determine the differences in the mass ablation rate around the horizon of the microsphere. The uniformity, as defined by $(\dot{m}_{max}-\dot{m}_{min})/\dot{m}_{min}$, where $\dot{m}$ is the mass ablation rate, is plotted as a function of defocus in Fig(2.6). Also plotted is a curve passing through the best points, giving an indication of the boundary on the uniformity. Two theoretical profiles are also shown; these will be discussed in section(2.13). The uniformity at a given defocus varies dramatically. Fig(2.7) shows uniformity plotted as function of beam balance; little correlation can be seen. Thus the variations in uniformity at a given defocus must be due to pointing errors in the alignment of the beams, or hot spots and irregularities within the individual beams.

It is therefore necessary to know whether the points of best uniformity at a given defocus are limited by beam

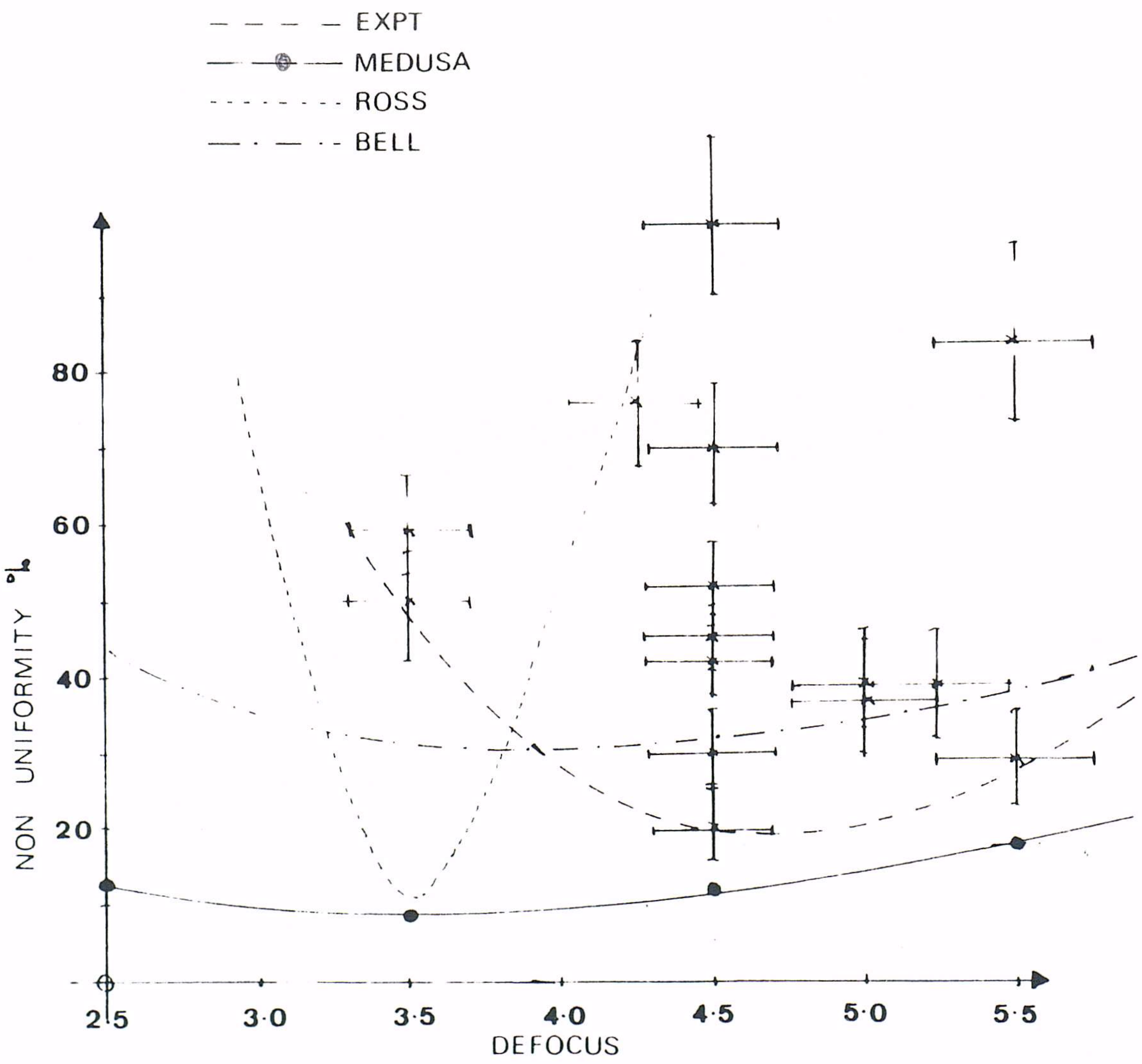

Fig(2.6) Uniformity as a function of defocus for experimental results and theoretical profiles.

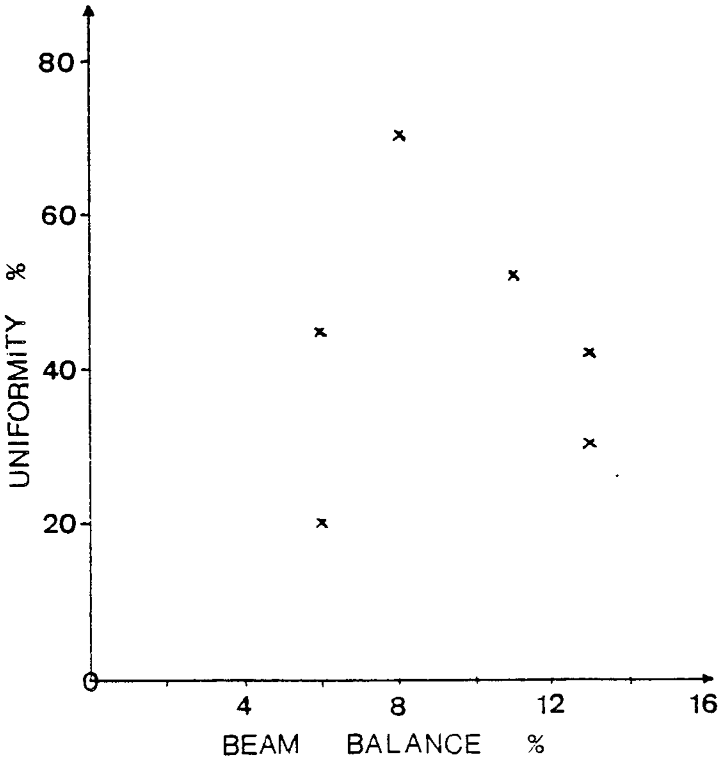

Fig(2.7) Uniformity as a function of beam balance for a defocus of 4.5.

overlap effects, or simply by beam quality. If beam overlaps are the dominant effect we would expect some symmetry in the pictures corresponding to the overlap positions.

Fig(2.8) shows the measured variation in mass ablation rate around the horizon of the target for the most uniform pictures at three different defoci. Also shown are the relative fourier components.

For D/R = 3.5 we see peaks at the double beam overlap positions; for D/R = 4.5 and 5.5 we see clear peaks at the triple beam overlap positions. This supports the view that these values of uniformity are limited by overlap effects. The four peaks at triple overlaps are predicted by theoretical models, as are the peaks at the double positions at lower defoci.

Also shown in Fig(2.8) are results from a shot showing large (50 %) uniformities at D/R = 4.5. No symmetrical features are seen, implying that the non uniformity is due to bad beam quality.

Fig(2.4) shows a computer coloured picture of shot 09290483 ; the four peaks in the ring correspond to the four triple overlap positions around the horizon of the microsphere, and the minima being the single and double positions. Also, within the ring, towards the centre of the target, two minima (coloured blue) can be seen and,less clearly, another two maxima from triple beam overlaps.

We see that the optimum defocus is at a D/R of 4.5 and

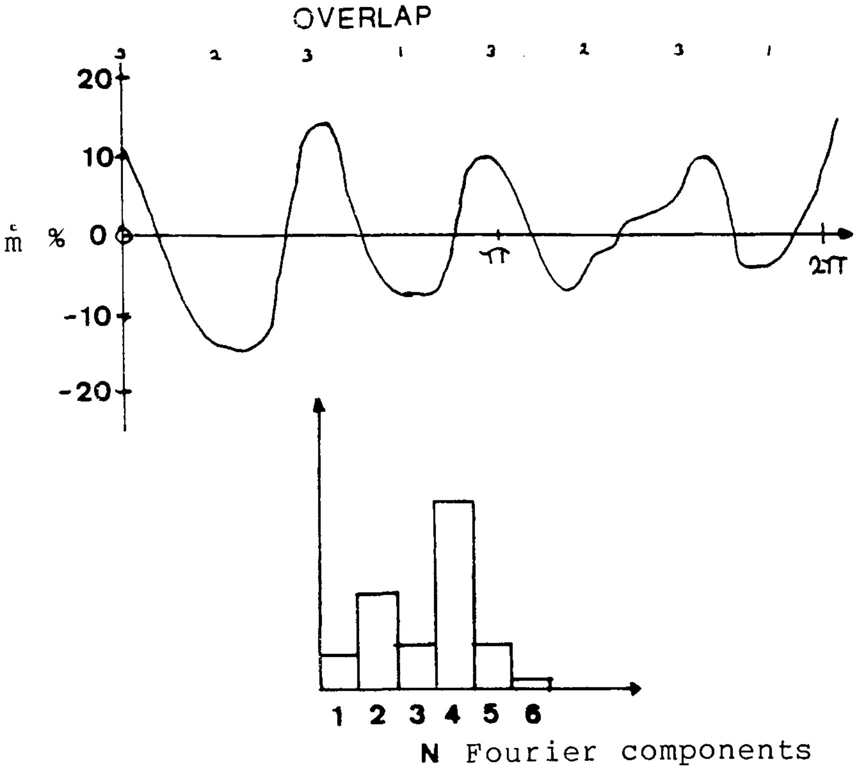

Shot 09290483, D/R = 4.5
E_{inc}= 246 J, 19% absorbed, 20% uniformity, 6% beam balance.

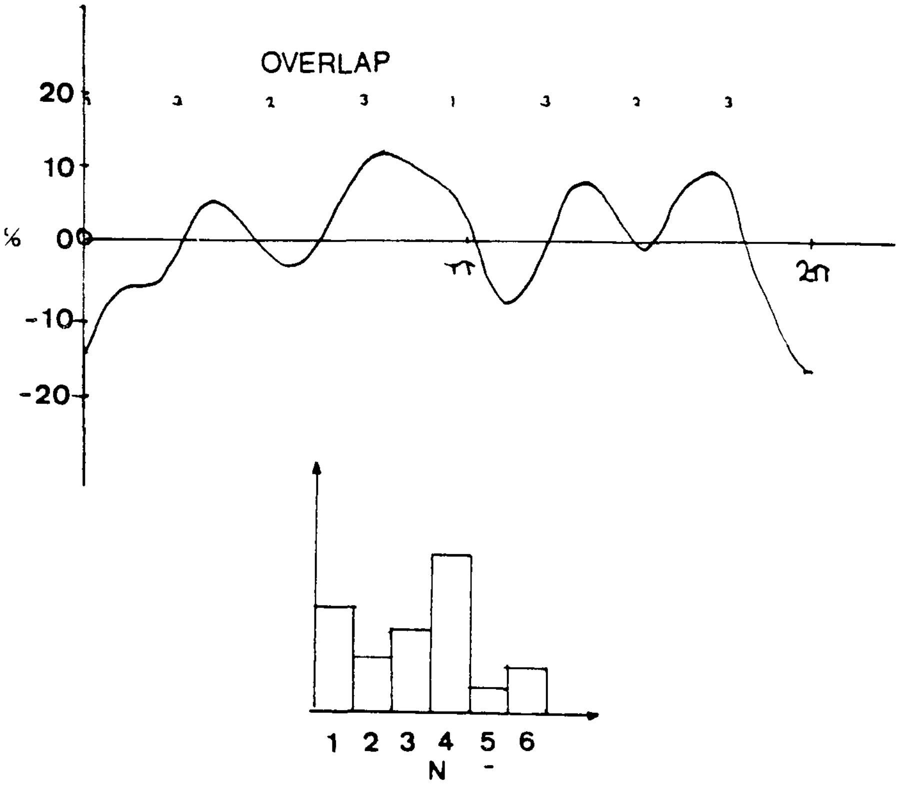

Shot 16280483, D/R = 5.5
E_{inc}= 254 J, 15% absorbed, 29% uniformity, 15% beam balance.

Fig(2.8) Variation in mass ablation rate around the microspheres.

(The Fourier components, a_n, are defined by $a_n = \int \cos(n\pi x/L)\dot{m}$ where x is the distance around the sphere and L the circumference.)

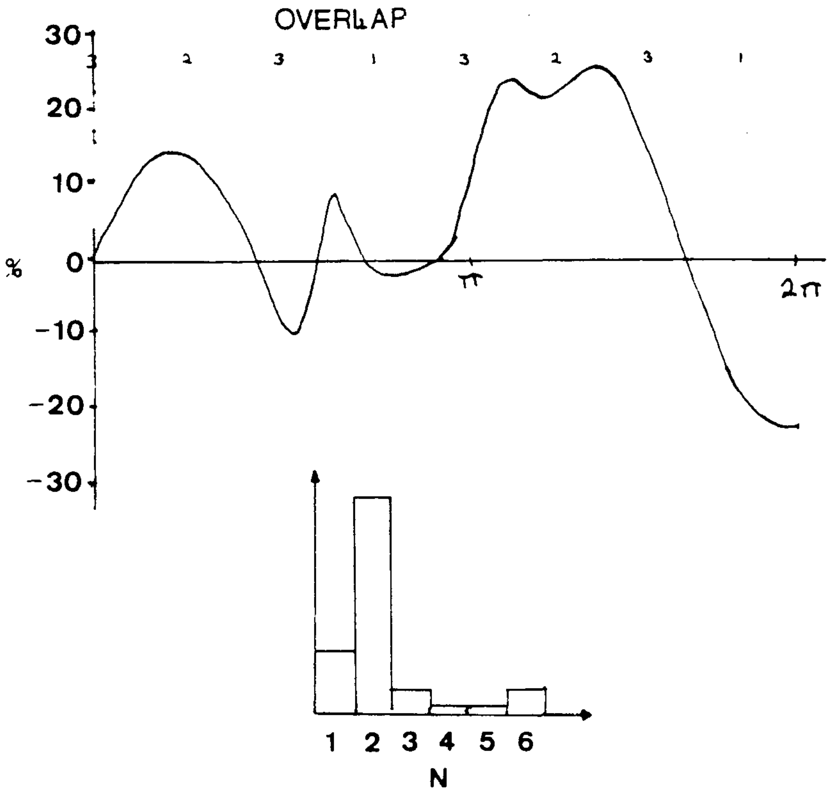

Shot 06290483, D/R = 3.5
E_{inc}= 277 J, 29% absorbed, 50% uniformity, 16% beam balance.

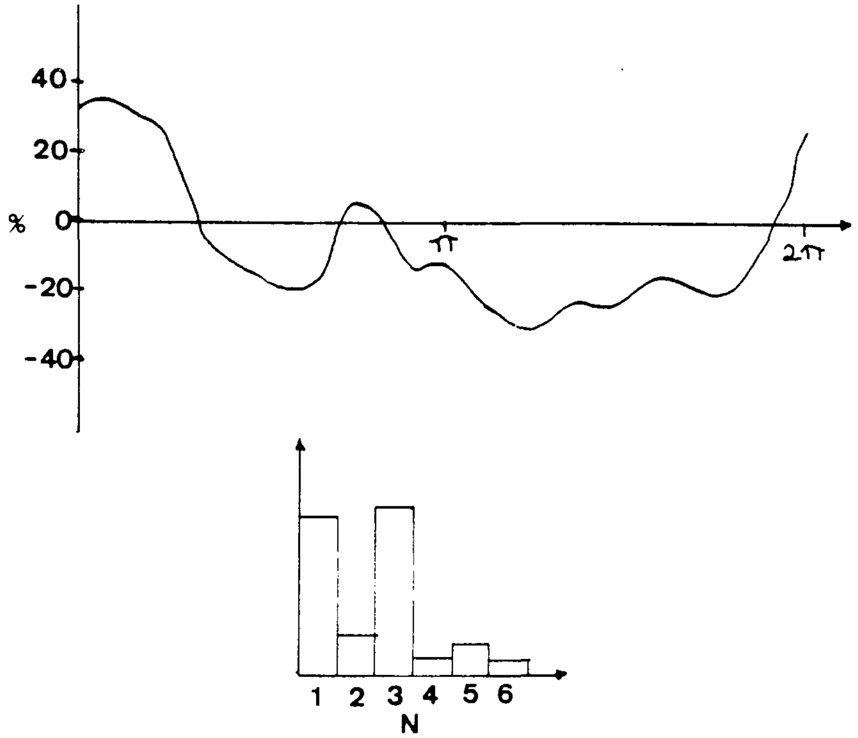

Shot 11280483, D/R = 4.5 (52% non uniformity)
E_{inc}= 280 J, 20% absorbed, 52% uniformity, 11% beam balance.

taking the average of the three best results, the mass ablation rate is 25 ± 5% higher at the triple beam overlap positions than at single beam positions, with the two beam overlaps half way inbetween. Also, the features within the ring on shot 09290483 as described above yield the result of 29% confirming the validity of the approach.

2.10 X-ray Shadowgraphy of Implosions

Subsequent to the experiment described above a group from Queens University Belfast used the technique of short pulse x-ray backlighting to observe ablatively imploded microballoons under similar conditions of irradiance and defocus as described above; it is useful to make a comparison with their results(2.5).

A shadowgraph of an imploding microballoon is shown in Fig(2.9). The hexagonal structure due to the higher ablation pressure at the beam overlaps can clearly be seen. However, these results were obtained with a camera looking down a triple beam overlap position, and so the sides of the hexagon correspond to double beam positions. The flat faces due to three beams are at an angle of 76^0 to the line of sight, and are not seen.

The percentage non-uniformity from the shadowgrams can be estimated as 20 %, in reasonable agreement with the x-ray data.

2.11 Absorption Results

The absorbed fraction is plotted as a function of defocus in Fig(2.10). The absorbed energy falls off with

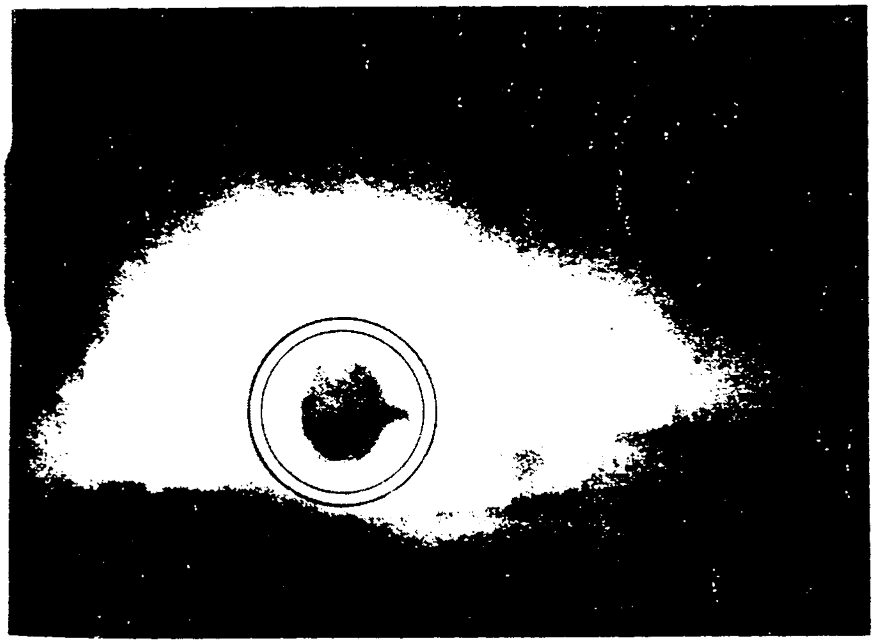

SHOT 19 ON 19/05/83

Fig(2.9) Shadowgraph of imploding microballoon at a defocus of 4.5 from ref(2.5).

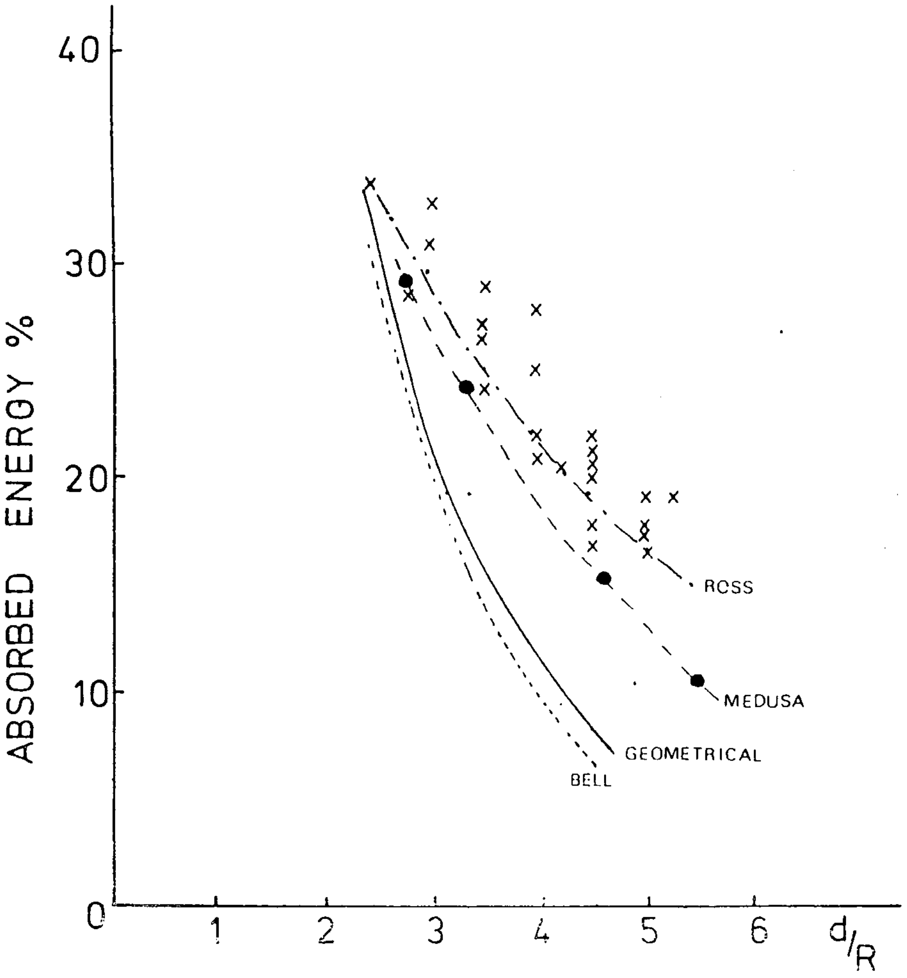

Fig(2.10) Absorbed energy as a function of defocus.

increasing defocus due to the beams starting to miss the target. However, the fall-off is not as great as purely geometrical considerations would suggest: this is due to absorption out in the corona, and will be dealt with in section (2.15).

No correlation could be found between the calorimeter positions and absorbed fraction (i.e. the absorption did not seem enhanced at the overlaps). This is thought to be due to a combination of the random error in calorimeter readings and the fact that after peak implosion the debris reaching the calorimeters will not necessarily be travelling in directions corresponding to overlaps.

2.12 Theoretical Calculations

The uniformity of energy deposition is dependent on the number of beams, their focusing conditions, and the form of the electron density distribution. Ross(2.1) has developed an absorption model assuming inverse bremsstrahlung and looked for optimum beam characteristics (such as the power of the super gaussian of the radial profile of the beam intensity) to maximise uniformity in a six beam system with f/1 lenses - i.e. that relevant to the results described here. The experimental results are compared with calculations obtained using his model for an inverse square electron density distribution. Comparisons are also made with the work of Bell(2.6), who also uses Ross's model with the simplifying assumption of short scale length electron densitydistributions.

2.13 The Absorption Model

Assuming the only absorption mechanism is inverse bremsstrahlung, the rate of energy loss of a light beam propagating through a plasma is(2.7);

$$\frac{dE}{ds} = -\beta E \qquad (2.4)$$

$$\text{where } \beta = \frac{n_e^{\,2}}{n_c T_e^{3/2} \mu} \qquad (2.5)$$

$$\text{Now } \mu^2 = 1 - n_e/n_c \qquad (2.6)$$

and assuming T_e is approximately constant outside of the critical surface, from (2.4)(2.5) and (2.6) we obtain:

$$\frac{dE}{E} = \frac{-k(1 - \mu^2)ds}{\mu} \qquad (2.7)$$

where k is a constant ~ $n_c/T_e^{\,3/2}$

The formula of Bouguer(2.8) in spherical geometry is

$$\mu r \mathrm{Sin}\phi = \text{constant} = \mu_0 r_0 = r_1 \qquad (2.8)$$

and equation (2.7) reduces to

$$\frac{dE}{E} = \frac{-k(1 - \mu^2)\,^2 r dr}{(\mu^2 r^2 - r_1^{\,2})} \qquad (2.9)$$

If the electron density distribution is defined as a function of r then μ(r) is known and the equation for energy deposition can be integrated. In practice the distribution will be non analytic; a typical distribution from Medusa is shown in Fig(2.11), along with an inverse square distribution. The code distribution is in between a true inverse square and a short scale length inverse square. Thus the experimental results were compared with a true inverse square distribution, short scale length

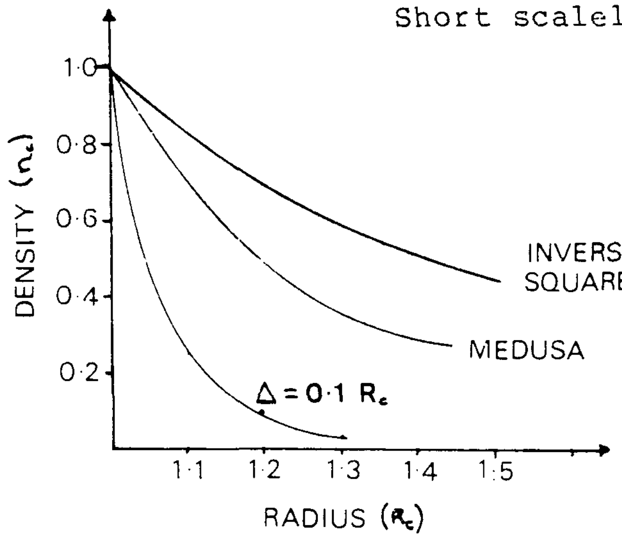

Short scalelength inverse square

$$\frac{n_e}{n_c} = \frac{\Delta^2}{(r-r_c+\Delta)^2}$$

Fig(2.11) The different electron density distributions.

distributions (Bell's model) and Medusa calculations using ray tracing as described in section (2.16).

2.14 The Inverse Square Distribution

The inverse square electron distribution is

$$\frac{n_e}{n_c} = \frac{r_c^2}{r^2} \qquad (2.10)$$

$$\text{Thus } \mu^2 = 1 - r_c^2/r^2 \qquad (2.11)$$

Substituting (2.11) into (2.9) we obtain;

$$\ln\left(\frac{E}{E_0}\right) = -kr_c^4\int\frac{dr}{r^3(r^2 - a^2)^{1/2}} \qquad (2.12)$$

$$\text{where } a = (r_c^2 + r_1^2) \qquad (2.13)$$

The limits on the integral on the right hand side of this equation run from ∞ to r for a position before the light is reflected near critical density, and from ∞ to a and back out to r for reflected light; i.e. the integral has a singularity at r=a and must be evaluated in the complex plane.

After some algebra Ross finds the result that a beam of energy E_0 incident at an angle ϕ_0, at an angle η to the line running from the centre of the target to the point of reflection has an energy E, at a position defined by the angle θ^1, of

$$\ln\left(\frac{E}{E_0}\right) = -\frac{kr_c}{2}\mathrm{Cos}^3\phi_0\left(\frac{\pi}{2} + \theta^1 + \frac{1}{2}\mathrm{Sin}2\theta^1\right) \qquad (2.14)$$

Therefore the total absorbed energy, which we shall use to compare with the calorimetry results, is given by the case of $r \to \infty$, i.e. $\mathrm{Cos}\theta^1 = 0$, $\theta^1 = \pi/2$:

$$E_{abs} = 1 - \exp-\left(\frac{kr_c}{2}\pi\mathrm{Cos}^3\phi_0\right) \qquad (2.15)$$

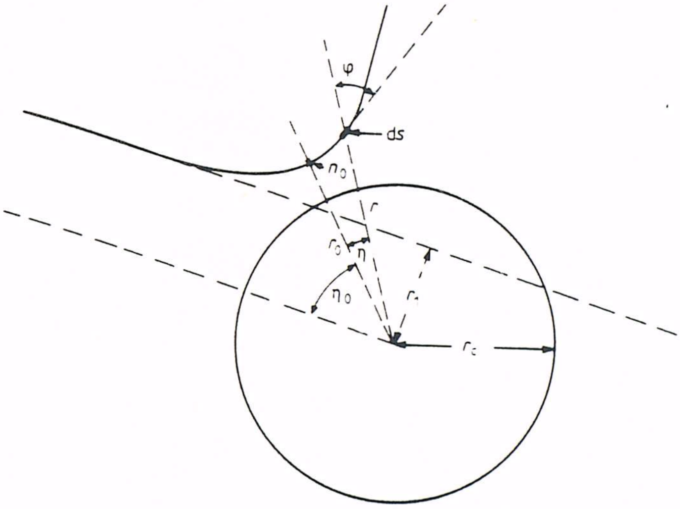

Fig(2.12) Geometry used in Ross's calculations from ref (2.1).

Referring to Fig(2.12) consider a cone of rays at θ, containing an element of energy, dE :

$$dE = 2\pi I(\theta)\mathrm{Sin}\theta d\theta \qquad (2.16)$$

Where $I(\theta)$ is the beam profile as a function of θ. Then Ross finds the element of energy per steradian absorbed at ψ, dU, can be written:

$$dU(\psi) = \frac{1}{\sin\psi} \int \frac{I(\theta)E \cos^2\phi_0 \cos^2\theta^1 \sin\theta d\theta}{\tan\phi_0} \qquad (2.17)$$

between the limits of θ_m and θ_f,

where $\tan\phi_0 = p\sin\theta$

$\theta^1 = \eta/\sin\phi_0$

$\eta = \psi-\theta-(\pi\sin\phi_0/2)$

θ_f = angle corresponding lens edge

$\theta_m = \psi - 2\eta_0$

This equation can be integrated numerically to find the variation in the total energy deposited per steradian as a function of ψ.

The uniformity can be calculated for all points on the target by the addition of all the contributions from each beam. In six beam geometry the extremes of irradiance occur at one or other of only four characteristic points on the target surface; these four points are:

i) at the beam centre where the total energy deposition from all beams is

$U_1 = U(0) + 4U(90)$

ii) midway between two beams

$U_2 = 2U(45) + 2U(90) + 2U(135)$

iii) equidistant from any three beams

$U_3 = 3U(54.74) + 3U(125.26)$

iv) a point tangential to rays from two neighbouring beams.

The numbers in brackets refer to the appropriate angle in degrees.

We can define the percentage non uniformity as $(U_{max}-U_{min})\times100/U_{min}$. This is plotted for the inverse square distribution as a function of defocus in Fig(2.6). The beam parameters have been chosen to best fit the experimental profiles$^{(2.9)}$ - i.e. a super gaussian power four with a fill factor of 0.7.

However, the energy uniformity and mass ablation rate uniformity are not equivalent. Energy deposited further out in the corona will be less effective in applying ablation pressure than energy deposited nearer the critical surface. Evans$^{(2.10)}$ used Medusa to derive the relationship

$$P \; \alpha \; U\rho^{1/2}$$

His approach was to deposit known quantities of energy at different distances from the critical surface and note the change in the ablation pressure.

The uniformity was recalculated using this model, but the results were only ≃ 4% different than before at any given defocus. This is because the $(r_c/r)^2$ model deposits a similar large amount of energy per beam for different ψs at distances far out into the corona as shown in Fig(2.13).

A similar calculation to that outlined above for the inverse square model can be carried out for a short scale length inverse square electron density distribution. Ross finds that in the limit of the scalelength tending to zero a particular cone of rays is absorbed at one particular point on the critical surface of the target; and the total energy absorbed is

$$E_{abs} = 1 - \exp(-k \cos^2\phi_0) \qquad (2.20)$$

Bell makes the further approximation that the absorbed fraction is small, and expands the exponential to give

$$E_{abs} = k \cos^2\phi \qquad (2.21)$$

The results of this model are plotted along with the true inverse square in Fig(2.6). The rise after the minima is much steeper in the $(r_c/r)^2$ case because there is a further contribution from energy absorbed far out in the corona not present in the short scalelength model (in which there is no contribution from rays missing the critical

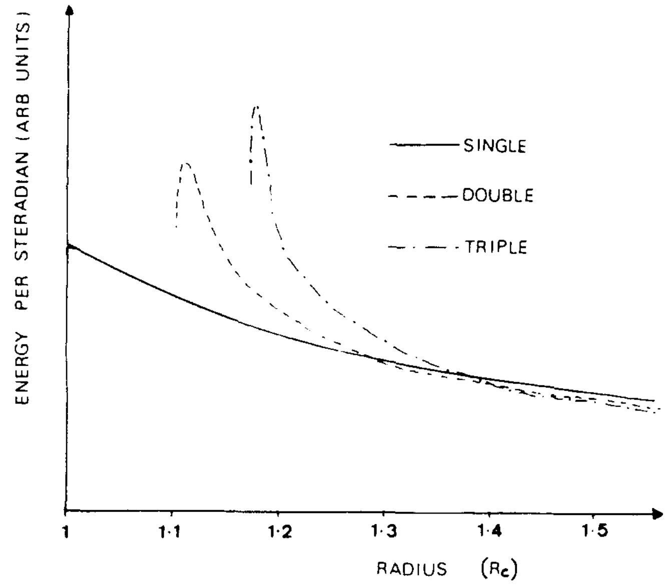

Fig(2.13) Energy deposited as a function of radius for different overlaps using Ross's model.

surface).

2.15 Absorbed Fraction

The experimental results for the fractional absorbed energy are plotted as a function of defocus in Fig(2.10). Assuming a particular value for the absorbed fraction at normal incidence it is possible to evaluate the absorbed fraction as a function of defocus for the different electron density models, e.g. equation (2.15). The results are also shown in Fig(2.10).

It can be seen that the $(r_c/r)^2$ model fits best, showing that a significant amount of energy is still absorbed out in the corona. The short scalelength model, which ignores all the energy missing the critical surface, gives too low a value of absorption at high values of defocus, as does the geometrical model which assumes that the absorption scales as $(R/D)^2$.

The experimental values of D/R refer to the initial target surface, whereas the theoretical calculations are evaluated with respect to the critical surface. Medusa calculations show that the critical surface expands to about 10% further out than the initial radius, and this value has been used to scale the theoretical results onto the experimental in Figs(2.10)and(2.6).

2.16 Computer Simulation of Uniformity

A comprehensive simulation of the effects of refraction and the interaction of non uniform energy deposition with the hydrodynamics requires a 2-D code incorparating raytracing: unfortunately such a facility was not available to the author. However, the 1-D Lagrangian code Medusa has long been used at RAL to simulate laser implosions. Medusa has been modified by MacGowan(2.11) to incorparate raytracing, yielding pseudo 2-D information.

2.17 The Raytracing Subroutine

This subroutine takes the electron distribution beyond the critical surface computed using the normal 1-D code then, assuming spherical symmetry, sets up a 2-d grid below critical density and traces the paths of the rays through the corona, depositing energy via inverse bremsstrahlung. On reflection a predetermined fraction of the remaining energy can be deposited in the two cells either side of critical to simulate resonance absorption.

The input data to the subroutine includes the f number of the lenses, the distance they are focused beyond the target, the resonance absorption fraction, beam profile (i.e. power of the super gaussian), lens fill factor and the frequency of call from the main routine. The effect of all six beams is added in.

The output from the routine is energy deposition as a function of radius and angle subtended from the centre of the sphere, i.e. ψ. In a particular code run one value of ψ is chosen, and the energy deposition as a function of radius is fed back into the main routine for this value of ψ. Thus comparing different runs at different ψs we gain pseudo 2-D information.

2.18 Results from Medusa

The mass ablation uniformity is calculated by comparing the total mass ablated at 725ps after the onset of the pulse at single, double and triple beam overlap positions for a given defocus. The results are plotted in Fig(2.6). We see that Medusa predicts that the best uniformity occurs at a defocus of 3.5, and is~10 %.

The absorbed fraction predicted by Medusa is plotted along with the experimental results in Fig(2.10); it can be seen that there is good agreement.

2.19 Discussion

The experimental results agree qualitatively with the two analytic models and the results from Medusa; they show that better uniformity of illumination can be obtained by overfilling the target. Quantitatively, however, they do not agree. First the optimum uniformity is found to be at a defocus of 4.5, as opposed to the 3.5 predicted; secondly the best uniformity is found to be 20%, whereas 8 % is predicted by analytic models and 10% from Medusa calculations. However, since all the models used assume a spherically symmetric electron density distribution (which will clearly not be the case) these discrepancies are not surprising, and the experiment shows that better modeling is needed.

The main object of the experiment, i.e. finding the optimum defocus for subsequent implosion experiments, has been fulfilled, and the uniformity is found to be optimum at

D/R=4.5, the non uniformity being due to more energy deposited at the three beam overlap positions.

2.20 Conclusion

The uniformity of the x-rays from the ablation surface of laser irradiated spheres has been measured. The best uniformity has been found to be 25±5% at a defocus of 4.5. Large variations in uniformity at given defoci independent of gross beam balance indicate that hot spots in the beams or pointing errors may be to blame.

This improved uniformity is made at the expense of the absorbed fraction; 20% is found to be absorbed at a defocus of 4.5, as opposed to 33% at obscuration.

CHAPTER THREE

X-RAY BACKLIGHTING OF R-T UNSTABLE FOILS

Abstract

X-ray short pulse radiography of laser accelerated foils has shown evidence of variations in the ρr, however, the integrity of the initial corrugations is not maintained, and it is shown that this is probably due to ring structure in the three beams driving the foil.

3.1 Introdution

It was shown by Rayleigh(3.1), and later by Taylor(3.2) that if the density and pressure gradients in a fluid, or superposition of fluids, are opposed, then the system is hydrodynamically unstable.

The simplest case is that of two inviscid fluids of differing densities, ρ_1 and ρ_2 $(\rho_1 > \rho_2)$, which are superposed, the heavier on the lighter, in a gravitational field as shown in Fig(3.1). Rayleigh showed that if the interface between the two fluids is perturbed then the perturbation will grow.

The equations of motion governing the fluid are:

$$\rho \frac{\delta u_x}{\delta t} = -\frac{\delta}{\delta x} \Delta\rho \tag{3.1}$$

and

$$\rho \frac{\delta u_z}{\delta t} = -\frac{\delta}{\delta z} \Delta\rho - g\Delta\rho \tag{3.2}$$

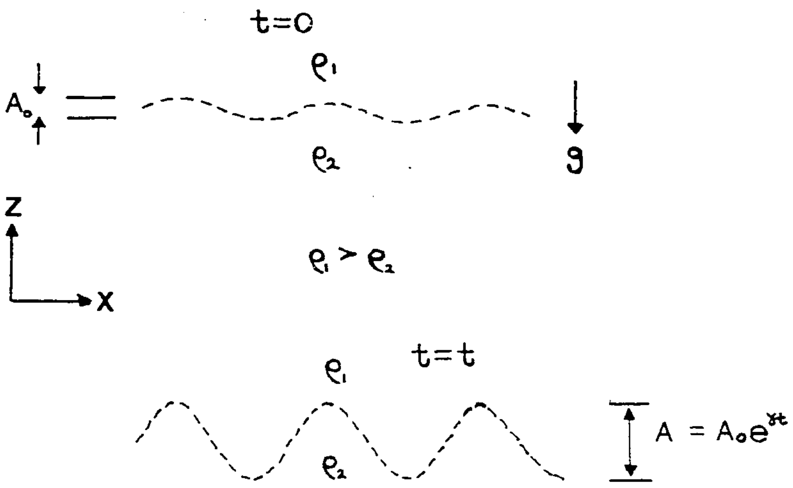

Fig (3.1) The classical Rayleigh Taylor instability.

where u_x is the velocity in the x direction, u_z the velocity in the z direction, and $\Delta\rho$ the increase in density at any point.

Also if we assume that the fluids are incompressible then:

$$\frac{\delta u_x}{\delta x} + \frac{\delta u_z}{\delta z} = 0 \qquad (3.3)$$

And the continuity equation is:

$$\frac{\delta}{\delta t}\Delta\rho = -u_z\frac{\delta\rho}{\delta z} \qquad (3.4)$$

Analysing the disturbance into normal modes we seek solutions of the form:

$$\exp(ikx + \gamma t) \qquad (3.5)$$

For solutions of this type equations (3.1)-(3.4) become

$$ik\Delta\rho = -\gamma\rho u_x \qquad (3.6)$$

$$\frac{\delta}{\delta z}\Delta\rho = -\gamma\rho u_z - g\Delta\rho \qquad (3.7)$$

$$iku_x = -\frac{\delta u_z}{\delta z} \qquad (3.8)$$

$$\gamma\Delta\rho = -u_z\frac{\delta\rho}{\delta z} \qquad (3.9)$$

From (3.6) and (3.8) we obtain:

$$k^2\Delta\rho = -\gamma\rho\frac{\delta u_z}{\delta z} \qquad (3.10)$$

and from (3.7) and (3.9) :

$$\frac{\delta}{\delta z}\Delta\rho = -\gamma\rho u_z + \frac{g}{\gamma}u_z\frac{\delta\rho}{\delta z} \qquad (3.11)$$

Now eliminating $\Delta\rho$ from between equations (3.10) and (3.11) we obtain:

$$\frac{\delta}{\delta z}\left(\rho\frac{\delta u_z}{\delta z}\right) = k^2\rho u_z - \frac{k^2 g}{\gamma^2}u_z\frac{\delta\rho}{\delta z} \qquad (3.12)$$

This is the required equation; from this, knowing the density profile, the growth rate of the instability can be calculated. Consider two fluids superposed, as shown in Fig(3.1). In both fluids the density is uniform and within each fluid equation (3.12) reduces to:

$$\left(\frac{\delta^2}{\delta^2 z} - k^2\right)u_z = 0 \qquad (3.13)$$

of which the general solution is:

$$u_z = Ae^{kz} + Be^{-kz} \qquad (3.14)$$

Since u_z must vanish at both $z=\pm\infty$ we must assume

$$u_z = Ae^{+kz} \; (z<0) \qquad (3.15)$$

$$u_z = Ae^{-kz} \; (z>0)$$

We now come to the problem of the density discontinuity at the interface of the two fluids. If we integrate equation (3.11) over an infinitesimal element of z including z_0, the value of z at the interface, we obtain:

$$\Delta_0(\Delta\rho) = \frac{g}{\gamma}u_{z0}\Delta_0(\rho) \qquad (3.16)$$

where $\Delta_0(f) = f(z_0+0) - f(z_0-0)$ (3.17)

is the jump which a quantity f experiences at the interface $z = z_0$. Now from equation (3.10)

$$k^2\Delta_0(\Delta\rho) = -\Delta_0(\gamma\rho\frac{\delta u_z}{\delta z}) \qquad (3.18)$$

Combining (3.16) and (3.18) we obtain:

$$\Delta_0(\rho\frac{\delta u_z}{\delta z}) = -\frac{k^2 g}{\gamma^2}u_{z0}\Delta_0(\rho) \qquad (3.19)$$

This equation may be considered as a boundary condition which must be satisfied at the interface between the two fluids; in this case it can be written:

$$\Delta_0(\rho\frac{\delta u_z}{\delta z}) = -\frac{k^2 g}{\gamma^2}(\rho_1-\rho_2)u_{z0} \qquad (3.20)$$

Applying this condition to the solutions of u_z we obtain:

$$-k(\rho_1+\rho_2) = -\frac{k^2 g}{\gamma^2}(\rho_1-\rho_2) \qquad (3.21)$$

i.e.

$$\gamma^2 = \frac{kg(\rho_1-\rho_2)}{(\rho_1+\rho_2)} \qquad (3.22)$$

thus at time t the amplitude, A, will be:

$$A = A_0 e^{\gamma t} \qquad (3.23)$$

A_0 is the initial perturbation amplitude, γ the growth rate, k the wavenumber of the perturbation and a the acceleration.

Chandrasekhar(3.3) examines the effect of viscosity and surface tension on the growth rate of the system described above.

3.2 Relevance to ICF

Typical pressure and density profiles for a laser accelerated target are shown in Fig(3.2). In ablative

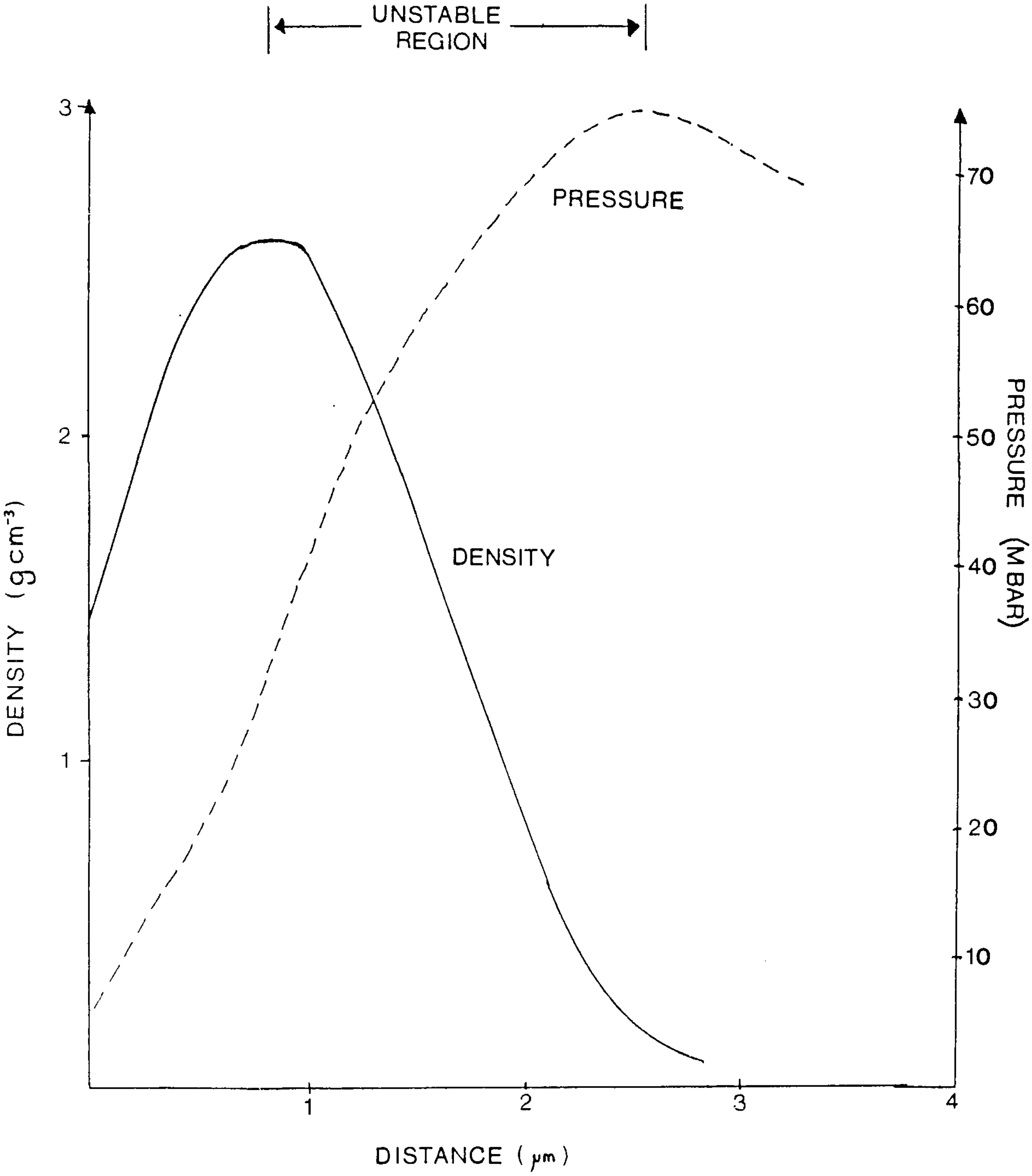

Fig(3.2) Typical density and pressure profiles for a laser irradiated target.

compressions the heavy low-pressure shell is accelerated by the high-pressure low density ablating plasma and there is a region at the ablation surface where the pressure and density gradients are opposed and the target is R-T unstable. Any density perturbations arising in the target due to non uniform ablation pressure or target imperfections will thus grow and, depending on the growth rate of the instability, may severely disrupt the spherical symmetry enough to significantly degrade the compression, or even cause complete break up of the target.

The target may also be unstable as peak compression is approached, when the shell is decelerated by the fuel. Thus the absolute value of the R-T growth rate may be of crucial importance in determining the core parameters in laser driven implosions.

3.3 Breakdown of Classical Theory

The classical R-T growth rate is derived using a linear theory. Thus it only holds if the fluid depth is much greater than the perturbation wavelength, λ, and if the amplitude is much less than λ. Also the Attwood number is inapplicable in I.C.F. targets as there are not two totally distinct fluids; the density falls off with a finite gradient moving away from the ablation surface. Various numerical analyses by Daly(3.4) and Crowley(3.5) have shown that the growth rate is reduced from the linear value (assuming an Attwood number of one) by approximately a factor of two. Indeed Crowley suggests a quadratic growth rate in the non linear regime, much slower than the exponential growth of the linear phase. Youngs has simulated the R-T instability with multiple wavelength initial perturbations(3.6) , he also suggests that the growth rate is quadratic in the non linear regime.

Thus the growth rate decreases as the amplitude approaches the perturbation wavelength. Thus the most damaging mode is the largest k that grows exponentially, i.e.

$$k \sim 2\pi/\Delta r \qquad (3.24)$$

where Δr is the thickness of the target.

Now the total growth exponent, γt, after time t is given by:

$$\gamma t = C\ (ka)^{1/2}t = C\ (2ks)^{1/2} \qquad (3.25)$$

where s is the distance moved by the target assuming constant acceleration (i.e. uniform drive pressure and neglecting the ablated mass) and C is a constant representing the reduction in growth rate from the classical.

Therefore at peak compression

$$\gamma t_{max} = (4\pi r/\Delta r)^{1/2}C \qquad (3.26)$$

where r is the initial radius of the target. Thus the R-T instability imposes an upper limit on the aspect ratio $(r/\Delta r)$ of the target. This limit was first described by Nuckolls et al(3.7), who also suggested a mechanism by which the instability may be inhibited. He suggested that the protruding spikes will move out radially as they grow into the higher temperature region of the corona; thus the tips of the spikes will be preferentially ablated, inhibiting or even saturating the instabilty. This process has been termed fire-polishing. Evidence of such a process has been found in simulations performed by McCrory et al(3.8).

Reduction of the growth rate due to the finite density gradient has been studied by Lindl and Mead(3.9) using the simple density step model; and has been generalised by Mikaelian(3.10) to exponential density profiles.

More recently Colombant and Manheimer have used a realistic density profile derived analytically using a planar ablative flow model(3.11)to determine the eigenvalues of the equation for perturbed velocity normal to the target surface(3.12) . The density profiles they derived are shown in Fig (3.3). The R-T instability is determined by the eigenvalues of the equation for the perturbed velocity, v_x, normal to the target surface:

$$\frac{d}{dz}\rho(z)\frac{d(v_x)}{dz} - \left[\rho(z)(kx_0)^2 + \frac{ka}{\gamma^2}(kx_0)\frac{d\rho}{dz}\right]v_x = 0 \qquad (3.27)$$

Where x_0 is the target thickness.The procedure they follow is to solve (3.27) for the eigenfunction and eigenvalue with the density profile given in Fig(3.3). They guess an initial value of ka/γ^2 and iterate until convergence is achieved. They find that for low irradiance ($I = 10^{13}W\ cm^{-2}$) the growth rate is reduced to $\sim 0.7\gamma_c$ for $kx_0<1$, and falls off rapidly to $0.5\gamma_c$ as $kx_0 \rightarrow 0$ as shown in Fig(3.4). Thus this analytic model shows that some

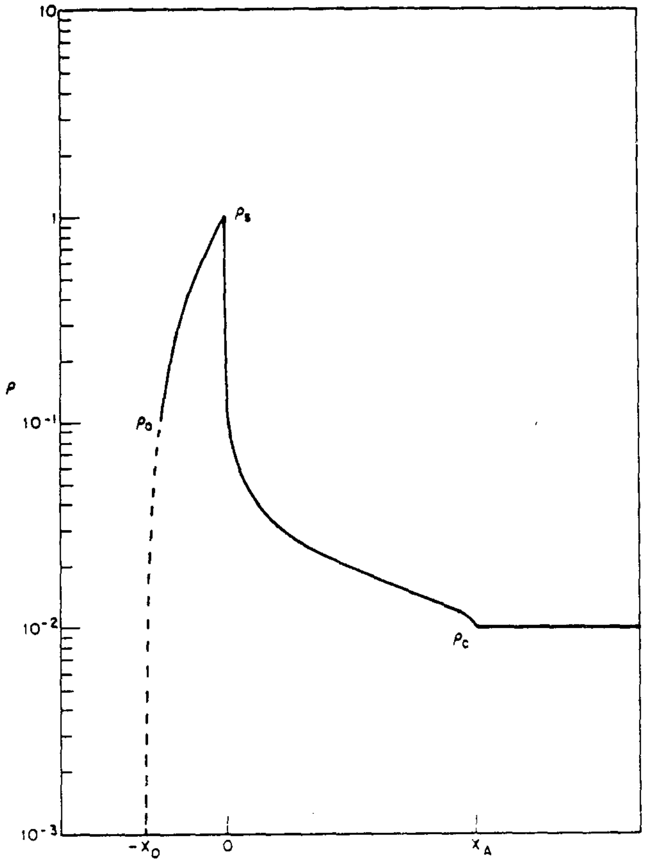

Fig(3.3) Density profile used by Colombant and Manheimer taken from ref $^{(3.11)}$.

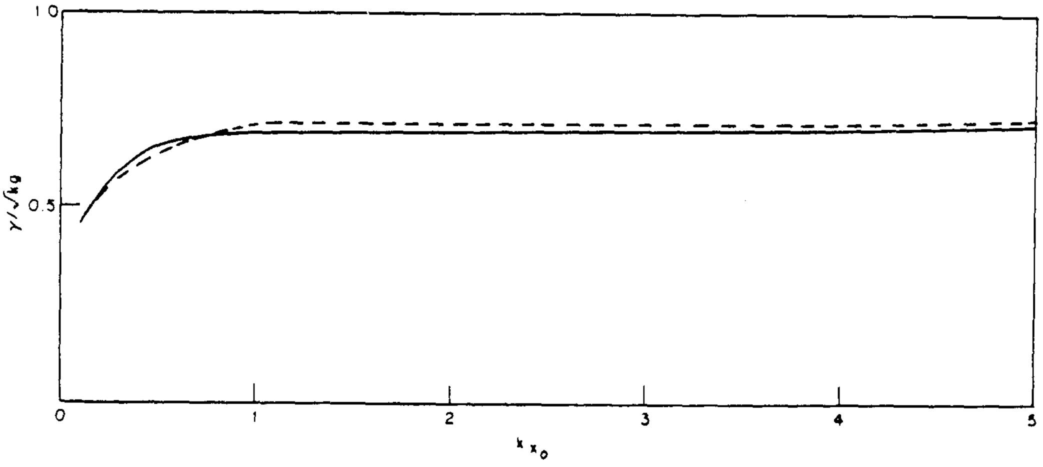

Fig(3.4) Reduction in growth rate due to density profile above from ref $^{(3.12)}$.

reduction of the growth rate can be explained purely by consideration of a realistic density profile.

Further work by the same two authors shows that vortex shedding, compressibility, thermal conduction and ablation may also be stabalising mechanisms(3.13).

3.4 The Kelvin-Helmholtz Instability

Well into the non linear regime of the R-T instability a shear layer develops at the interface of the spike of heavy fluid and the bubble of lighter fluid which can lead to the Kelvin-Helmholtz instability(3.14)(3.15). This spreads out the tip of the spike, inhibiting R-T growth. Emery, Gardener and Boris have recently observed this phenomena in 2-D simulations(3.16) , as has Youngs(3.6) .

3.5 Previous Experimental Measurements

Until 1982 the only experimental data on the R-T instability in laser accelerated targets was of an indirect nature. Colliding foil experiments were performed by Obenschain et al(3.17)who claim inhibition to R-T growth because of unmodulated shock emission from the impact foil. However, in this experiment the rear surface of the accelerated foil was being observed which, according to numerical simulation(3.8)(3.15) , is far less perturbed than the front surface.

Key et al(3.18) used time resolved x-ray shadowgraphy to diagnose six beam ablative implosions. The measured core sizes were larger than predicted by 1-D simulation and the cores lacked a clearly defined edge; this appeared to be worse for large aspect ratio targets and they cite the R-T instability as a possible explanation.

Kilkenny et al(3.19) suggested that accelerated thin foil targets may be stable to growth from noise despite classical growth exponents of 15. In this experiment the x-ray emission from silicon layers underlying thin Aluminium films was recorded. It was suggested that any R-T growth would cause a stretching of the outer Al layer resulting in a faster burn through to the silicon than for similar massive unaccelerated (i.e. R-T stable) targets. This was not observed, implying that the thin targets were stable.

The first direct evidence was observed by Cole et al (3.20). They accelerated corrugated Al foils backlit with the x-rays from a copper plasma produced from a laser beam synchronous with the drive beams. The x-rays transmitted through the foil were imaged onto a slit orientated perpendicular to the corrugations. The resultant image was then streaked to give temporal resolution. They observed the growth of a spatially periodic change in the transmission of the foil, with a wavelength corresponding to that of the initial corrugation, and a growth rate of the mass redistribution of 0.3±0.05 of the corresponding classical rate.

Even more recently Whitlock et al(3.21) have observed the R-T instability in plane targets using side on x-ray shadowgraphy . They accelerated plastic foils of 9.7μm thickness with 0.5μm bars of plastic placed periodically on the rear (unirradiated) side of the foil. After driving the foil 150μm with a 4ns pulse of 1.05μm at an irradiance of 5×10^{12}W cm^{-2}, they observed spikes protruding from the front surface of the foil with an amplitude of 65 μm, at the initial perturbation wavelength of 50 μm. In this advanced non linear regime they also observed broadening of the spikes, indicative of the Kelvin Helmholtz instability.

The most recent experimental work to be reported has been performed by Grun et al(3.22) . They buried a tracer layer of Magnesium beneath a plastic coating on the smooth laser irradiated side of a mass perturbed Carbon foil. They observed the Magnesium X-ray emission from both sides of the foil using pinhole cameras and were thus able to deduce the variation in ρr in the foil at the time of the Magnesium flash.

They observed growth in the variation of ρr in agreement with code predictions of about 0.5 the classical rate for perturbations of initial period 30, 46 and 100μm. However their technique has several disadvantages. First, the X-ray flash from the Magnesium is relatively long lived (~2ns); secondly any non uniformities in the drive beam could cause the backlight to emit at different times at different parts of the foil. The R-T instability itself could also effect the time when parts of the foil are backlit.

3.6 Experiments

Three different experiments to study the R-T instability will be described in this thesis.

i) Short pulse x-ray backlighting of plastic foils will be described in this chapter.

ii) Short pulse x-ray backlighting of plastic microballoons will be described in chapter four.

iii) A feasability study of the technique of alpha particle backlighting of foils will be described in chapter five.

Then an experiment relevant to measuring R-T growth -

iv) Short pulse point projection spectrally resolved side-on radiography of plastic foils will be described in chapter six.

These four experiments contain much that is new. The only two dimensional transmission pictures of the laser driven R-T instability to date are from Gruns work (with the disadvantages outlined above). Mass modulated microballoons have never been studied before. The technique of alpha particle backlighting is entirely novel, and very little work has been done on point projection radiography.

3.7 X-Ray Backlighting of Plastic Foils

The experiment of Cole measured the growth rate using streaked x-ray shadowgraphy. Thus only information in one spatial dimension was obtained; it could not be seen whether or not the initial parallel corrugations maintained their integrity as the instability grew, or if inhomogeneities in the drive beam had any effect.

In this experiment the driven foil was backlit with a short pulse of x-rays, through 3μm of Al filtering, and imaged with a 10 μm pinhole onto a phosphor screen and intensifier, as shown in Fig(3.5). Thus the whole of the foil could be shadowgraphed at one instance in time.

The foils used were 10 μm thick, 300μm diameter plastic. A periodic mass modulation had been applied to the foils using a novel laser etching technique developed by Rumbsy et al(3.23) at the target preparation group of the CLF. The technique involves irradiating the foils with a KrF laser through a grating with the required periodicity. The laser etches away the plastic, the depth of etching can be varied by altering the number of laser pulses. A typical mass modulated foil is shown in Fig(3.6)

The foils were accelerated with a typical absorbed irradiance of 8×10^{13} W cm^{-2} of 0.53 μm light in a lns pulse, using three orthogonal drive beams, each incident at 56^{0} to the normal of the foil. They were backlit with a short pulse (285ps FWHM) 1.05 μm beam incident onto a copper target with a focal spot size of 300 μm. This produced a plasma x-ray source about 300 μm across and 200 μm high behind the accelerated foil.

3.8 Backlighting Spectrum

The spectrum of the x-ray backlight was recorded using a miniature x-ray spectrometer with a TLAP (2d=26Å) reflecting crystal recording on No Screen film. The spectrum is shown in Fig(3.7). The broad band around 11Å is due to transitions between 3p-3s states in Neon like copper.

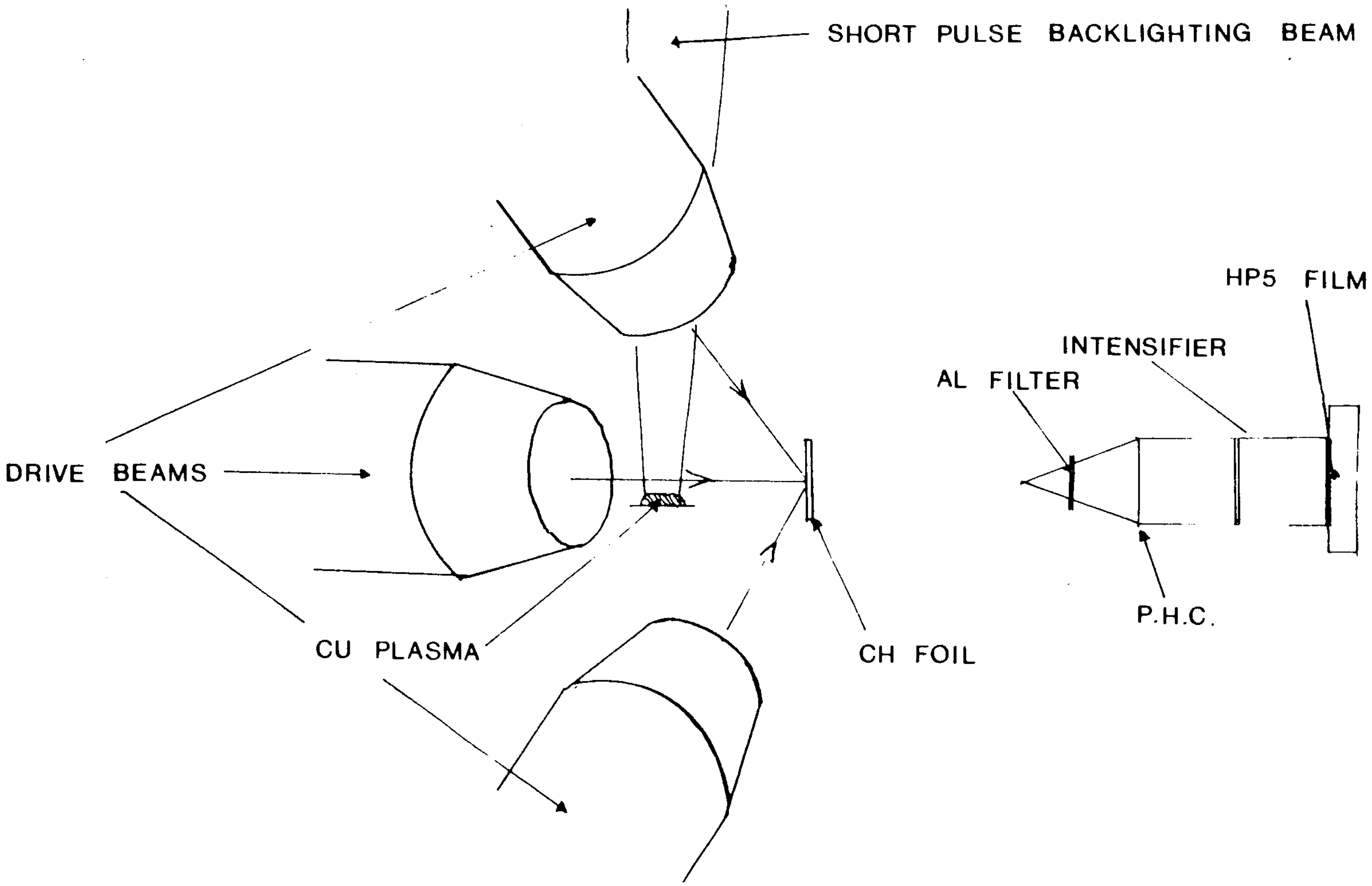

Fig(3.5) Experimental arrangement for backlighting of plastic foils.

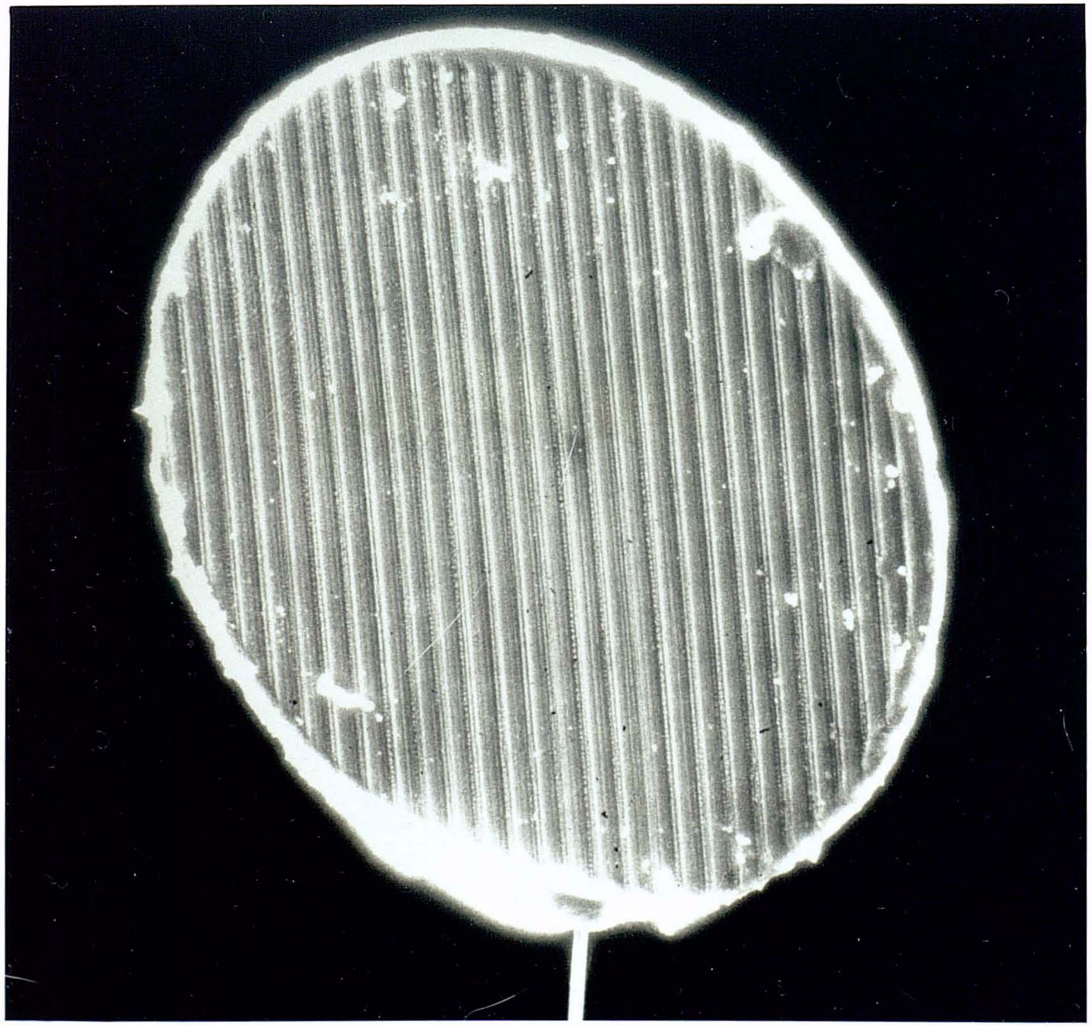

Fig(3.6) A mass modulated foil.

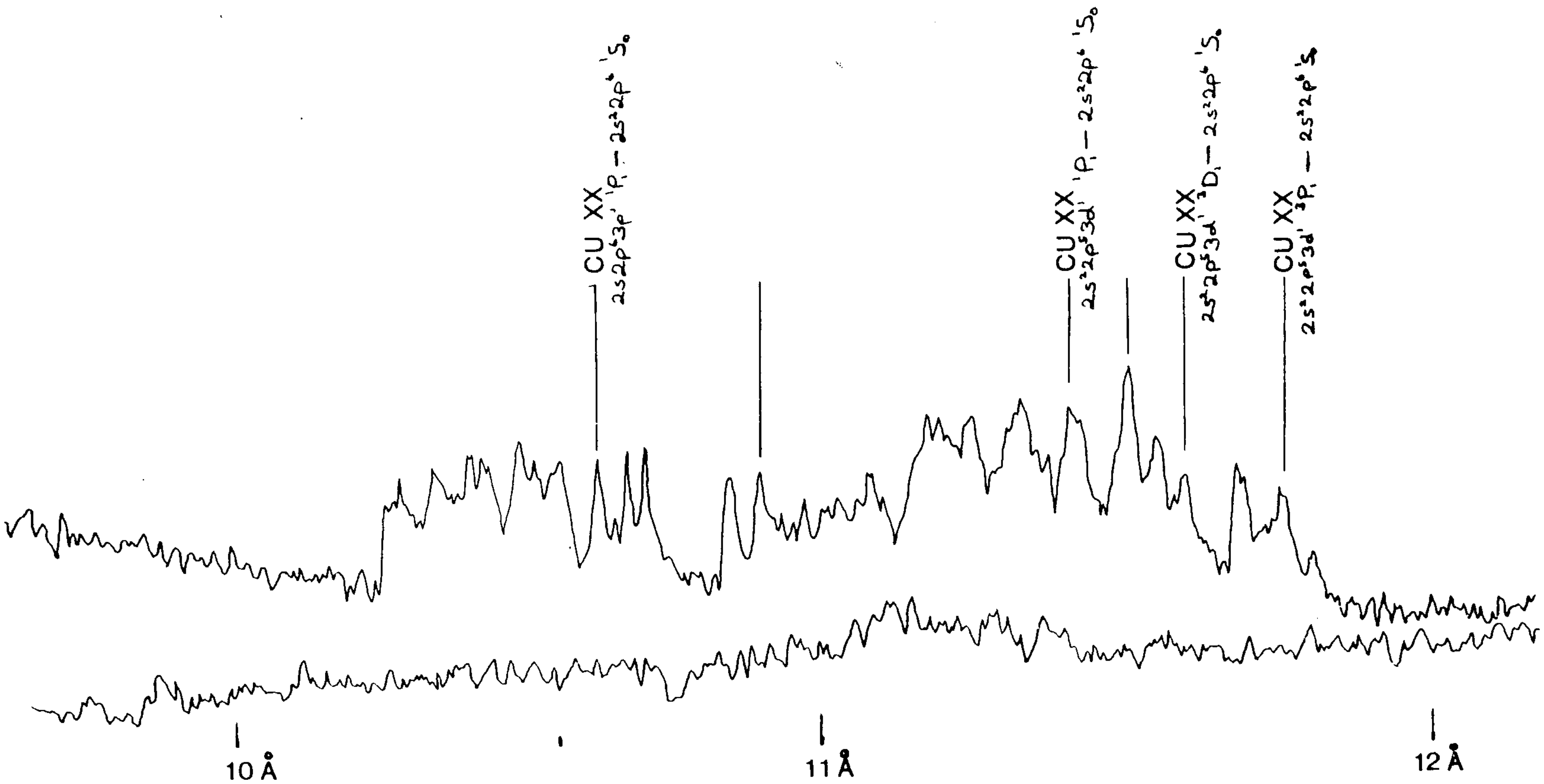

Fig(3.7) The Copper backlighting spectrum.

Lower energies were filtered out using the 3 μm of Al; the k edge of the Al cut off anything above 7.95 Å.

A more important measurement for the results here is that of an average wavelength. An average wavelength was calculated using a filter pack of various thicknesses of mylar beneath 3μm of AL . The results are shown in Fig(3.8). The transmission through the mylar corresponds to wavelength of 10Å.

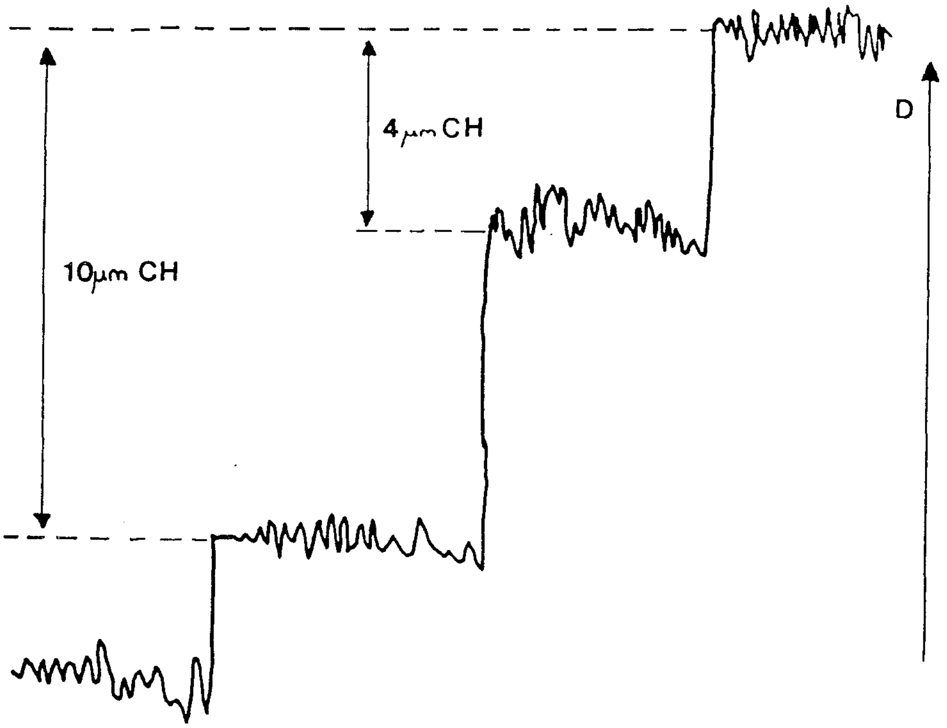

Fig(3.8) Results from the filter pack measurements

3.9 Distance moved by the target

Before looking at the accelerated target in transmission the backlight and pinhole camera were arranged to view the target side-on; thus the distance moved by the target for the given irradiance could be measured. This result is shown in Fig(3.9). The beams were focused on a 250 μm spot, punching a hole in the middle of the target and leaving a stationary anular ring as a reference marker. The target is seen to have moved 60μm after 1ns at an absorbed irradiance of 5×10^{13} Wcm^{-2}.

3.10 Results

The shadowgraphs of the driven foils, along with the illumination conditions are shown in Fig(3.10). The initial target corrugations were vertical, and it can be seen that their integrity has not been maintained. In several of the pictures the transmission of the foil exhibits ring structures.

There are two reasons for believing that the observed ring structures are due to beam effects. First, ring structures of the order of the same scalelength have been measured in the beams at the CLF: Fig(3.11) shows the beam profile of an f/1 beam recorded by Eason(3.24) through the final lens. This ring pattern is due to defects in the final lenses. The lenses were polished in a series of anular rings leaving a small wedge between rings causing the ring pattern. Under the focusing conditions in this experiment the peak to peak distance of the intensity on target would be 30 μm, and the observed rings are about 27±4 μm apart, in good agreement. Secondly, the three orthogonal drive beams are each incident on the target at 56^0, and thus

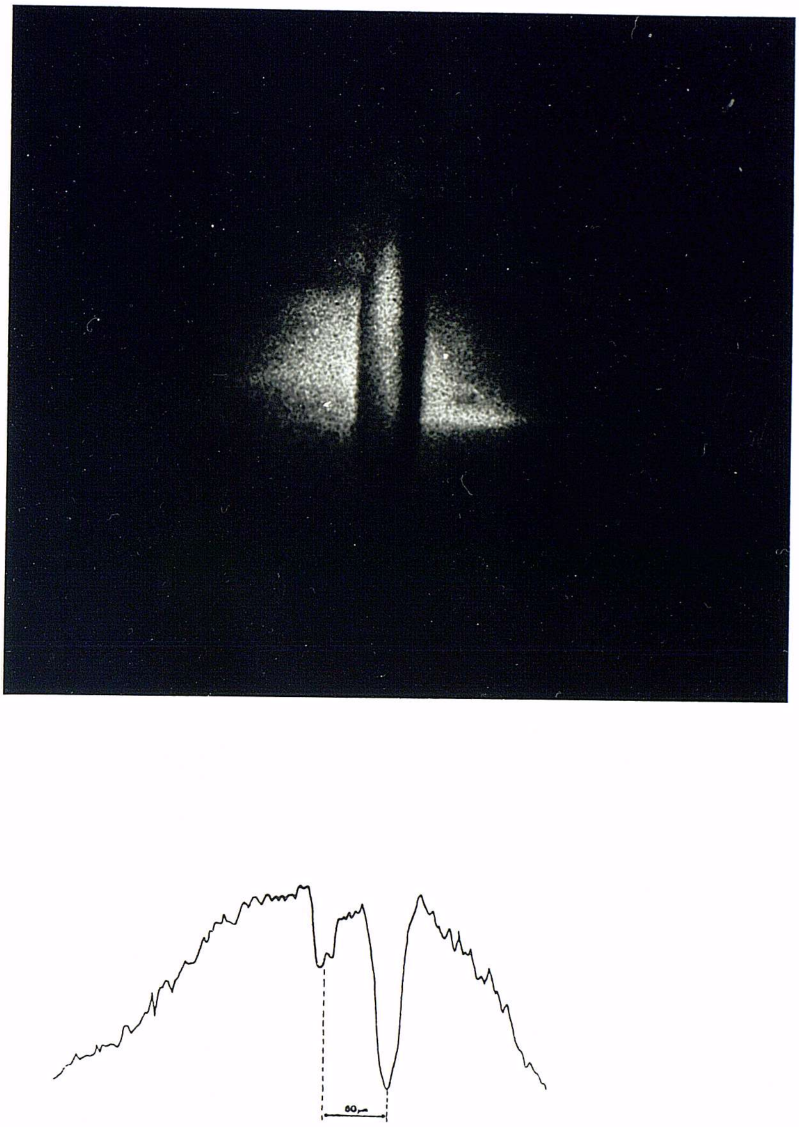

Fig(3.9) Side on backlighting picture of an accelerated foil.

Absorbed irradiance of 5×10^{13}Wcm^{-2}, probed at lns after the beginning of the drive pulse

Shot 06290783, $I_a = 8.5 \times 10^{13}$ Wcm^{-2}

Shot 05280783, $I_a = 9.0 \times 10^{13}$ Wcm^{-2}

Fig(3.10) Shadowgraphs of the driven foils, all the probe times are lns.
The foils are 10μm thick, 300μm diameter plastic.

Shot 08290783, $I_a = 7.1 \times 10^{13}$ Wcm^{-2}

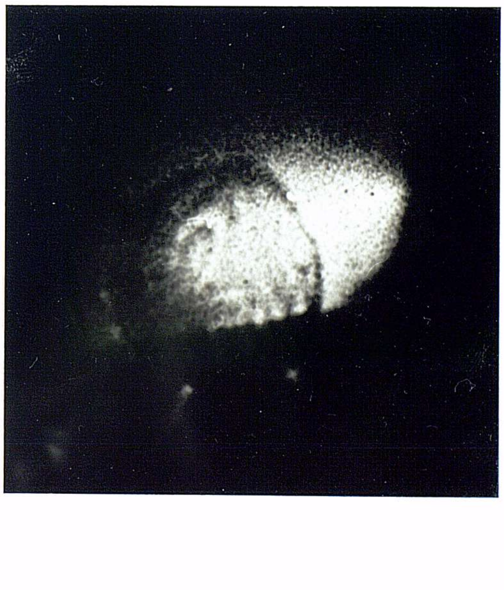

Shot 04290783, $I_a = 10^{14}$ Wcm^{-2}

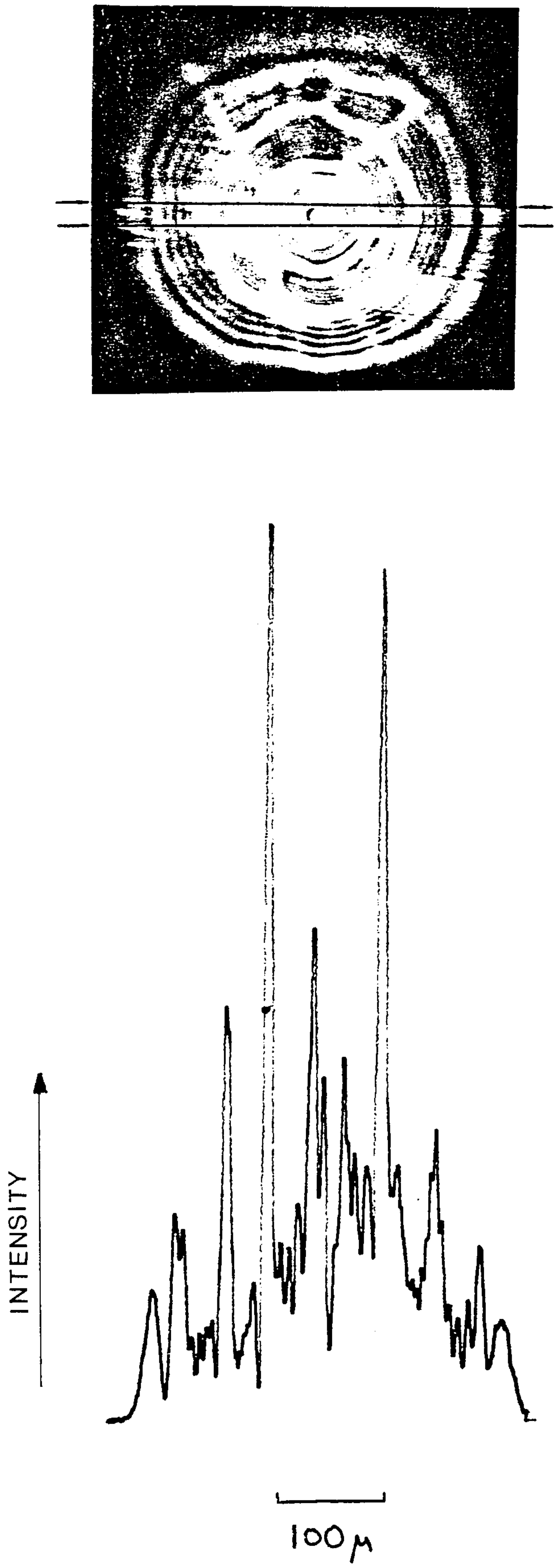

Fig(3.11) Beam profile through one of the f/1 lenses at the CLF from ref (3.24).

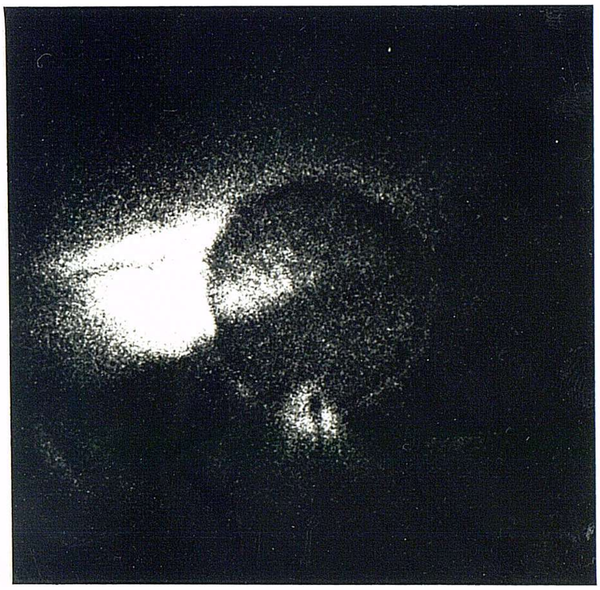

Fig(3.12) Misaligned backlight showing low level of self emission from the target.

a circular ring in the beam would appear as an elipse on the target with a major to minor axis ratio of 1.8. Elipsoidal rings can be seen on the target with axis ratios of 1.6±0.2, in good agreement. Also the pictures show evidence of up to three rings on the target, with the major axes pointing in three different directions, as would be expected.

We note that, with reference to Fig(2.4), no effect of the ring pattern in the beams was seen in the uniformity experiment. Thermal smoothing could possibly have played a role there as the irradiances were higher. However a significant amount of smoothing could not have taken place as the effects of the beam overlaps are still present. Another possible explanation is that refractive smoothing is more effective in spherical geometry, as the rays are incident on the target at larger angles.

Having established that the ring structure is probably due to beam effects it is still necessary to deduce if the variation in transmission of the targets is due to the R-T instabilty. There are two other possible explanations: first, the observed rings are due to self emission on the front surface of the target; secondly, it is totally due to preferential ablation.

The first of these explanations can be discounted from a picture in which the backlight and target were not quite properly aligned, as shown in Fig(3.12). The self emission from the plastic foil can clearly be seen, much fainter than the copper backlight, and no structure is visible in the self emission.

In consideration of the second possible explanation, the mass ablated can be calculated using independently measured ablation rates(1.7) . From these rates we predict that, at the absorbed irradiance of 8×10^{13}Wcm^{-2}, 2.2 µm of the plastic would be ablated after 1ns; and as the ablation rate has been found to scale as $(I_{abs})^{0.36}$ in the ring structure (where the irradiance is a maximum of four times as great) the mass ablated would be increased by a factor of 1.65 to 3.6 µm. Thus the peak to trough of the ρr in transmission would only be 1.4 µm of 1.3gcm^{-3} plastic if preferential ablation were the dominant effect.

However, the $(I)^{0.36}$ scaling in planar geometry occurs due to energy spreading. Well within the beam the ablation rate scaling may approach that of spherical geometry, ie $(I)^{0.72}$. This would lead to amplitudes in ρr of greater than 9µm of solid plastic. From densitometer traces of the backlit foils in conjunction with the filter pack measurements we find that the experimental amplitudes lie between 2 and 9µm of plastic. Thus it may be possible that the observed structure is due to preferential ablation. The differential ablation rate between peak and trough could also be further enhanced by self focusing of the laser beam.

The Rayleigh-Taylor instability could also be playing a role, and its effect was simulated using a 2-D Eulerian code as described below.

3.11 Hydrocode Simulation

Instigation of the R-T instability by non uniformities in the beam has been simulated by Evans et al(3.25). However in their simulations the modulation in the beam intensity were only ±20%, an order of magnitude less than in this case. To investigate the effect of such large variations in the beam intensity the experiment was simulated using the 2-D hydrocode Pollux.

The two dimensional hydrocode, Pollux, used to simulate the experiment was written by Pert(3.26). The code is Eulerian, it solves the hydrodynamic equations closed by an equation of state. Thermal transport across steep temperature gradient is modelled by using a flux limiter. The output of the code is the temperature, density and pressure profiles on a two dimensional grid, usually set to be 100 × 50. The code was run on the Cray-1s at the University of London Computer Centre, and a typical run of 1ns simulation took 1 - 1.5 hours of CPU time. Further details of the code can be found in reference(3.26).

The simulation involved irradiating a plane 10μm thick plastic foil with a modulated beam with a 4:1 intensity ratio as shown in Fig(3.13). A flat foil was chosen to simplify the analysis; if a mass modulated target were used it would be difficult to decompose the effects due to the beam from those due to the initial target perturbations.

The results of the simulation are shown in Fig(3.14).

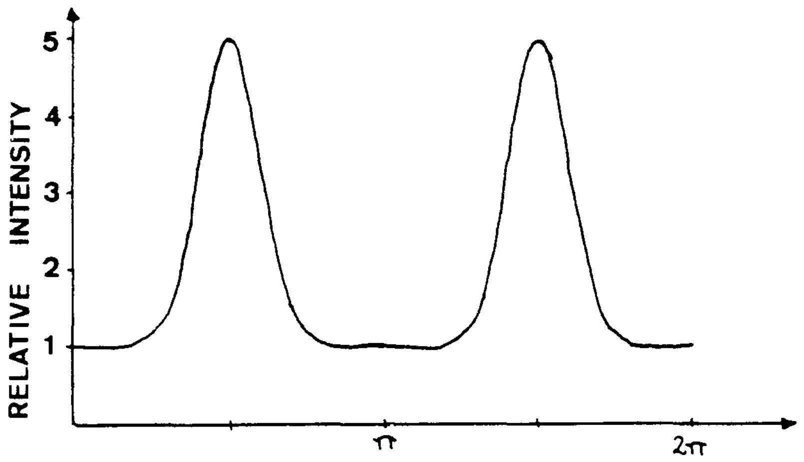

Fig(3.13) Laser beam intensity variation used in the hydrocode simulation.

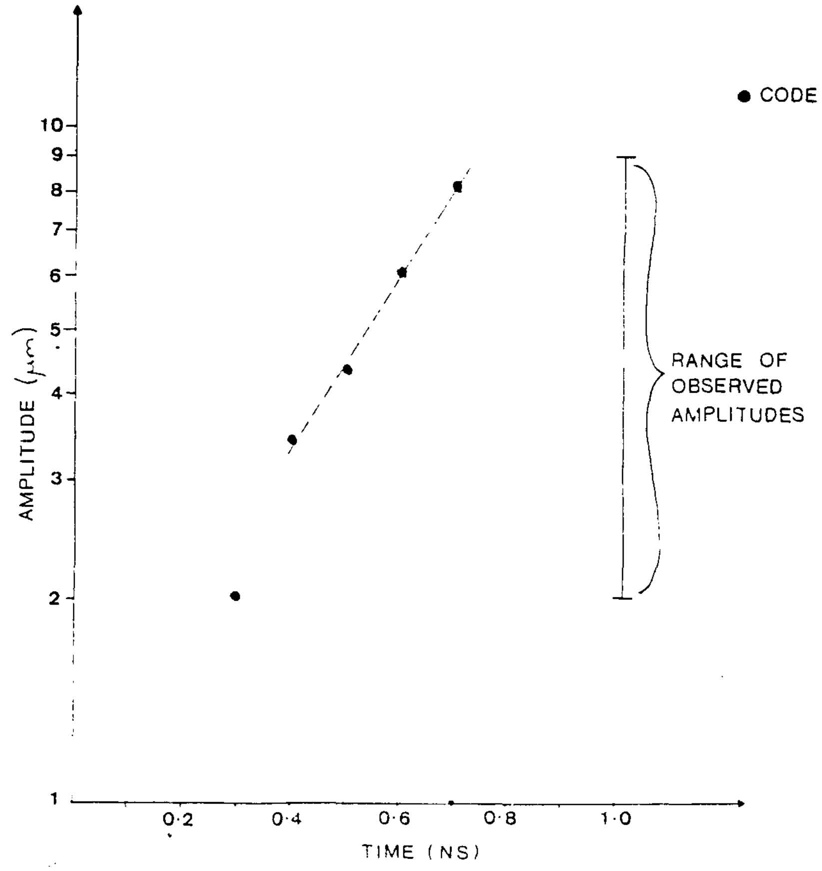

Fig(3.14) Variations in ρr predicted by the hydrocode.

It can be seen that there is an increasing periodic variation in ρr. Some of this variation will be due to preferential ablation; however the R-T instability must also be a factor because the maxima in ρr are greater than the initial target thickness.

We see that the code predicts larger amplitudes than those observed; there are several possible explanations for this. First, due to the limited availibilty of Cray time the code was run for only one value of intensity ratio, 4:1, whereas the amplitudes of the rings in the beam actually vary greatly from 1.5 to 4. The code is not in too great a disagreement with the greatest amplitudes observed.

Secondly there are several processes which are not allowed for in the code, for instance there is no radiative transport; we could conjecture that X-Ray preheat may reduce the growth rate. Also magnetic fields are ignored in the code, these could be important in this experiment as the large non uniformities in irradiance may produce large magnetic fields.

3.12 Discussion

An interesting question arising from these results is why the instability due to the ring structure dominated over that due to the initial mass modulations in the target. Assuming a growth rate of 0.4 of classical we would still expect to see spikes of 10μm amplitude from 1μm initial perturbations after 1ns.

One possible explanation is that with such non uniform illumination magnetic fields are set up that inhibit growth, though this is conjecture, the problem should be addressed by controlled experiments with deliberate modulations in a clean beam. At present there is no immediate answer.

3.13 Conclusion

Variations in the ρr of driven foils, due probably to structure in the beam have been observed. The observed amplitudes are less than those predicted by the 2-D code, "Pollux". This may be due to inaccuracies in the modelling in the code. This experiment shows the necessity of good quality final lenses in ICF experiments.

CHAPTER FOUR

THE R-T INSTABILITY IN IMPLODING MICROBALLOONS

Abstract

Short pulse x-ray backlighting has been used to diagnose ablatively imploded mass-modulated plastic microballoons. Radially protruding spikes have been observed growing at a rate of 0.6±0.05 γ_c. A transmission picture has shown clear evidence of mass redistribution. Reasons for a higher growth rate than that measured by Cole et al are discussed.

4.1 Introduction

The novel laser etching technique described in the previous chapter has, for the first time, enabled mass modulated microballoons to be manufactured. All previous R-T experiments (in the open literature) have taken place in planar geometry. Looking side on to the perturbations allows the shape of the spike to be discerned. Spherical targets were used to facilitate looking side on to the instability; a planar target could buckle or bow due to non uniform drive which could obscure a view of the growing spikes.

4.2 Targets

A typical target is shown in Fig(4.1). The 10μm thick plastic microballoon, of approximately 180μm diameter, has had 20μm periodic bars etched away on one hemisphere with a

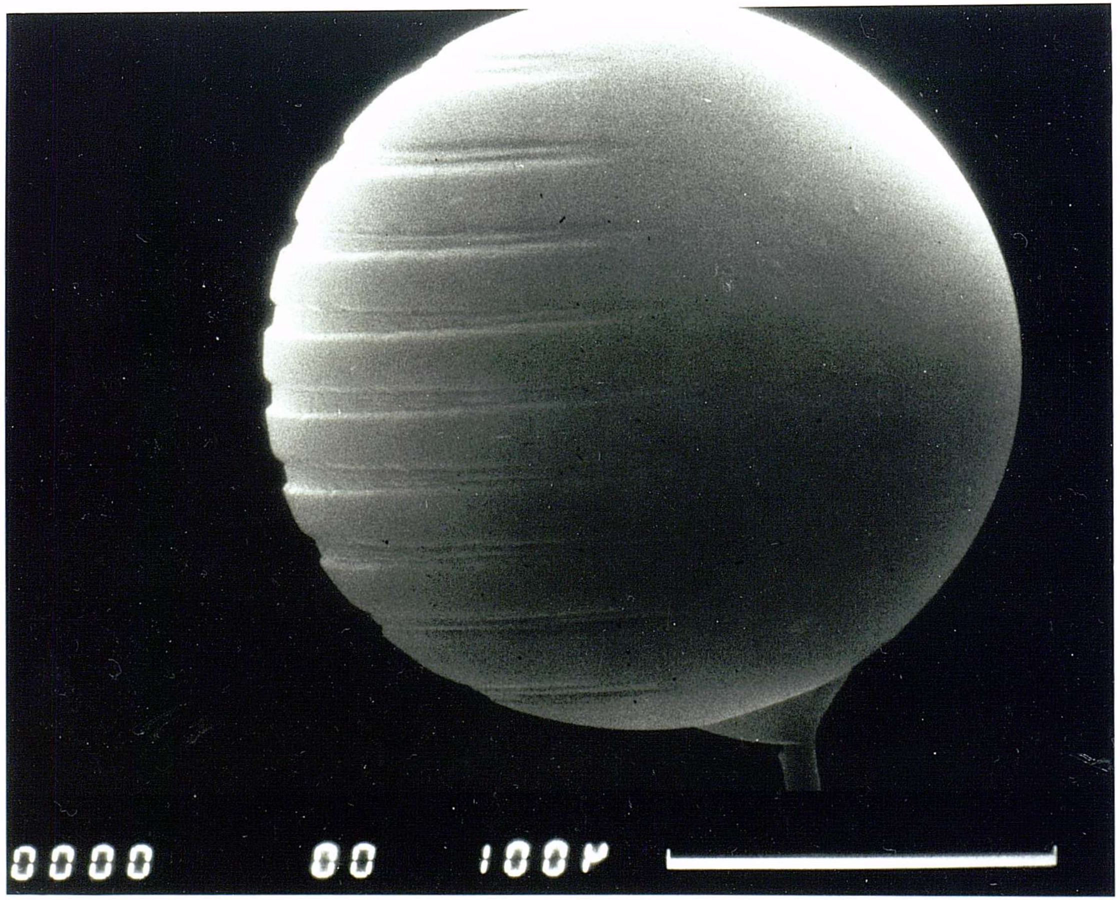

modulation wavelength : 20µm

Fig(4.1) A mass modulated microballoon.

perturbation depth of 2μm. At the time of target manufacture the laser etching technique was in its infancy, and the relationship between the number of shots, laser power, and the resultant etch depth was not well known. This explains the perturbation depth of 2μm, rather higher than would have been liked. Later, however, targets with 1μm perturbation amplitude were manufactured, and the result from such a target is included here.

To look for evidence of mass redistribution it is necessary to look through the microballoon along a line normal to the target surface. To facilitate this a target was manufactured with part of the unetched hemisphere cut away as shown in Fig(4.2).

4.3 The Experimental Set up

The experimental set up is very similar to that used for the planar plastic foil experiment and is shown in Fig(4.3). For the main part of the work the pinhole camera was positioned to look side on to the perturbations.

Three orthogonal 0.53μm beams were used to implode the etched hemisphere. The unetched side of the balloon remained stationary during the time of observation; and this was used as a reference point to determine the distance moved by the shell wall. The three beams were defocused to 4.5 target radii, as defocusing reduces the effects of beam overlap non-uniformities, as discussed in chapter two.

The typical absorbed irradiance, as measured by ion calorimeters, was 2×10^{13}Wcm^{-2} in a pulse length FWHM of 1ns,

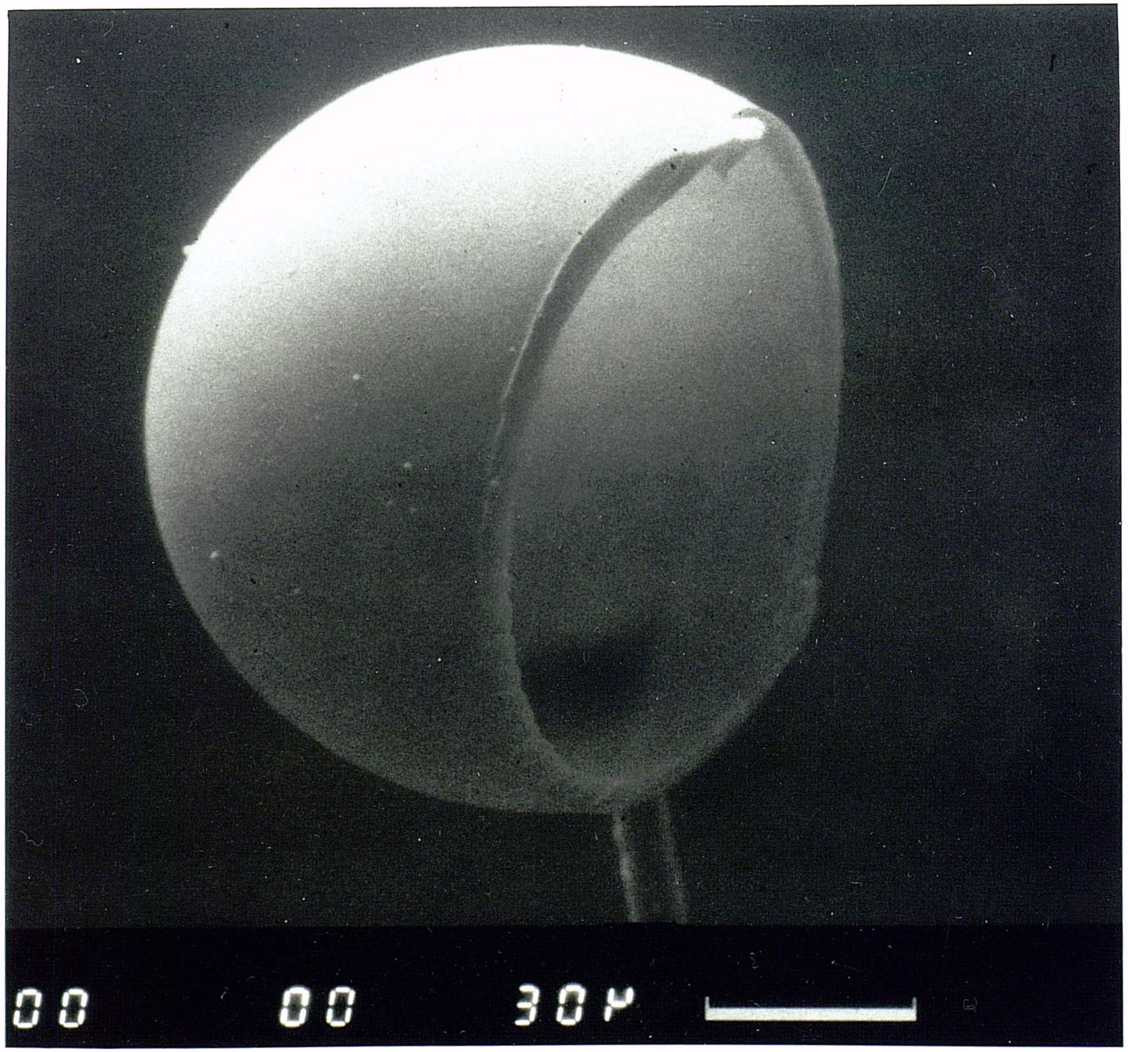

Fig(4.2) Microballoon with back removed to facilitate transmission measurement of the R-T instability.

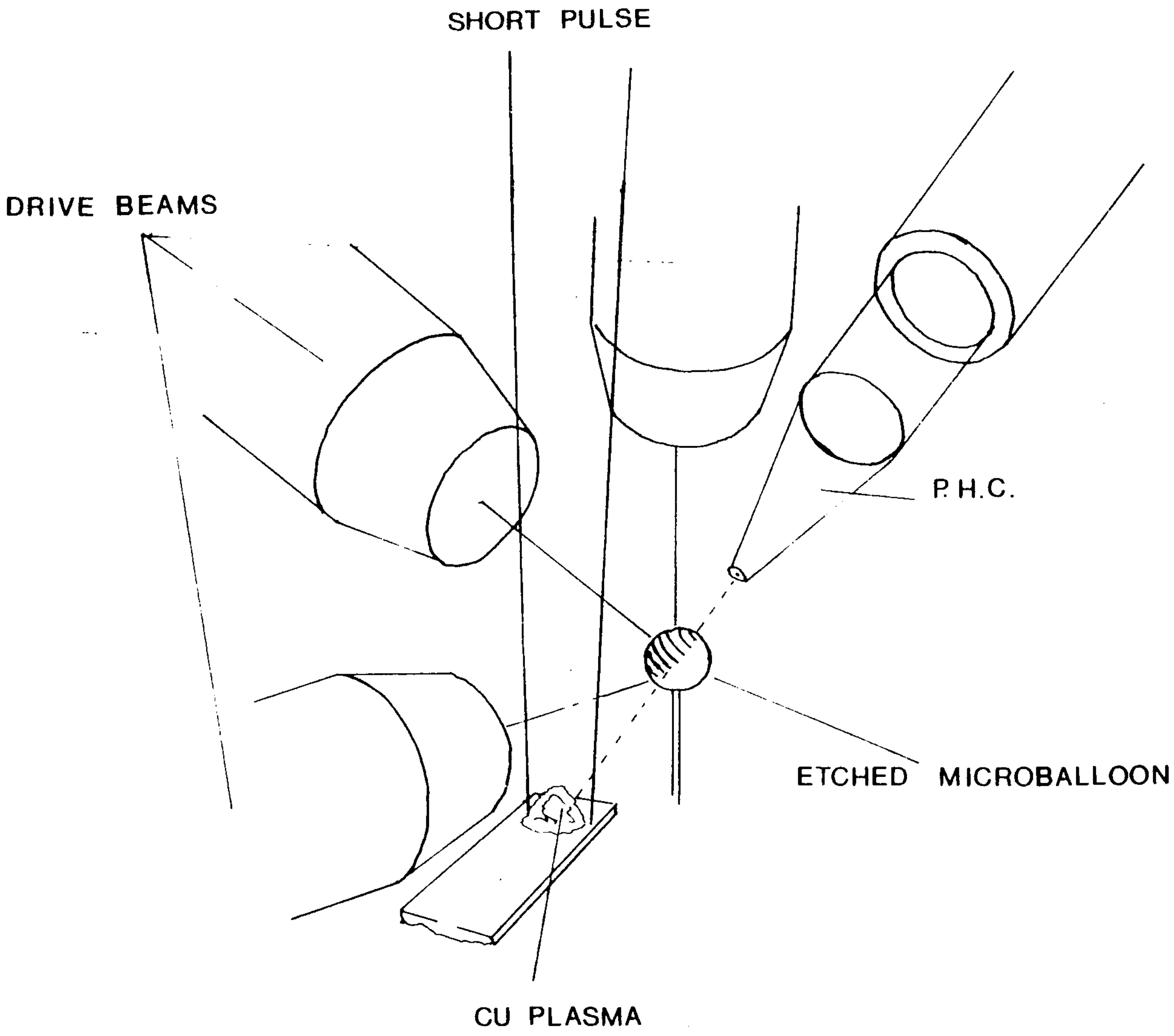

Fig(4.3) Experimental arrangement for the backlighting of mass modulated microballoons.

with a backlight of 30J in 285ps. The pulse lengths were measured using an X-ray streak camera, the results are shown in Fig(4.4). The pinhole size was 8µm and the x-rays were filtered through 3µm of Al onto the phosphor screen at a magnification of 20±1. The magnification was checked by backlighting an unirradiated microballoon of known diameter.

4.4 Results

The x-ray shadowgraphs are shown in Fig(4.5). Radially protruding spikes of the correct periodicity can be seen on the irradiated hemisphere, increasing in amplitude as the backlight is delayed, and the shell implodes further. A summary of the results is tabulated below.

Shot	Initial Pert µm	Distance µm	Average Amp µm	ln(Amp)
03270783	2	4 ± 2	5 ±1	0.92
10280783	2	12 ± 3	13.5±2.5	1.91
14280783	2	25 ± 5	15 ±3	2.01
16280783	2	10 ± 2.5	10 ±2	1.61
19280783	2	8 ± 3	7.5±2	1.32
06220783	2	36 ± 6	19.5±4	2.
05270184	1	20 ± 4	8 ±2	1.95

As the backlight is delayed, the velocity of the imploding shell at the time of observation increases, and the shadow is smeared out in time, causing some loss of resolution. The picture of an unmodulated irradiated hemisphere is shown in Fig(4.6) along with the densitometer tracing through the imploded and stationary side of the sphere. The hemisphere, of original diameter 189µm, has imploded 30µm and it can be seen that time smearing has

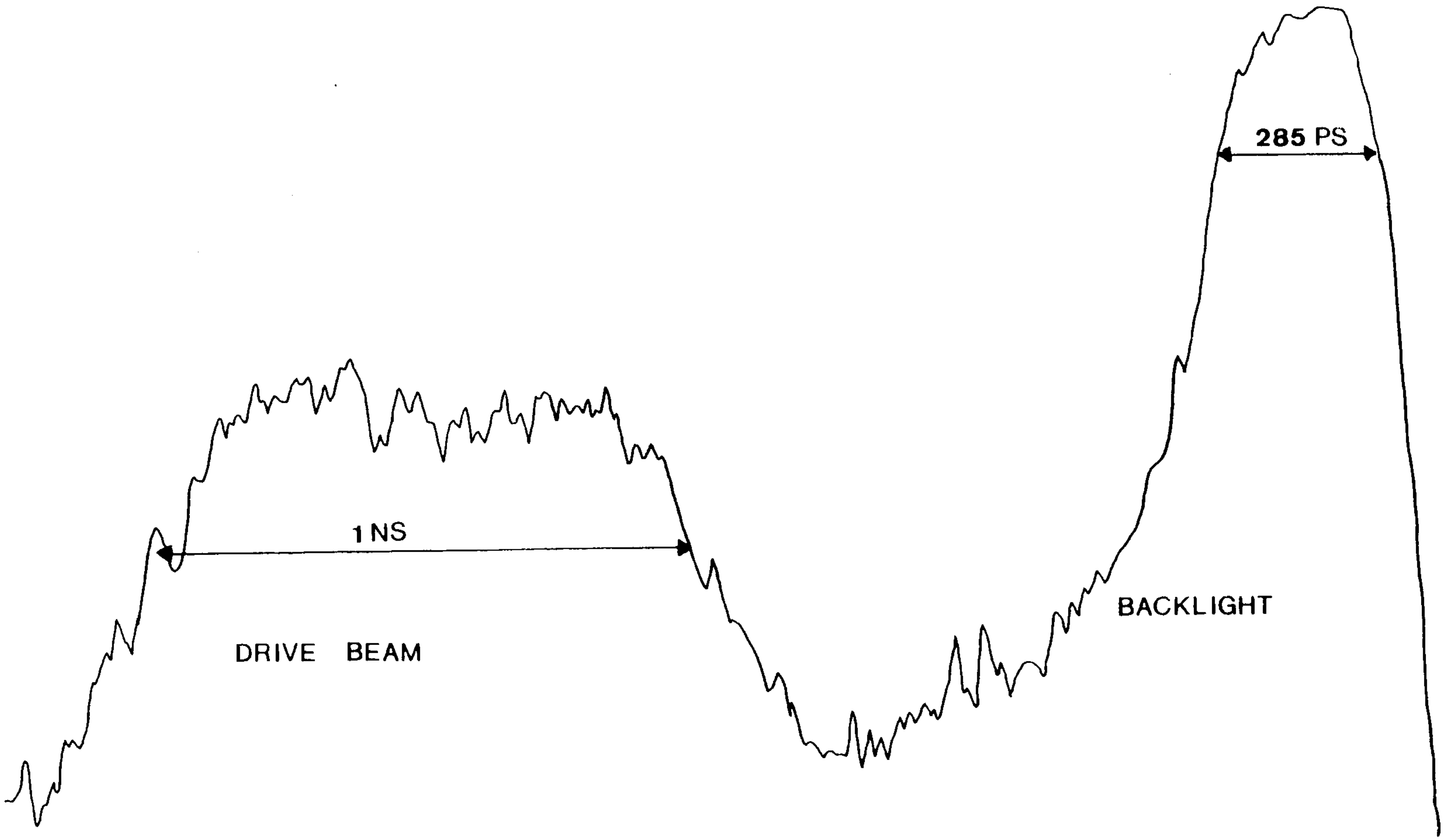

Fig(4.4) Densitometer trace of a streak camera picture of x-rays from the backlighting and drive pulses.

Shot 03270783

Shot 10280783

Fig(4.5) X-ray shadowgraphs of the imploding mass modulated hemispheres.
The typical absorbed irradiances are $2 \times 10^{13} \mathrm{Wcm}^{-2}$.

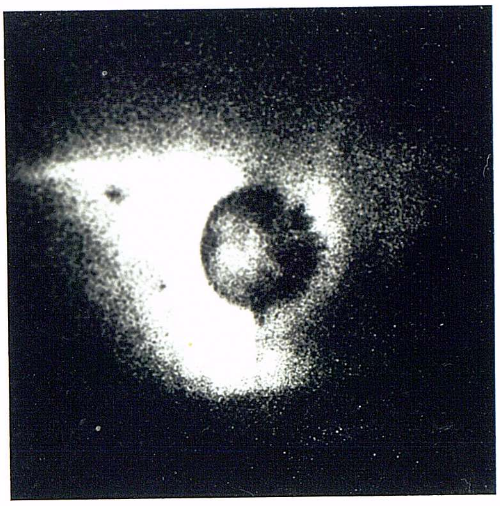

Shot 14280783

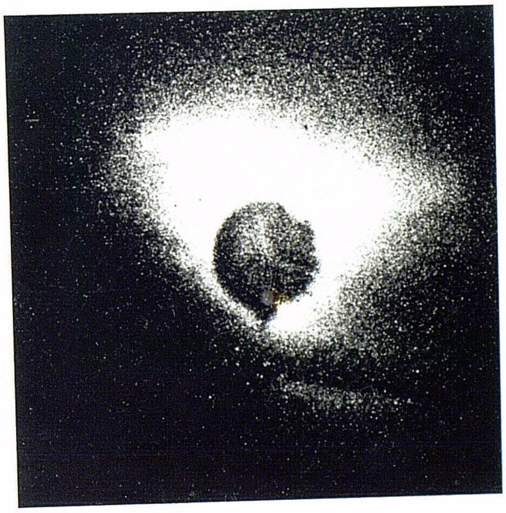

Shot 16280783

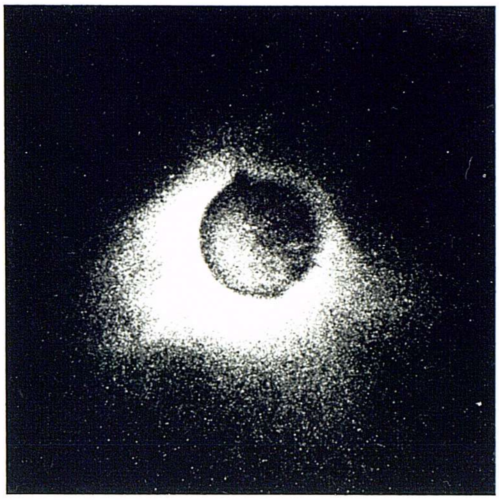

Shot 19280783

Shot 06220783

Shot 05270184

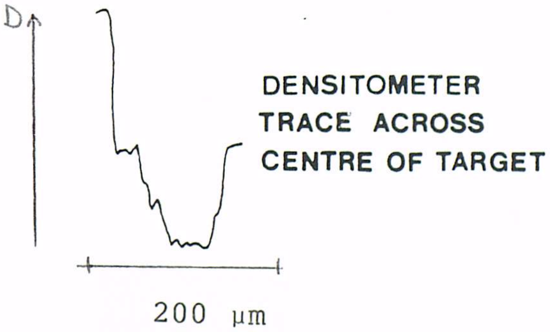

Fig(4.6) Unmodulated irradiated hemisphere showing resolution due to time smearing.

indeed blurred the edge. The resolution of the stationary side is 6±1μm (this is the pinhole resolution) for 10% to 90% transmittance. The same definition applied to the time smeared side gives a resolution of 16μm. However, this definition is quite severe; for 50% transmission the resolution is 10μm.

The furthest an etched hemisphere was observed to implode in this experiment was 36μm, for which we would predict a resolution at 50% transmission of 12μm. The observed spikes were of 20μm amplitude (not taking resolution effects into account); and thus the resolution did not prevent observation of the instability. As the results are two dimensional pictures there is no unique solution for deconvolution with pinhole response. However, we are as much interested in the growth rate as the absolute magnitude of the amplitude, and resolution effects will tend to give rise to errors more in the former than the latter.

As shown in section (3.3) the growth exponent of the classical R-T instability is proportional to $\sqrt{s}$, the square root of the distance moved. The average spike amplitude is plotted as a function of $\sqrt{s}$ in Fig(4.7). The classical growth rate for unit Attwood number, $(2sk)^{1/2}$, is also shown for comparison. From this diagram we conclude that the growth rate is 0.6±0.05 of the classical.

4.5 Comparison with Coles results

This growth rate is double that measured by Cole et al, and we can consider several possible explanations of

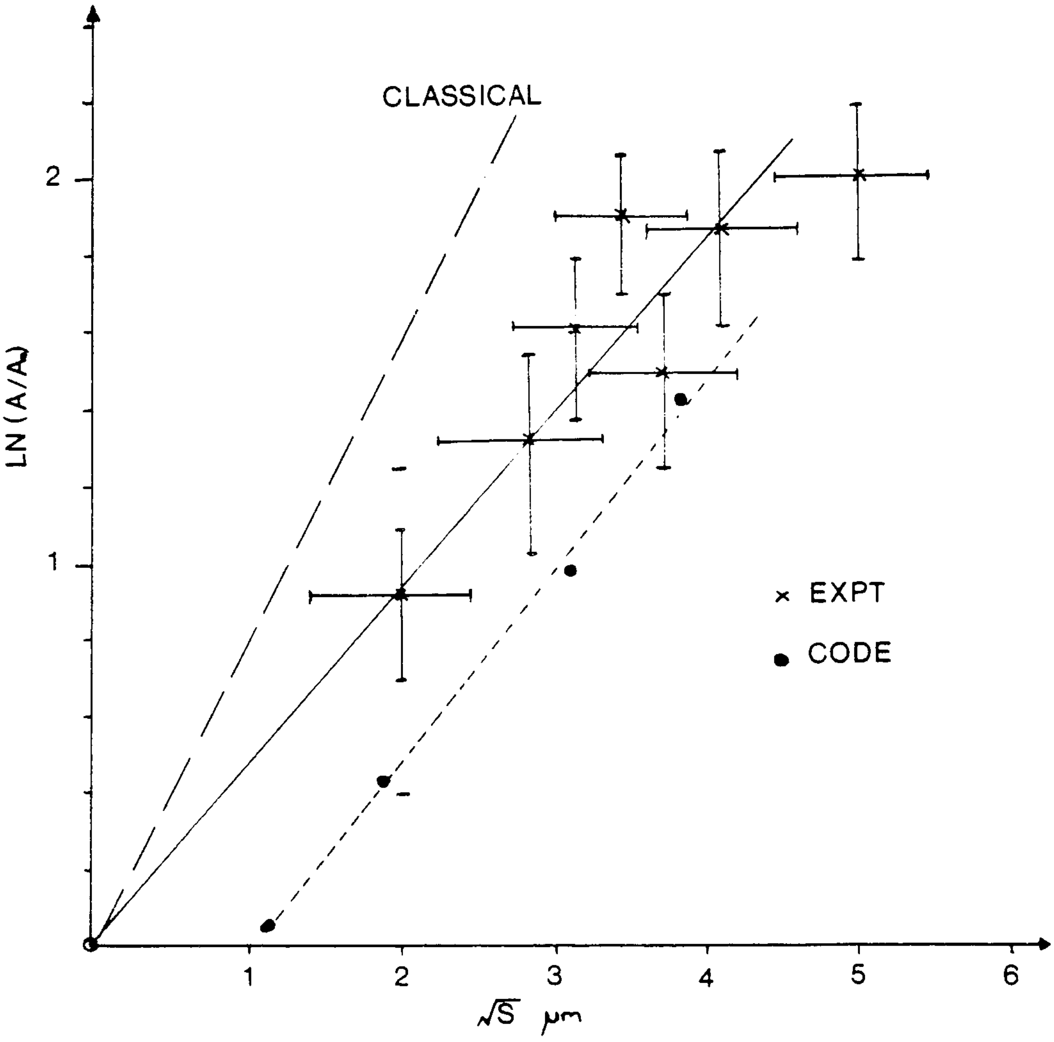

Fig(4.7) Average spike amplitudes plotted as a function of the square root of the distance moved.

this. First we could suppose that spherical effects could be playing a role. As the shell implodes the wavelength of a particular disturbance decreases linearly with the target radius. The furthest the hemisphere was observed to implode was down to (2/3) of its initial radius, i.e. λ decreased by a factor of (2/3) and the growth rate would increase to only $(3/2)^{1/2} = 1.22$ of its initial value. If this effect is integrated up the spike would only be 10% higher at this radius than if spherical effects were not present. Thus this effect cannot explain the higher observed growth rate.

Also, as we are looking side on, not in transmission, spikes would appear on the outside surface of the driven hemisphere due to secular, i.e. non instability, effects. A constant pressure applied to both peaks and troughs of the initial perturbed target would cause an increase in the outside peak to trough amplitude merely due to the different thicknesses, and hence accelerations, that would not show up as an increase in mass length product (i.e. a corrugation rather than a mass modulation).

The initial mass perturbation is 20%, and thus the apparent spikes due to this effect will be 20% of the distance moved; i.e. about 5μm for shot 14280783 where the shell has travelled 25μm, and the observed amplitude is 15μm. If we assume that 5μm of the spike is corrugation, not seen in transmission, then the transmission growth rate would be reduced from 0.6 to 0.41 of the classical, still greater than that observed by Cole et al.

However, there is another spherical effect that could be present (which, in fact, acts to reduce the secular growth). We would expect the target wall thickness to increase as the surface area decreases during the implosion. Obviously there may be some relaxation of this effect due the compressibility of the shell, but we can make an upper estimate. Consider one modulation of the target shown in Fig(4.8); let us apply the same pressure to both peak and trough until the centre of gravity of the trough has travelled 25μm from the initial radius of 90μm.

Referring to Fig(4.8),

$$\Delta r_p' = (90/65)^2 \, \Delta r_p = 15.4\mu m$$

Meanwhile the centre of gravity of the peak will have travelled less due to its smaller mass, it will have travelled

$$0.8 \times 25 = 20\mu m$$

and will therefore have a thickness

$$\left(\frac{91}{91 - 20} \right)^2 \times 10 = 16.4\mu m$$

So we see that the difference in the thicknesses of the peak and trough due to spherical effects are negligible (1μm) in this experiment as the hemisphere has not imploded far enough for spherical effects to become important.

So we see that, looking side on to the spikes may cause us to observe a greater spike growth than

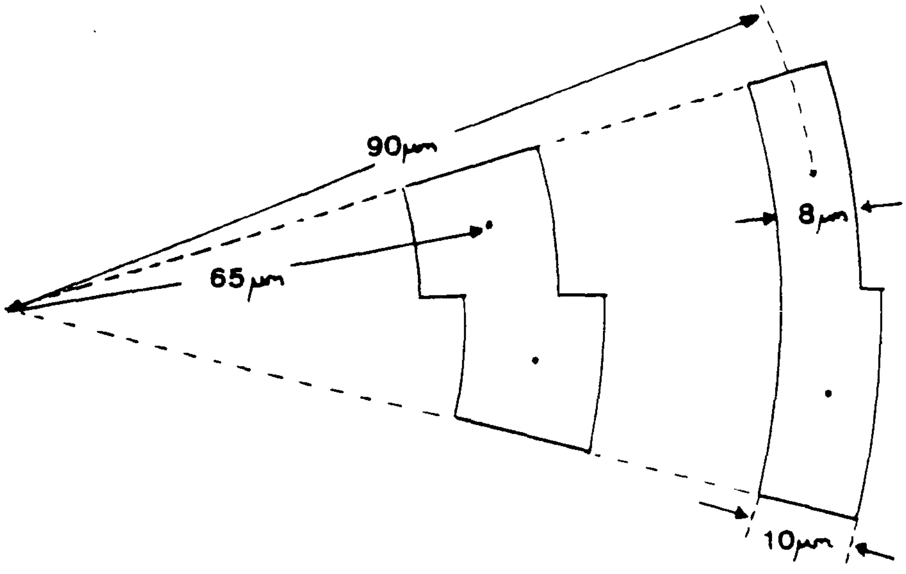

Fig(4.8) Increase in shell thickness due to incompressibility.

in transmission, and at first sight could explain the magnitude of the difference in observed growth rates. However, the model is unrealistic; it assumes that the ablation pressure at peak and trough is uniform, and hence the acceleration at the trough is greater. However, simulations show that the critical surface is modulated far less than the ablation surface during the instability, i.e. the critical to ablation distance is greater at the trough, and the ablation pressure correspondingly reduced; we can see this in the code run shown in Fig(4.11), the rear surface of the foil is still unmodulated after the foil has travelled nearly 10μm showing that the trough is not experiencing a greater acceleration. Alternatively we can look at this in terms of enhanced ablation at the spikes, i.e. firepolishing, as mentioned in reference (3.26). This would tend to nullify these secular effects.

These explantions are also refuted by a transmission measurement of one of the etched imploding hemispheres. The target shown in Fig(4.2) was shot with the backlight and pinhole camera moved so that the camera was looking through the hole in the target onto the inside surface of the irradiated hemisphere, as shown in Fig(4.9). The result is shown in Fig(4.10) along with the associated densitometer tracing.

The hole in the rear surface of the microballoon can clearly be seen, and through it we observe a dark horizontal band corresponding to one of the peaks in the initial mass perturbation. The peak to valley ρr difference is 11 µm of solid plastic. From the irradiance and probe time we can estimate the distance moved by comparison with the side on data to be 20 µm, i.e. a transmission growth rate in ρr of 0.47 of classical. It is not surprising that this is less than the side on growth rate, as we would expect some modulation of the rear surface at this stage in the implosion, i.e. an element of corrugation which gives the appearance of a spike on the outside surface without mass redistribution.

One major difference between this experiment and that of Cole is the target materials used: Aluminium and plastic. A possible explanation is that the Aluminium targets create

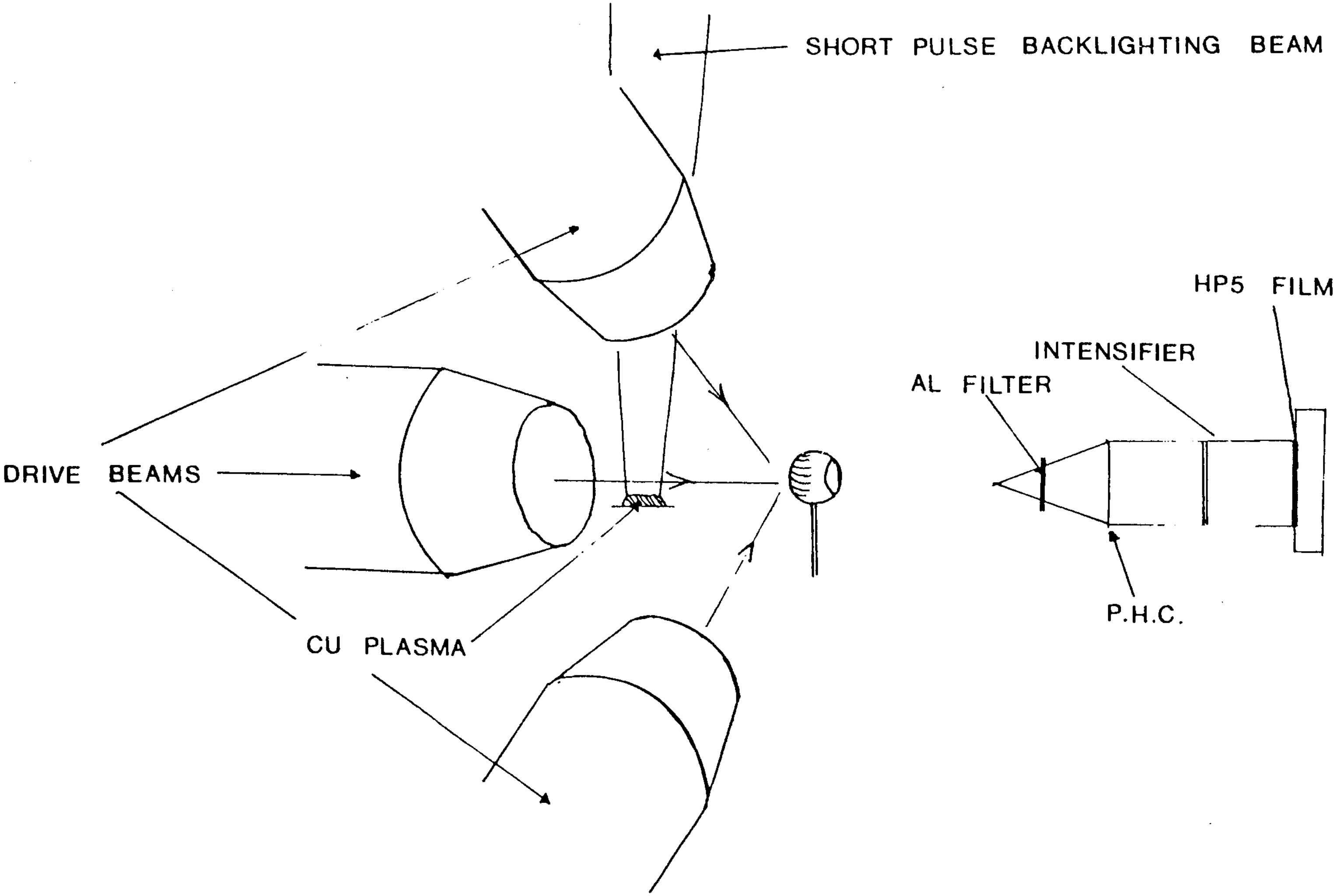

Fig(4.9) Experimental arrangement for the transmission measurement of the R-T instability.

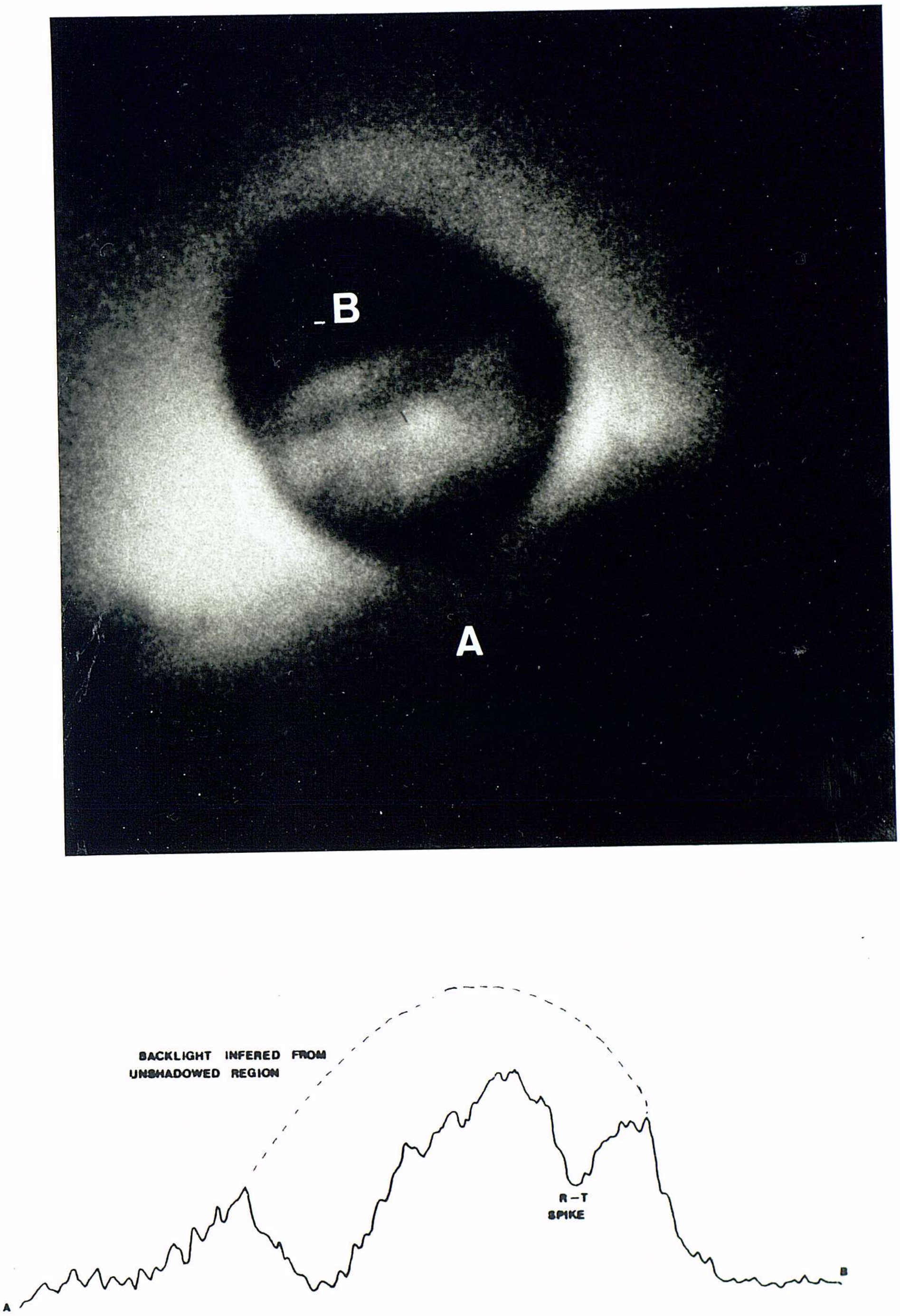

Fig(4.10) View through the hole in the rear of the target to the inside surface of the mass modulated hemisphere.

a larger X-ray preheat due to their larger Z. This preheat could decompress the target, smoothing out the density gradient at the ablation surface, and thus reducing the R-T growth rate.

4.6 Computer Simulation

The 2-D code 'Pollux' was again used to simulate the experiment. Some of the density contours are shown in Fig (4.11), and the peak to trough distance is plotted as a function of $\sqrt{s}$ in Fig(4.7) for comparison with the experimental results. We see that the code is in good agreement to within experimental error, predicting a growth rate of 0.65 of the classical.

It is interesting to note that the code gives good agreement in this case, but not with the results of Chapter Three or the experiment of Cole (who used the same code to simulate his results). The predicted growth rate in all three cases is very nearly the same, but experimentally the observed amplitudes are less for the high irradiance or high Z cases. This is a strong indication that physical processes, such as radiative transport, ignored on the code, may reduce the R-T growth rate.

4.7 Limits on the Aspect Ratio

The results recorded here show that for ablative implosions the growth rate of the R-T instability is 0.6 γ_c. From section (3.3) we recall

$$\gamma t_{max} = (4\pi r/\Delta r)^{1/2} C \qquad (3.26)$$

where we have found C = 0.6. Also

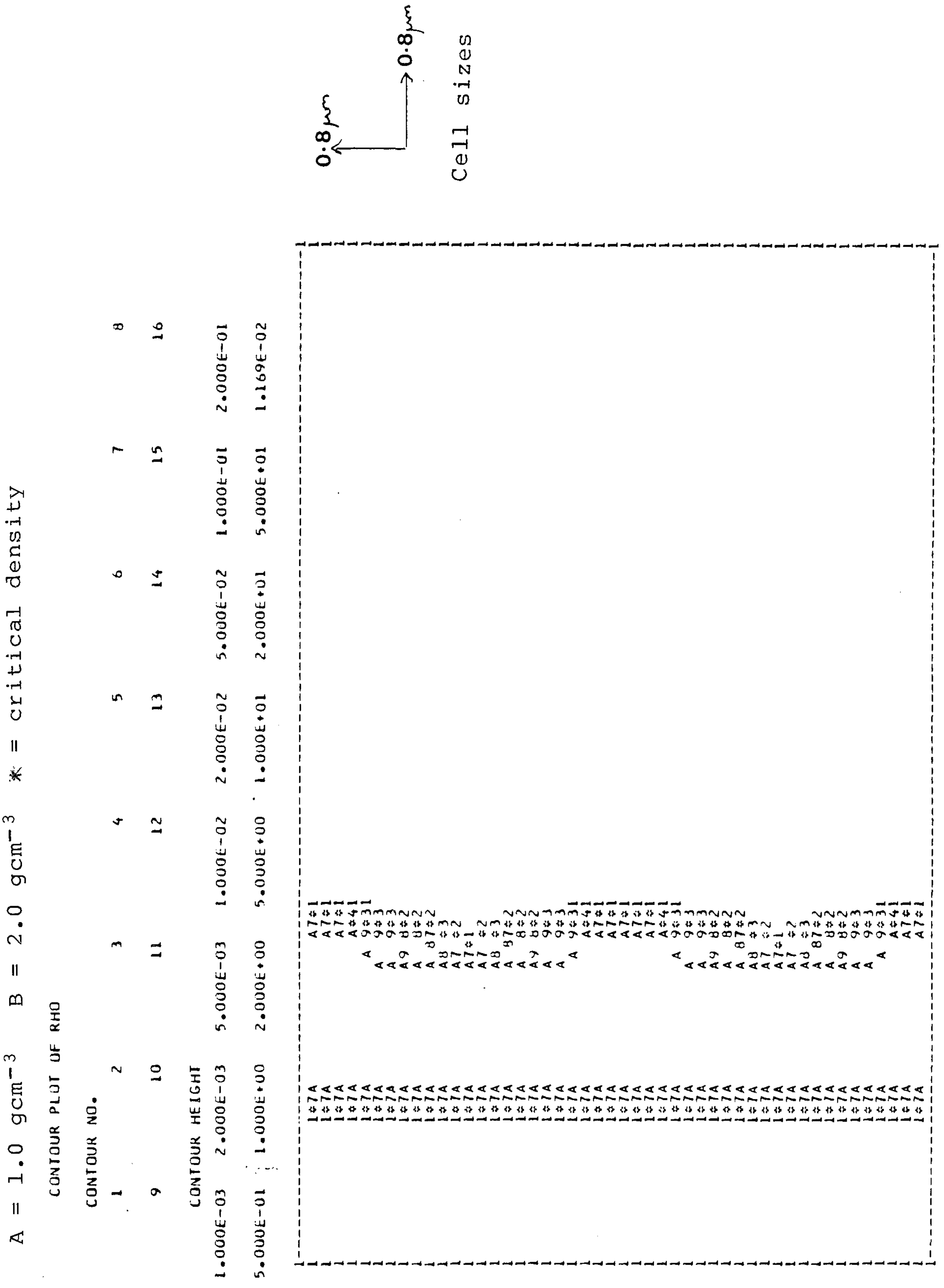

CONTOUR NO.	CONTOUR HEIGHT
1	1.000E-03
2	2.000E-03
3	5.000E-03
4	1.000E-02
5	2.000E-02
6	5.000E-02
7	1.000E-01
8	2.000E-01
9	5.000E-01
10	1.000E+00
11	2.000E+00
12	5.000E+00
13	1.000E+01
14	2.000E+01
15	5.000E+01
16	1.169E-02

Distance moved, s = 0.0μm

Fig(4.11) Density contours from the hydrocode simulation with the distance, s, moved by the target in each case. Planar geometry is used as spherical effects are negligible.

```
        CONTOUR PLOT OF RHO

       CONTOUR NO.
        1           2           3           4           5           6           7           8

        9          10          11          12          13          14          15          16

       CONTOUR HEIGHT
1.000E-03   2.000E-03   5.000E-03   1.000E-02   2.000E-02   5.000E-02   1.000E-01   2.000E-01

5.000E-01   1.000E+00   2.000E+00   5.000E+00   1.000E+01   2.000E+01   5.000E+01   1.159E-02

 1------------------------+---+----------------------------------------------------------------------1
 1         12  3 3 ÷5788     BA976 5  ÷4                              3                              1
 1         12  3 3 ÷579B     BA97  5  ÷4                              3                              1
 1         12  3 3 ÷579B     BA87  5  ÷4                              3                              1
 1         12  3 3 ÷579B     BA86 5   ÷4                              3                              1
 1         12  3 3 ÷57AB   B A876 5   ÷ 4                             3                              1
 1         12  3 3 ÷58AB   BA876  5   ÷ 4                             3                              1
 1         12  3 3 ÷58AB  BA976   5   ÷ 4                             3                              1
 1         12  3 3 ÷68B   BA86    5   ÷ 4                             3                              1
 1         12  3 3 ÷68B   B976    5   ÷ 4                             3                              1
 1         12  3 3 ÷68B  BA9 6   5    ÷ 4                             3                              1
 1         12  3 3 ÷69B  BA8 6   5    ÷ 4                             3                              1
 1         12  3 3 ÷69B  BA86    5    ÷ 4                             3                              1
 1         12  3 3 ÷69B  BA86    5    ÷ 4                             3                              1
 1         12  3 3 ÷69B  BA8 6   5     ÷ 4                            3                              1
 1         12  3 3 ÷69B  BA8 6   5    ÷ 4                             3                              1
 1         12  3 3 ÷69B   B976    5    ÷ 4                            3                              1
 1         12  3 3 ÷68B   BA76    5    ÷4                             3                              1
 1         12  3 3 ÷68B   BA876   5    ÷ 4                             3                             1
 1         12  3 3 ÷58B    B98 6  5    ÷4                             3                              1
 1         12  3 3 ÷58AB   BA976   5   ÷ 4                             3                             1
 1         12  3 3 ÷58AB    BA976  5   ÷4                             3                              1
 1         12  3 3 ÷57AB     BA976 5   ÷4                              3                             1
 1         12  3 3 ÷57AB     BA986 5   ÷4                             3                              1
 1         12  3 3 ÷57AB      BA86 5   ÷4                              3                             1
 1         12  3 3 ÷57AB      BA87 5   ÷4                             3                              1
 1         12  3 3 ÷57AB      BA86 5   ÷4                              3                             1
 1         12  3 3 ÷57AB     BA986 5   ÷4                             3                              1
 1         12  3 3 ÷57AB     BA876 5   ÷ 4                             3                             1
 1         12  3 3 ÷57AB    BA976  5   ÷ 4                            3                              1
 1         12  3 3 ÷58AB   BA876   5   ÷ 4                             3                             1
 1         12  3 3 ÷58AB  BA97 6   5   ÷ 4                            3                              1
 1         12  3 3 ÷58B   BA7 6   5    ÷ 4                             3                             1
 1         12  3 3 ÷68B   B9 6    5    ÷ 4                            3                              1
 1         12  3 3 ÷68B  BA8 6    5    ÷ 4                            3                              1
 1         12  3 3 ÷69B  BA8 6    5    ÷ 4                            3                              1
 1         12  3 3 ÷69B  BA8 6    5    ÷ 4                            3                              1
 1         12  3 3 ÷69B  BA8 6    5    ÷ 4                            3                              1
 1         12  3 3 ÷69B  BA8 6    5    ÷ 4                            3                              1
 1         12  3 3 ÷69B  BA976    5    ÷ 4                            3                              1
 1         12  3 3 ÷69B   BA76    5    ÷ 4                            3                              1
 1         12  3 3 ÷69B   BA876   5    ÷ 4                            3                              1
 1         12  3 3 ÷69B    BA8 6  5    ÷ 4                            3                              1
 1         12  3 3 ÷69B    BA986  5   ÷  4                            3                              1
 1         12  3 3 ÷69B     BA976  5  ÷ 4                             3                              1
 1         12  3 3 ÷6AB      BA976 5  ÷ 4                             3                              1
 1         12  3 3 ÷6AB       BA87 5  ÷ 4                             3                              1
 1         12  3 3 ÷7AB       BA9865  ÷ 4                             3                              1
 1         12  3 3 ÷7AB        BA865  ÷ 4                             3                              1
 1------------------------+-----+--------------------------------------------------------------------1
```

S = 3.8µm

```
        CONTOUR PLOT OF RHO

       CONTOUR NO.
         1           2            3            4            5            6            7            8

         9          10           11           12           13           14           15           16

       CONTOUR HEIGHT
 1.000E-03    2.000E-03    5.000E-03    1.000E-02    2.000E-02    5.000E-02    1.000E-01    2.000E-01

 5.000E-01    1.000E+00    2.000E+00    5.000E+00    1.000E+01    2.000E+01    5.000E+01    1.169E-02

1-----------------------+-----+-+-------------------------------------------------------------------1
1          1 2 ÷6789 A  B    BA986  5   ÷ 4                               3                         1
1          1 23÷5789 A  B    BA986  5   ÷ 4                               3                         1
1          1 23÷6789 A  B    BA986 5    ÷ 4                               3                         1
1          1 23÷6789 A  B   BA986  5   ÷  4                               3                         1
1          1 23÷6789 A B  B A976   5    ÷ 4                               3                         1
1          1 23÷6789A  B  B97 6   5    ÷  4                               3                         1
1          1 23÷6789A  BB A7 6    5    ÷  4                              3                          1
1          12 4÷6789A B BA8 6     5    ÷  4                              3                          1
1          12 ÷578 9A B BA86      5    ÷  4                              3                          1
1          12 ÷579 9A BBA976     5     ÷  4                              3                          1
1          12 ÷678 9A BBA976     5     ÷  4                              3                          1
1          12 ÷6789 A BBA976     5     ÷  4                              3                          1
1          123÷6789 A BBA976     5     ÷  4                              3                          1
1          123÷6789 A BBA976     5     ÷  4                              3                          1
1          123÷6789 A BBA976     5     ÷  4                              3                          1
1          12 ÷6789 A BBA976     5     ÷  4                              3                          1
1          12 ÷678 9A B BA8 6     5    ÷  4                              3                          1
1          12 ÷579 9A B B A7 6    5    ÷ 4                               3                          1
1          12 ÷678 9A B  BA97 6    5   ÷ 4                               3                          1
1          12 ÷678 9A  B  BA9876   5   ÷ 4                               3                          1
1          123÷6789 A  B   B A986  5   ÷ 4                               3                          1
1          12÷56789 A   B    BA986  5  ÷ 4                               3                          1
1          12÷678 9 A   B     BA986 5  ÷ 4                               3                          1
1          13÷678 9 A   B     B A87 5  ÷ 4                               3                          1
1          13÷678 9 A   B     B A976 5 ÷ 4                               3                          1
1          13÷678 9 A   B     B A8765  ÷ 4                               3                          1
1          12÷678 9 A   B     BA986 5  ÷ 4                               3                          1
1          12÷56789 A   B    BA9876 5  ÷ 4                               3                          1
1          123÷6789 A  B   B A98 6  5  ÷ 4                              3                           1
1          12 ÷578 9A  B  BA87 6   5   ÷ 4                              3                           1
1          12 3÷6789A B B A7  6    5   ÷ 4                              3                           1
1          12 3÷6789A B BA8 6      5   ÷ 4                              3                           1
1          12 ÷568 9A BBA97 6     5    ÷ 4                              3                           1
1          12 ÷578 9A BBA976      5    ÷ 4                              3                           1
1          12 ÷578 9A BBA976      5    ÷ 4                             3                            1
1          12 ÷6789 A BBA976     5     ÷ 4                             3                            1
1          123÷6789 A BBA976     5     ÷ 4                             3                            1
1          123÷6789 A BBA976     5     ÷ 4                            3                             1
1          123÷6789 A BBA986      5    ÷ 4                            3                             1
1          12÷56789 A B BA9 6     5    ÷ 4                            3                             1
1          12÷56789 A B B A8 6    5    ÷ 4                           3                              1
1          13÷678 9A  B  B A876   5    ÷ 4                          3                               1
1         12÷5678 9A   B   BA976   5   ÷ 4                          3                               1
1         13÷ 6789 A   B    BA9876 5   ÷4                           3                               1
1         24÷67 89  A  B     B A976 5 ÷ 4                           3                               1
1         2÷5678 9  A  B       BA97 5 ÷ 4                          3                                1
1         2÷5678 9  A  B       B A865 ÷ 4                          3                                1
1         2÷567 89  A  B        BA97 5÷ 4                          3                                1
1-----------------------+-------++------------------------------------------------------------------1
```

S = 10.0μm

```
        CONTOUR PLOT OF RHO

       CONTOUR NO.
        1           2           3           4           5           6           7           8

        9          10          11          12          13          14          15          16

       CONTOUR HEIGHT
1.000E-03   2.000E-03   5.000E-03   1.000E-02   2.000E-02   5.000E-02   1.000E-01   2.000E-01

5.000E-01   1.000E+00   2.000E+00   5.000E+00   1.000E+01   2.000E+01   5.000E+01   1.169E-02

 1---------------------+---------+-+----------------------------------------------------------------1
 1       13*5 6 78  9   A B    B A876  5     *  4                                       3           1
 1       13*5 6 7 8 9  AB       3A776  5    *   4                                       3           1
 1       134* 6 7 8 9  AB   B    A87  5     *   4                                       3           1
 1        24*56 7 8 9 AB   BA  987 6  5     *   4                                       3           1
 1        24*56 7 8 9A b BA966   6   5      *   4                                       3           1
 1        23*5 67 8 9AB BA8 6        5      *   4                                       3           1
 1        23*5 67 89A BBA976        5       *   4                                       3           1
 1        23*5 67 89A  A9876        5       *   4                                       3           1
 1        23*5 678 9A  A87 6       5        *   4                                       3           1
 1        23*5 678 A  A9876        5        *  4                                        3           1
 1        23*5 6789A   A976        5        *  4                                        3           1
 1        24*5 6789A   A986       5         *  4                                        3           1
 1        24*5 6789A   A986        5        *  4                                        3           1
 1        24*56 78 A   A986        5        *  4                                        3           1
 1        24*56 78 A   A986        5        *  4                                        3           1
 1        34* 6 78 9A  A986        5        *  4                                        3           1
 1       13*5 6 78 9ABBA98 6        5       *  4                                        3           1
 1      123*5 6 78 9AB BA98 6       5      *  4                                         3           1
 1      23*5  67 8 9 AB  B9 6        5     *  4                                         3           1
 1     2 3*5 6 7 8 9 AB   B986  6     5    *  4                                         3           1
 1     234*5 67 8  9  AB   BA9 87  6  5    *  4                                         3           1
 1    123*5 6 7 8  9  A B   B   A9876  5   * 4                                          3           1
 1    123*5 6 7 8  9   AB       B A987 5   * 4                                          3           1
 1    123*5 6 7 8  9   AB        b A986 5  * 4                                         3            1
 1    123*5 6 7 8 9    AB         BA987 5  * 4                                         3            1
 1    123*5 6 7 8 9    AB         BA967 5  * 4                                         3            1
 1    123*5 6 7 8 9   A B       B  A976 5  * 4                                         3            1
 1    123*5 6 7 8  9  AB   B     A9876 5   * 4                                         3            1
 1    123*5 6 7 8  9 A B  B97     7 6  5   * 4                                         3            1
 1     234*5 6 78  9 AB BA8      6    5    * 4                                         3            1
 1     123*5 6 7 8 9AB BA8 6          5    * 4                                         3            1
 1      23 *5 6 78 9A  A98 6         5     * 4                                         3            1
 1       23*5 6 78 9A A9876         5      * 4                                         3            1
 1        24*5 6789A  A9876         5      * 4                                         3            1
 1        24*5 6789A   A976        5       * 4                                         3            1
 1        34*56 789A   A986        5      *  4                                          3           1
 1       23*5 6 789A   A986        5      *  4                                          3           1
 1      123*5 6 78 9A  A987        5      *  4                                          3           1
 1      234*5 67 8 9A  A9876       5      *  4                                          3           1
 1     23 *5 6 7 8 9AB BA87 6       5     *  4                                          3           1
 1    1234*5 67 8  9AB  BA97 6      5     *  4                                           3          1
 1    2 3*5 6 7 8  9 AB  BA98 6      5    * 4                                            3          1
 1    23 *5 6 7 8  9 AB   B A 97 6   5    * 4                                            3          1
 1   123 *5 6 7 8  9  AB    B  A9876  5   * 4                                             3         1
 1   1234*5 6 78   9  AB       B  A976 5 *  4                                             3         1
 1   1234*5 6 7 8  9  AB          BA986 5 *4                                              3         1
 1   2 34*5 6 7 8  9  AB           BA9865 *4                                              3         1
 1   2 34*5 6 7 8  9  AB            BA975 *4                                              3         1
 1---------------------------------+----------------------------------------------------------------1
```

S = 14.9μm

$$A = A_0 e^{\gamma t} \qquad (1.22)$$

The restriction on aspect ratio is obviously, therefore, a function of the initial perturbation. Let

$$A_0 = f\Delta r \qquad (4.1)$$

$$A_{max} = 2\ \Delta r \qquad (4.2)$$

then we find

$$2 = f e^{\gamma t} \qquad (4.3)$$

i.e.

$$\gamma t_{max} = C(4\pi r/\Delta r)^{1/2} = \ln(2/f) \qquad (4.4)$$

$$\frac{r}{\Delta r} = \frac{1}{4\pi}\left[\frac{\ln(2/f)}{C}\right]^2 \qquad (4.5)$$

The aspect ratio is plotted against various values of f in Fig(4.12) . We can look upon f as an effective initial perturbation amplitude which is related to the smoothness of the target or illumination uniformity via thermal smoothing, ablation effects etc. This requires further experiments using modulations in the beam to instigate the instability.

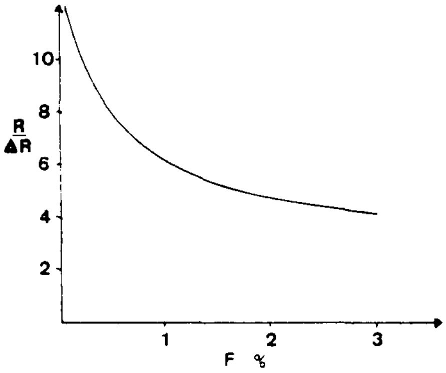

Fig(4.12) Aspect ratio as a function of effective initial perturbation.

4.8 Conclusion

The R-T growth rate for plastic ablatively driven hemispheres has been measured to be 0.6±0.05 γ_c. A transmission measurement has shown clear evidence of mass redistribution, the hallmark of the R-T instability. The results are in good agreement with the 2-D code 'Pollux'. The growth rate could be greater than that measured by Cole et al due to less radiative preheat, but further experiments will be needed to qualify this.

CHAPTER FIVE

ALPHA PARTICLE BACKLIGHTING

Abstract

The concept of alpha particle backlighting is discussed and compared with the conventional technique of x-ray backlighting. Basic experimental conditions and constraints are derived, and the effect of realistic density and temperature profiles of the driven targets on the energy loss of the alpha particles is investigated. The first residual range spectra of laser accelerated targets backlit with alpha particles are presented. They show evidence of mass redistribution indicative of the R-T instability. This novel technique is thus proved to be feasible as a valuable complement to conventional methods of ρr measurements.

5.1 Introduction

Previous successful experimental studies of the R-T instability in laser accelerated targets have all employed the technique of X-ray backlighting. However, this technique has several inherent difficulties and limitations. First, spatial resolution is limited to 5μm by pinhole manufacturing methods. Secondly the backlight is not purely monochromatic (unless point projection spectrally resolved backlighting is used, as will be described in the next chapter), which leads to difficulties in ascertaining accurately how the mass is distributed within the target. Thirdly, the X-ray backlight is not a uniform source, it may contain hot spots of emission due to non uniformities in the laser beam (this also may be overcome by point projection). Fourthly the temporal resolution is limited to at best 100ps (and is typically 200ps) by the length of the short pulse laser beam. Lastly, the noise level is too high to study the R-T instability in the very early stages. For instance, looking through a 10μm plastic foil with an R-T bubble and spike of amplitude 0.5μm with 10Å X-rays would show up as a modulation of 0.02 in density on Ilford HP5 film after processing using a phosphor screen and image intensifier; whereas the typical noise level from a 300μm Cu backlight is often four times greater than that (see Fig(4.10)); although a point source backlight recorded on film may overcome this.

5.2 The concept of alpha particle backlighting

The technique of alpha particle backlighting has been proposed as a means of overcoming some of the drawbacks of X-ray backlighting outlined above at the expense of lateral spatial resolution (5.1).

The basic concept is to illuminate the target with a short burst of monoenergetic alpha particles, rather than with X-rays; the source of alphas being an exploding pusher, and the detector CR39 plastic as will be described below.

Thin-walled D-T filled microballoons imploded at high irradiance (10^{15}Wcm^{-2}), i.e. in the exploding pusher mode,

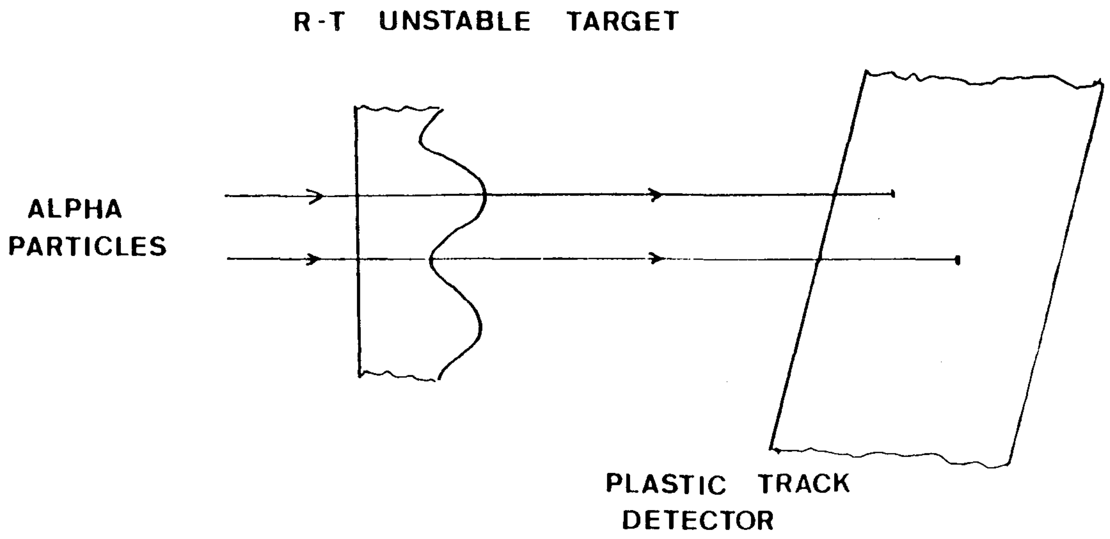

Fig(5.1) The basic concept of alpha particle backlighting to detect the R-T instability.

have long been known to initiate the fusion reaction, albeit at densities too low for energy applications. Alpha particle yields of between 10^6 and 10^7 are routinely produced at the CLF. The alpha particles emitted from the fusion core have an energy of 3.5 Mev with a Doppler spread of ±20Kev due to the temperature of ~ 1Kev in the core. Thus the backlight is highly monochromatic.

The alphas pass through the target, as shown in Fig(5.1), depositing energy on the way, and their residual range is measured using CR39 plastic track detector. A knowledge of their residual range allows the ρr in the target to be determined.

If the alphas pass through a plane foil of uniform ρr then the residual range spectrum in CR39 will simply be the normal Doppler broadened spectrum shifted to shorter ranges by a function of $(\rho r/\rho_{cr^{39}})$. If, however, there is a variation in ρr due to the R-T instability some alphas will pass through a spike and will have less residual range in CR39 whereas others will pass through a bubble and thus have greater range in the CR39; thus the range spectrum will be altered.

5.3 The CR39 Plastic Track Detector

The discovery by Cartwright et al (5.2) of the plastic CR39 presented a major change in the role of plastic track detectors due to its high sensitivity and uniformity of response. When a charged particle traverses the plastic it leaves a trail of chemical damage. When the plastic is subsequently chemically etched in a bath of NaOH the damaged region is preferentially etched away revealing a pit corresponding to the path of the impinging particle. Henshaw and Fews (5.3)(5.4) have shown that detailed analysis of the parameters of the etched pit is an accurate method of determining the energy of the alpha particle to better than 20Kev, i.e. a ρr of 0.2 gcm^{-3}μm. The shape of a typical etched track is shown in Fig(5.2) along with parameters from which the particle range can be determined.

Fews has used the detector to analyse fusion products in ablatively driven implosions at the CLF (5.5)(5.6); and the detector has also been used to measure the range of alpha particles in hot (100ev) matter (5.7).

The 3.5Mev alphas have a range of 17.5 μm in CR39, with a straggling of 0.2 μm (5.3); thus targets with an average ρr of the order 8 gcm^{-3}μm are ideal candidates for this type of backlighting, which is the same sort of thickness as the ablatively driven targets studied at the CLF.

5.4 Experimental Set up

The experimental set-up is shown in Fig(5.3). The thin-walled D-T microballoon was irradiated with 60 J of 1.06μm light in a pulse length of 100 ps FWHM. The alpha particle yield was between 10^6 and 4×10^6 into 4π steradians. The three short pulse beams producing the exploding pusher could be delayed with respect to the long pulse beams accelerating the foil thus enabling the instability to be

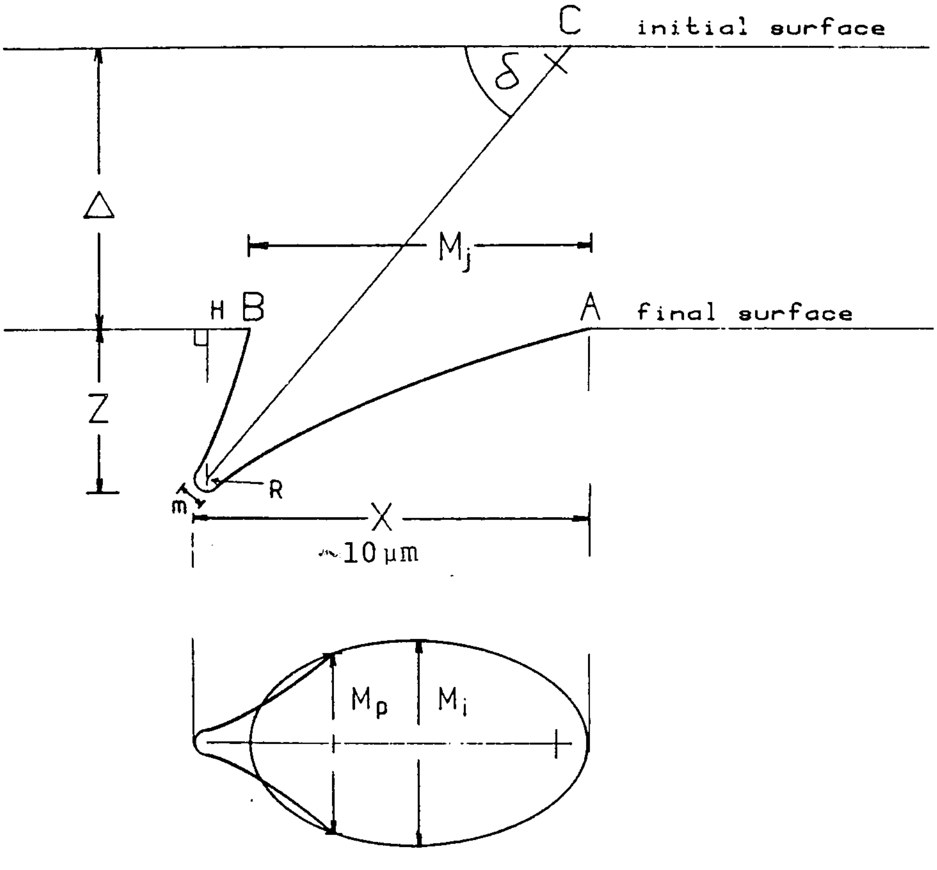

Fig(5.2) The shape of a typical etched track along with the parameters from which the range may be determined.

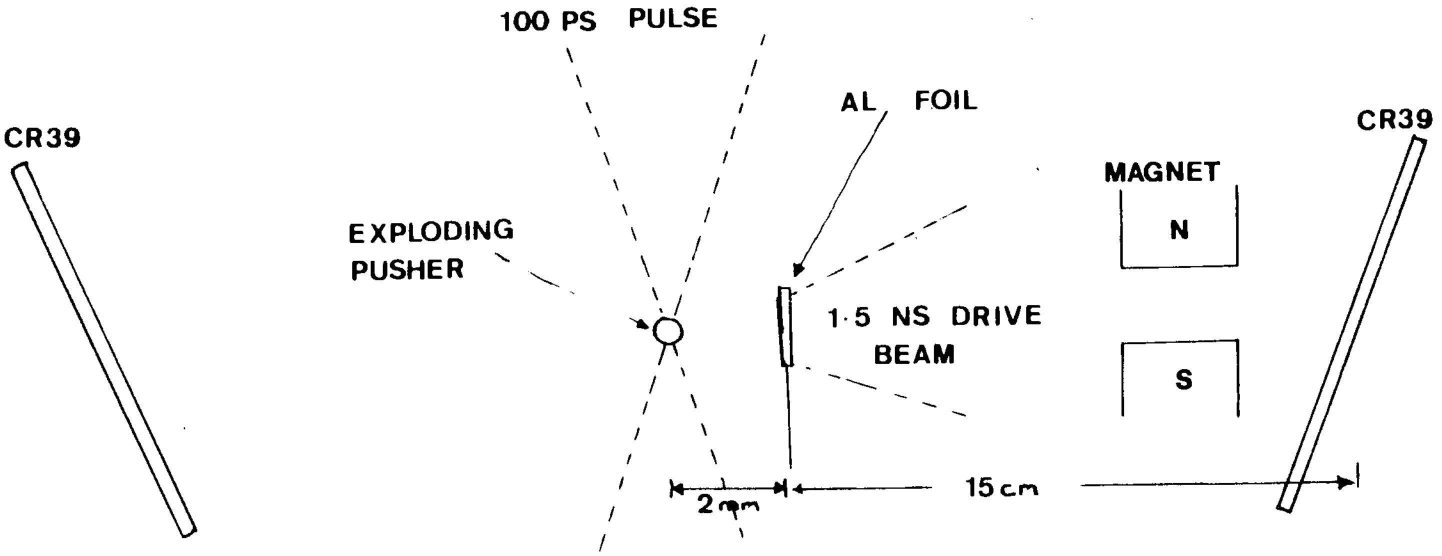

Fig(5.3) The experimental arrangement for the alpha particle backlighting of laser accelerated targets.

probed at different times on different shots.

The accelerated foil was a 3μm thick, 270 μm diameter aluminium foil either plane or corrugated to a depth of 0.5 μm with a period of 20 μm. It was accelerated with three beams of 1.06μm light, each at an angle of 56^0 to the normal, with 100 J in 1.5ns FWHM. The foil was typically placed 2mm from the exploding pusher, subtending a solid angle of 1.1×10^{-3} steradians to the source, thus for an alpha yield of 10^6 into 4π, 10^3 passed through the foil.

A 0.3 Tesla peak field magnet was placed 5cm from the CR39, a wide slit in front of the magnet restricted particles to travel through the region of uniform field. This magnet deflected the ablating plasma away from the region of the CR39 where the alphas were imaged, preventing ion damage to the plastic detector.

To first order the angle θ a charged particle travelling through a magnet of length d is deflected is

$$\theta = \mathrm{Tan}^{-1}(zeBd/mv) \tag{5.1}$$

For the ablating plasma $v = 5 \times 10^7$cm s^{-1}, and as d = 2.5 cm we find $\theta = 37^0$, i.e. the plasma is totally deflected away from the CR39. The alpha particles have a velocity of 10^9 cm s^{-1} and we find $\theta = 1.6^0$, and thus the alpha particles are only deflected 1.4 mm on the CR39.

There are several constraints on the distance between the alpha source and the foil. We want this distance to be as small as possible to maximise the number of alphas passing through the foil, and also to improve the resolution set by multiple coulomb scattering of the alphas, as will be described below.

However, the microballoon is irradiated sometime during the acceleration of the foil; thus we must ensure that the x-rays and plasma blow off from the foil do not knock off the microballoon before it is irradiated, i.e. we must not have the microballoon too close to the foil. A distance of 1.5 → 2.0 mm was chosen for safety; only a limited number of shots were available for this experiment and we did not wish to waste them by disturbing the microballoon inadvertently.

5.5 Temporal Resolution

Another parameter constraining this distance is temporal resolution. Simulations indicate that the alpha particles are produced in a pulse of ~20 ps. However, these particles have a Doppler spread in velocity and thus the pulse will spread out in time and the temporal resolution decrease as they move away from the exploding pusher. For a temperature of 1Kev in the pusher the spread in particle velocity about the mean of $1.3\times 10^{9}\mathrm{cms}^{-1}$ is $10^{8}\mathrm{cms}^{-1}$. We can express the temporal resolution, Δt, as a function of distance from the exploding pusher. If v is the average alpha particle velocity with a spread of $2\Delta v$ FWHM then, at a distance d from the pusher;

$$\Delta t = \frac{d}{v+\Delta v} - \frac{d}{v-\Delta v} \qquad (5.2)$$

assuming $\Delta v \ll v$

$$\Delta t = \frac{d}{v}\left(\frac{2\Delta v}{v}\right) \tag{5.3}$$

Which for 1Kev yields $\Delta t = 12$ ps mm^{-1}. Thus when the foil is 2mm away the temporal resolution due to Doppler broadening becomes comparable with that due to the finite fusion burn time.

5.6 Spatial Resolution

There are two factors that determine the lateral (i.e. perpendicular to the measured ρr) spatial resolution. First, the diameter of the core from which the alphas are emitted; this is about 20 μm, as has been determined from x-ray pinhole camera pictures. Secondly the alphas will undergo multiple coulomb scattering as they pass through the foil. The average root mean square angle, $\langle(\Delta\theta)^2\rangle^{1/2}$, through which a particle is scattered is given by (5.8):

$$\langle(\Delta\theta)^2\rangle = \frac{8\pi N z^2 Z^2 e^4 L}{(4\pi\varepsilon_0)^2 v^2 p^2} \log\left(\frac{b_{max}}{b_{min}}\right) \tag{5.4}$$

where b is the impact parameter, N the number density of nuclei, ze the charge on the alpha particle, Ze the charge on the scattering nucleus, L the thickness of scattering material, v the alpha particle velocity and p its momentum.

The effective charge of the scattering nucleus is a function of b, at b_{max} the charge should be completely screened. In a crude way this can be approximated by choosing:

$$b_{max} = \frac{a_0}{Z^{1/3}} \tag{5.5}$$

where a_0 is the Bohr radius. This value may be justified by the Thomas-Fermi statistical model of the atom. On the other hand we choose b_{min} to be small compared with 1 rad for a single collision giving:

$$b_{min} = \frac{zZe^2}{4\pi\varepsilon_0 vp} \qquad (5.6)$$

The result is not very sensitive to b_{max} and b_{min} which only appear logarithmically in equation (5.4). For this experiment where the alphas traverse 3μm of Al the scattering angle is 30 mrad.

Now to see how this effects the lateral spatial resolution consider Fig(5.4). Two particles travelling through the same point on the foil may have paths at an angle $\Delta\theta$ to each other; they will impinge on the CR39 a distance $\Delta\theta D$ apart. The magnification, M, is given by:

$$M = \frac{D+d}{d} \qquad (5.7)$$

Therefore the resolution on the foil is:

$$\frac{\Delta\theta D}{M} = \frac{\Delta\theta Dd}{D+d} \qquad (5.8)$$

and as $d \ll D$ the resolution is $\Delta\theta d$. Thus the closer we can get the foil to the exploding pusher, the better the spatial resolution. With d=2mm the resolution is ~ 60 μm. However, we note that $\langle(\Delta\theta)^2\rangle$ scales as Z^2NL, and N as ρ/Z, thus $\langle(\Delta\theta)^2\rangle^{1/2}$ is proportional to $Z^{1/2}$ for a given ρL. Therefore to optimise the spatial resolution we should use a target with as low a Z as possible - plastic targets would give a resolution of ~ 40 μm when 2 mm away from the

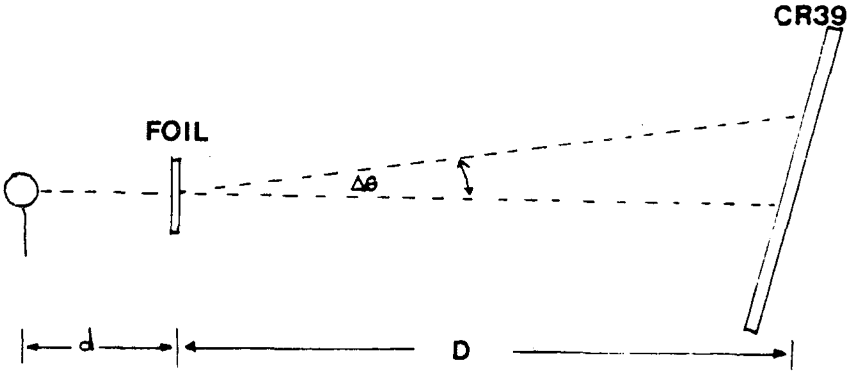

Fig(5.4) Resolution due to Multiple coulomb scattering.

microballoon. However, the laser time for this experiment was allocated at short notice and the targets used were those that could be manufactured quickest, i.e corrugated Al by depositing Al onto gratings through circular masks and floating off the resultant discs. These targets were sufficient to achieve the main aim of this feasability study; i.e. proof of principle rather than extensive quantitative results. In future experiments it may be possible to achieve resolution of up to 35μm by using plastic targets and putting the targets as close as possible to the exploding pusher.

It should be stressed that, although the resolution is limited, variations in ρr on a shorter scale length will still change the alpha particle residual range spectrum, though the scale length is undetermined. In fact the shortest length on which a meaningful range spectrum can be produced will be $x\Delta\theta$, where x is the width of the target, i.e. less than 0.1 μm.

5.7 Range as a Function of Temperature and Density

The stopping power of matter to alpha particles is a function of the density and temperature of the material as well as the atomic number. The stopping power of Aluminium is shown in Fig(5.5) for several different densities and temperatures as a function of alpha particle energy, from calculations performed by Rose(5.9). Thus although the residual range in CR39 tells us the energy of the particle after passing through the foil, we must make certain assumptions about the density and temperature profile of the driven foil to calculate the variations in the foil thickness.

The first thing to note is that the low density high temperature ablating plasma has a small contribution to the energy loss.

From Fig (5.5)

$$\frac{dE}{dx} \approx 2 \times 10^3 \text{ Mev cm}^{-1}$$

i.e. about 1/7 of that of cold material on average. From independent mass ablation measurements(3.25) 1.5×10^5gm $\text{cm}^{-2}\text{s}^{-1}$ will be ablated at 10^{14}Wcm^{-2} for 1.05μm light (i.e. the conditions for the feasibility study described in this chapter). Thus 1.5×10^{-4} gm cm^{-2} will be ablated in 1ns;

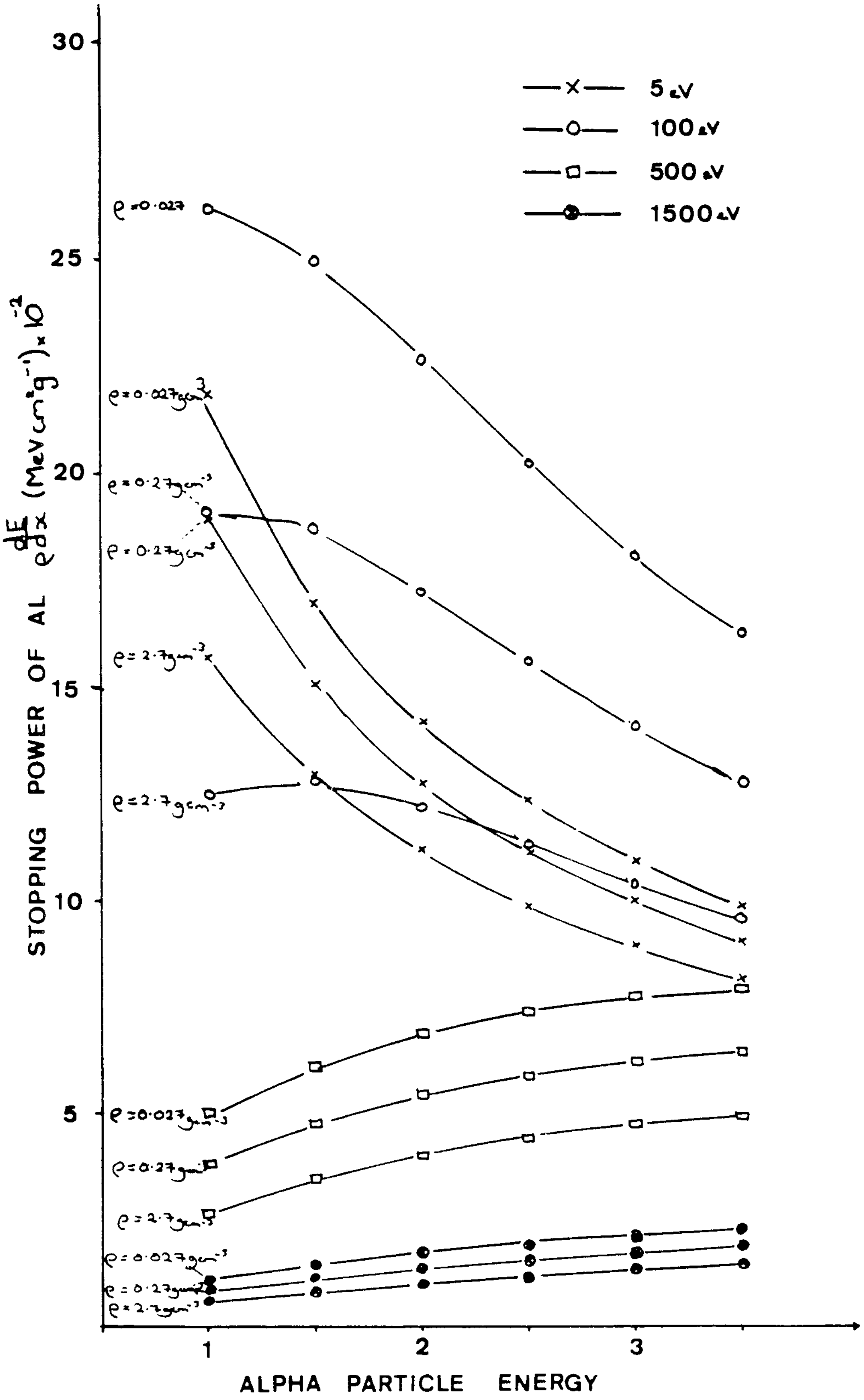

Fig(5.5) Stopping powers of Al as a function of density and temperature from the calculations of Rose.

the foils have an areal mass density of 8 × 10^{-4} gm cm^{-2}, so 19% of the initial mass is ablated after 1ns. Therefore the energy lost by the alpha particle in the corona when the foil has been accelerated for 1ns will be 19/7 = 2.7% of the initial thickness of the foil. This is equivalent to 0.2 gm $cm^{-3}\mu m$ - roughly equal to the straggling of the alpha particle in the CR39 detector. Thus the energy lost in the ablating plasma is negligible. More importantly the variations in the lost energy in the corona will be much smaller than this.

The next consideration is the energy loss of the particle passing through the main part of the foil. We wish to know the error caused by ignoring the realistic density and temperature profile on our estimation of the effective ρr of the foil from the residual range spectrum.

We expect the error to come from two sources. First in the region of a strong shock the stopping power will be lowered, the exit energy of the alpha from the foil will increase, and we will underestimate the ρr of the foil if we assume it is cold and of solid density. Secondly there will be a thin region at the ablation surface which is both relatively hot and dense, i.e. have an increased stopping power, and this will tend to make us overestimate the ρr of the foil.

To estimate the magnitude of the effects mentioned above the calculations of Rose have been used in conjunction with "Pollux" simulations. The energy lost by a 3.5 Mev alpha particle passing through the density and temperature profiles predicted by the code has been estimated in two ways.

i) By using the density and temperature dependent stopping powers.

ii) By using the stopping power for cold solid material at all points.

The values of the exit energies from the foil can be converted into estimates of the equivalent thickness of cold solid Al traversed by the alpha particles using Figs(5.6) and (5.7). The difference in these two thicknesses tells us the error in assuming that experimentally obtained residual ranges are derived from particles passing through a cold foil of solid density.

This calculation has been performed for two code runs. First for a 3 μm thick Al foil corrugated with an amplitude of 0.5 μm and irradiated with 10^{14}W cm^{-2} of 1.05μm light - i.e. the conditions of the feasibility study. Secondly for the code run mentioned in section (4.6), i.e. 2×10^{13} W cm^{-2} of 0.53 μm light on 10 μm of 1.3 gm cm^{-3} plastic mass modulated to a depth of 2 μm (Rose has also performed calculations for the stopping power of such plastic). This second run was chosen because it is likely that plastic targets will be used in future experiments for the reasons given in section (5.6).

The results of these calculations are shown for the two runs in Figs(5.8) and (5.9). The error in the

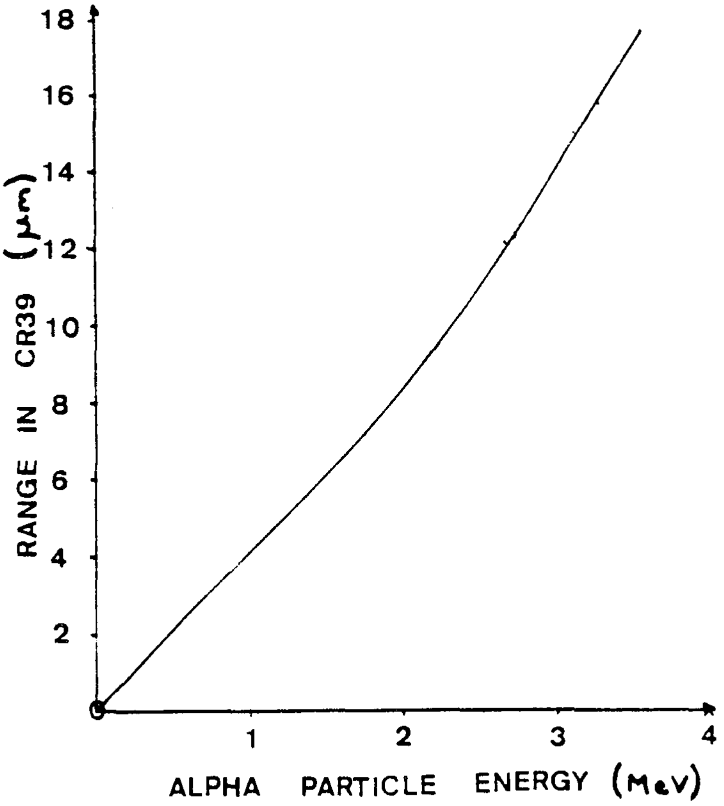

Fig(5.6) The energy of the alpha particle as a function of range in CR39.

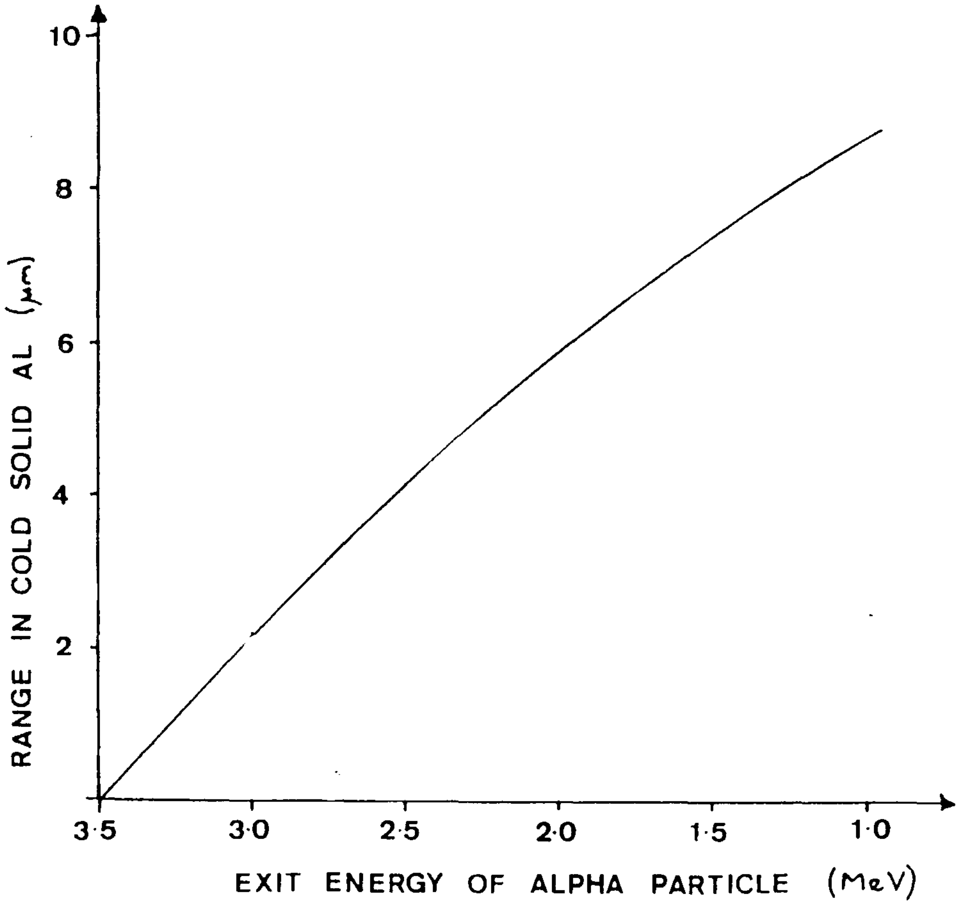

Fig(5.7) Exit energy of the alpha particle from the foil as a function of thickness of the foil, assuming the foil is cold and of solid density.

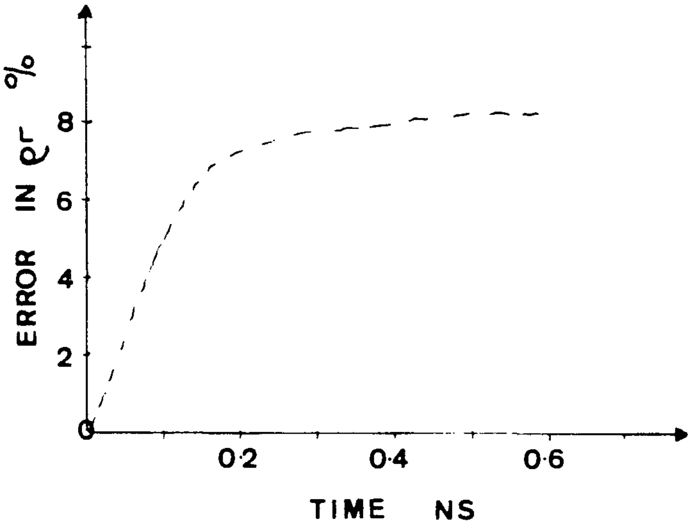

Fig(5.8) Error in ρr for the Al code run.

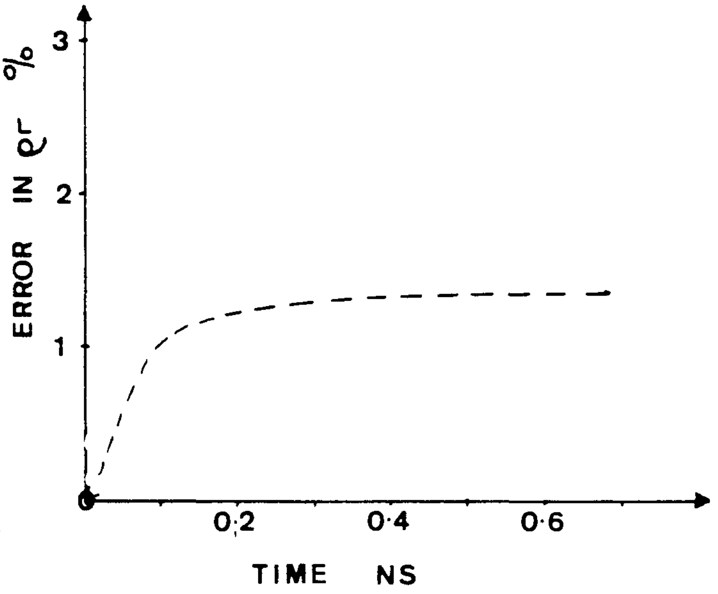

Fig(5.9) Error in ρr for the CH code run.

measurement of the total ρr rises quickly in both cases and then levels off as a steady state in the density and temperature profiles is achieved. The error is such as to make us overestimate the ρr of the foil(i.e. E_{exit} is less for realistic profiles). This is because the increased stopping power due to heating at the ablation surface dominates over the effect of the reduced stopping power in the shock.

The error in the ρr for the Al run is five times that of the CH case. This is not surprising. The higher irradiance in the Al run gives rise to a larger region at the ablation surface which is both relatively hot (100 ev) and dense enough to make a significant change to the alpha particle energy. For the CH case the error is 1.5%, of order 0.2 gm $cm^{-3}\mu m$, the straggling limit. For the Al case it is 1.0 gm $cm^{-3}\mu m$ and is non negligible if we wish to know the ρr of the foil accurately.

However in studies related to ICF the more interesting parameter is the variation in ρr across the foil, rather than the absolute magnitude; this is the parameter we wish to measure for R-T studies. Both of the computational runs mentioned above were for R-T unstable targets. The energy lost by alpha particles was calculated at both peaks and troughs of the ρr at various times during the growth of the instability, and an error in these variations in ρr estimated in a similar way to that for the absolute magnitude.

The results are shown in Fig(5.10), where the error in $\Delta(\rho r)$ is plotted as a function of $\Delta(\rho r)$ for both of the simulations. Below a $\Delta(\rho r)$ of 0.3 gm $cm^{-3}\mu m$ numerical errors due to the finite mesh size in the code start to dominate and thus the errors are only plotted above this value.

Again, as expected, the errors are greater in the higher irradiance Al run. They decrease as $\Delta(\rho r)$ increases; this is because the value of the error in terms of gm $cm^{-3}\mu m$ varies little once steady state is achieved at the ablation surface, and therefore when plotted against $\Delta(\rho r)$ the percentage error falls off as $1/\Delta(\rho r)$ to first order.

From Fig(5.10) we see that the realistic density and temperature profiles have little effect on the measured variations in ρr for the plastic foils driven at 2×10^{13} W cm^{-2}, and are 4 % at 0.5 gm $cm^{-3}\mu m$. However for the high intensity run errors as high as 40 % can occur for small variations in ρr.

5.8 Anisotropy in the parent distribution

The alpha particles will lose some energy in passing through the stagnated material of the exploding pusher. If this energy loss is totally isotropic we can deconvolve this parent distribution from that of the alphas passing through the foil. Typically the alphas from the exploding pushers have a range in CR39 of 16.9 μm, i.e. they lose about 0.7 μm of residual range traversing the stagnated shell.

In this feasibility study the parent distribution was

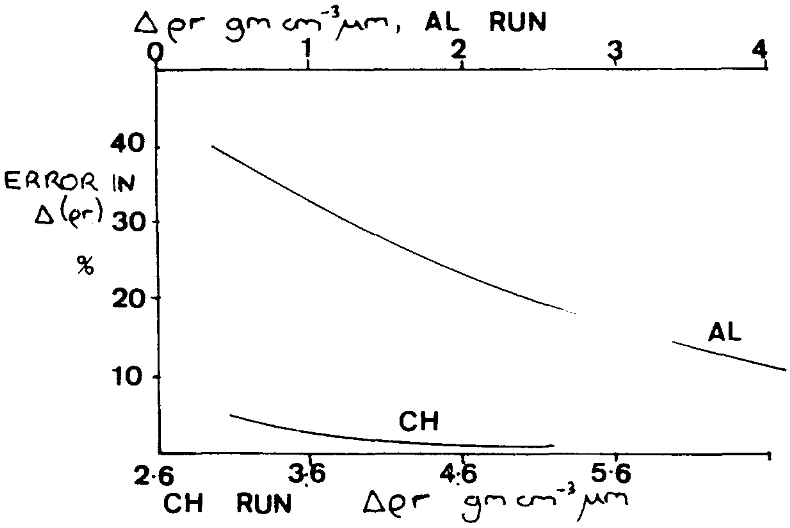

Fig(5.10) Error in the measured ρr caused by ignoring the realistic density and temperature profiles for the two code runs.

recorded on CR39 placed on the opposite side of the pusher to the target, whereas in future experiments it may be possible to record both the foil and the parent spectra on the same piece of detector by using the arrangement shown in Fig(5.11), rendering anisotopy effects negligible.

However anisotropy in the stagnated mass surrounding the fusion core in the exploding pusher is more likely just to shift the spectrum of the parent, the gaussian width being determined by the temperature in the core; thus the errors induced will be in the absolute magnitude of the ρr of the foil, rather than variations in ρr.

5.9 Experimental results

The first residual range spectra from alpha particle backlit laser accelerated targets are shown in Figs(5.12) and (5.13). These are the two shots in which sufficient alpha particles were produced to enable a meaningful spectrum to be obtained.

Fig(5.12) is the spectrum from a 3μm Al foil corrugated at 20μm wavelength to a depth of 0.5μm, accelerated with an incident irradiance of 5×10^{14} Wcm^{-2} of 1.05μm light and probed with the alpha particles 1.5ns after the start of the drive pulse.

Fig(5.13) is the spectrum from a plane 3μm Al foil accelerated with an incident irradiance of 5×10^{14} Wcm^{-2} of 1.05μm light and probed at 900 ps after the onset of the drive pulse.

In these spectra alpha particles passing within 50μm

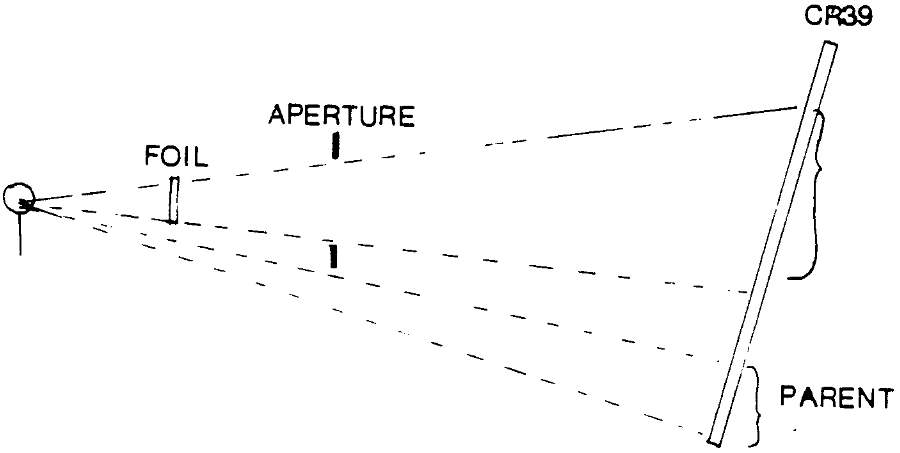

Fig(5.11) Arrangement for measuring the parent distribution on the same piece of CR39 as the foil distribution.

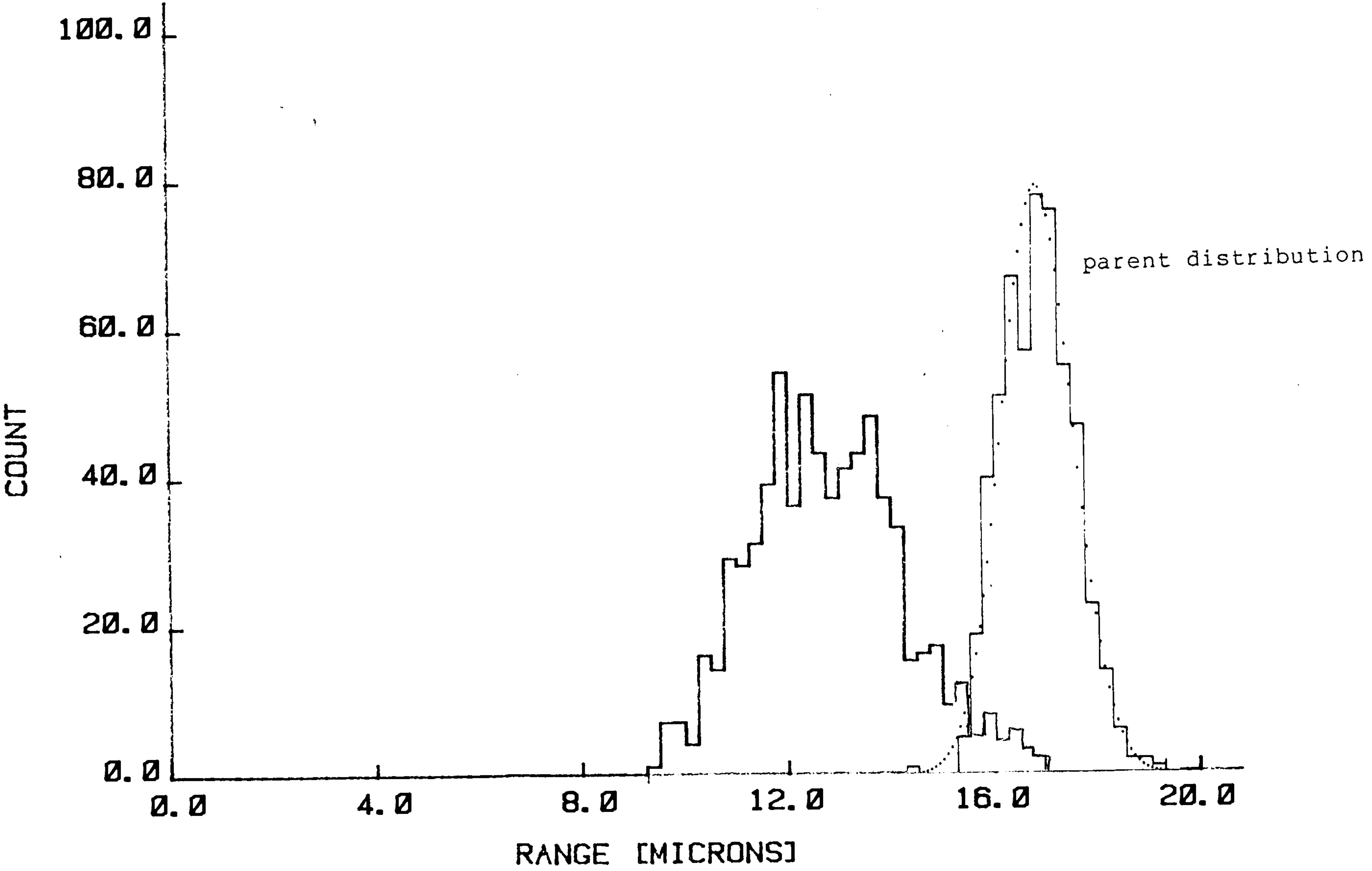

Fig(5.12) Alpha particle range spectrum for 3μm corrugated Al foil.

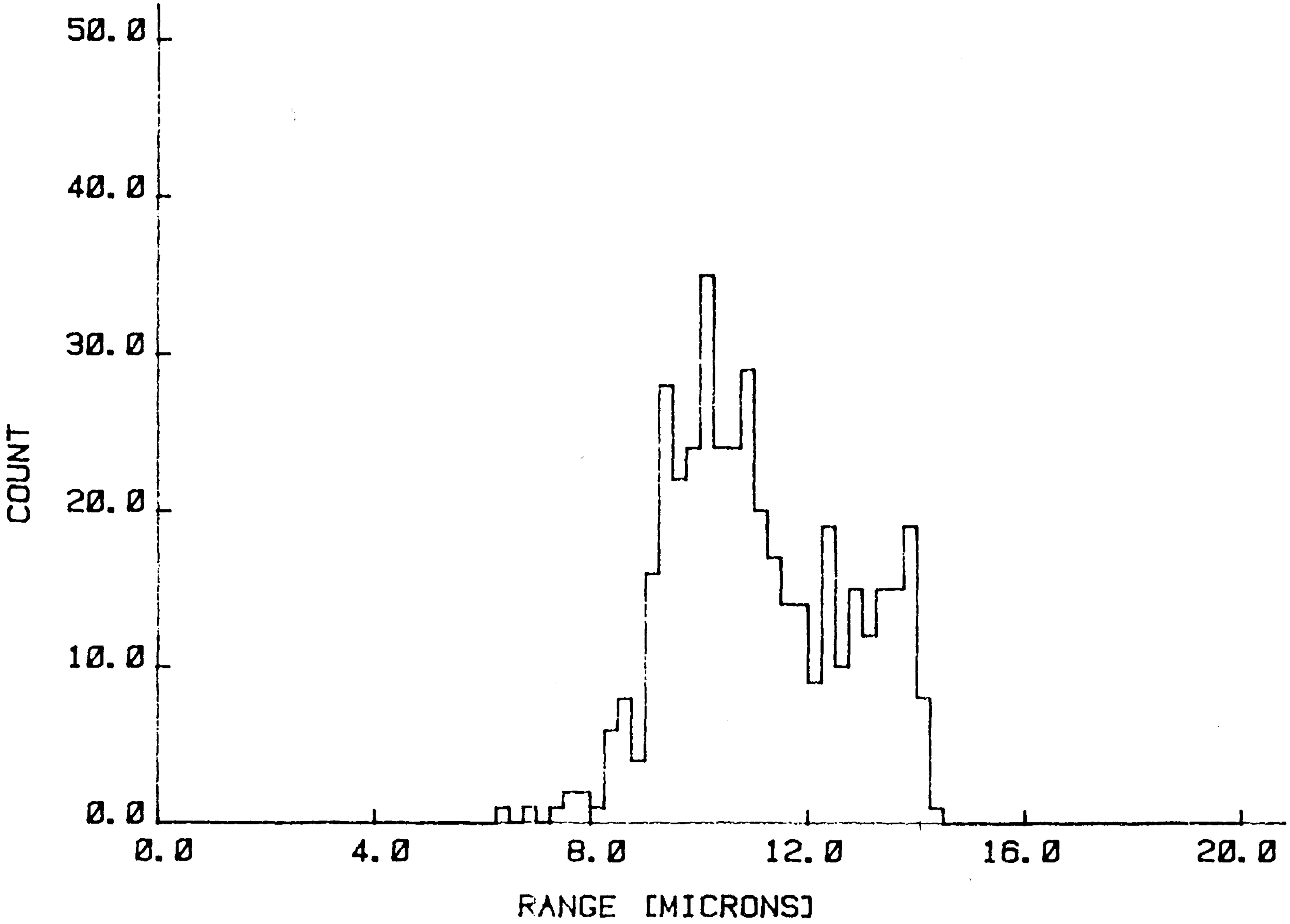

Fig(5.13) Alpha particle range spectrum for 3μm plane Al foil.

of the edge of the foil have been ignored to prevent edge effects distorting the distribution.

The first thing to note is that both distributions are broader than the parent, indicating that there is a variation in ρr across the target. We shall now discuss each shot in turn before making comparisons between the two.

5.10 The corrugated target spectrum

Here the alpha particle residual range spectrum is spread over the range 9.2 to 17μm in CR39. This is equivalent to a spread in thickness of solid Al of 5.2 to 0.0μm; i.e. some region of the target has started to break up, whereas other regions of the target have greater thicknesses than at the onset of acceleration. This indicates that there has been mass redistribution, indicative of the R-T instability. Such an effect would not be caused by preferential ablation at hot spots in the beam, as they could not give rise to regions of greater than original thickness. However, as there are yet no other range spectra obtained at different times during acceleration we can make no estimate of the rate of the mass redistribution. No periodic variations in the alpha range could be seen across the foil due to the 60μm resolution set by multiple coulomb scattering.

5.11 The plane target spectrum

Perhaps the more interesting of the two results is that obtained from the plane target, where again we see evidence of mass redistribution. Here the spread of ranges corresponds to a spread in thicknesses of cold solid Al of 2 to 6μm. Thus all the target is still intact even though there is evidence of areas of the foil containing large spikes.

The mass redistribution in this case has grown totally from noise and thus we have no way of telling the spatial scalelength of the variations in ρr.

This noise could have arisen from defects in the final lenses as mentioned in Chapter Three, or from noise in the beam, or small irregularities on the surface of the target.

5.12 Comparison of the two results

From the range spectra we can calculate that the two foils have different mean thicknesses; the mean thickness of the corrugated foil is 2.95μm, and of the plane foil 3.35μm. The difference of mean thickness is consistent with the expected difference in ablated mass due to the different probe times for these two shots. However both foils have a greater mean thickness than we would expect. We know from section (5.11) that we are liable to overestimate the thickness by 10%, i.e. 0.3μm, due to the hot region at the ablation surface, but these results are about 35% greater than we would expect once the ablated mass is taken into account. There are two possible explanations for this. First there could have been an error in the measurement of the initial target thickness, and more care must be taken in future. Secondly we note that this is consistent with x-ray preheat decompressing the target, and if so further experiments are necessary to ascertain whether similar problems occur for low Z at lower intensities.

From the residual range curves, if we assume that the variations are periodic and symmetric, then assuming that the number of alpha particles traversing a given thickness is proportional to the area at that thickness normal to the plane of the target, we can plot thickness against wavelength as shown in Fig(5.14). We see that the plane target has a smoother bubble and spike, indicating that the R-T instabilty is not so advanced as in the corrugated case. However, the variations in ρr are unlikely to occur with only one periodicity, and interpretation of graphs such as (5.14) must await a larger collection of data at different probe times and with better spatial resolution.

5.13 Conclusion

This chapter has described the concept of alpha particle backlighting and has gone on to explain some of the advantages and limitations of the technique, along with the effects constraining experimental parameters. The advantages are shown to be good temporal resolution, good resolution in ρr, and the ability to detect variations in ρr on very small scalelengths, though the scalelength is undetermined.

Combining computed stopping powers with 2-D simulations has shown that the temperature and density profiles of the accelerated foil have negligible effect on the measurements of the variation in ρr as long as the drive intensity is kept low enough (2×10^{13} Wcm^{-2}).

The first ever range spectra from alpha particle backlit laser accelerated targets have been presented, showing evidence of mass redistribution, and hence the R-T instability, in both corrugated and plane targets.

Thus the principle of the technique has been proved, and it promises to act as a valuable complement to x-ray backlighting in the study of laser accelerated foils.

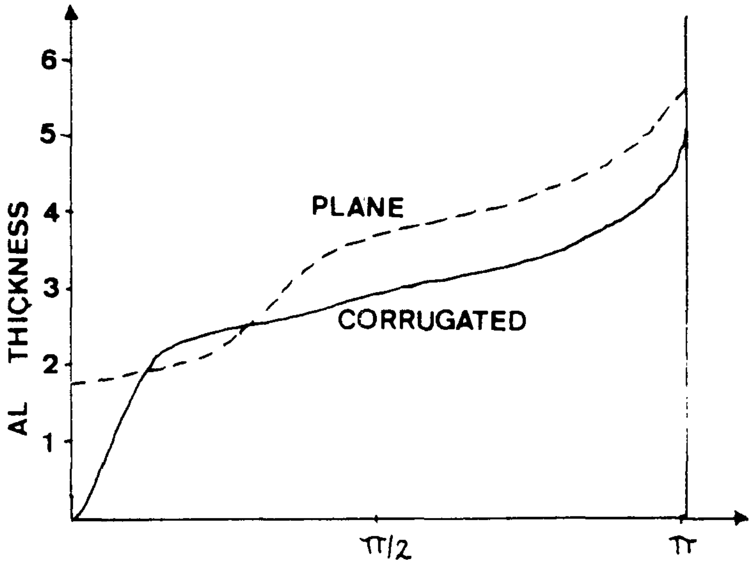

Fig(5.14) Variation in target thickness for the two foils.

CHAPTER SIX

POINT PROJECTION RADIOGRAPHY OF FOILS

Abstract

Laser accelerated foils have been backlit by point projection radiography. The spatial resolution has been determined. The effects of self emission from the foil are discussed.

6.1 Introduction

To date the majority of experiments employing X-Ray backlighting have used extended sources, the resolution being determined by pinhole imaging. However, X-Ray backlighting with spatial resolution can also be obtained by using a point source (6.1) and recording the shadow of the object as shown in Fig(6.1). The resolution is then determined by the size of the point emitter.

If the image is diffracted off a crystal onto the image plane then the recorded image will be the shadow of the object in the spectrum of the backlight - thus at each point on the object the backlighting wavelength is known and the corresponding ρr in the target can be measured accurately.

The advantages of such a technique are that the backlight is uniform and quasi monochromatic - i.e. at each point on the target the backlighting wavelength is known.

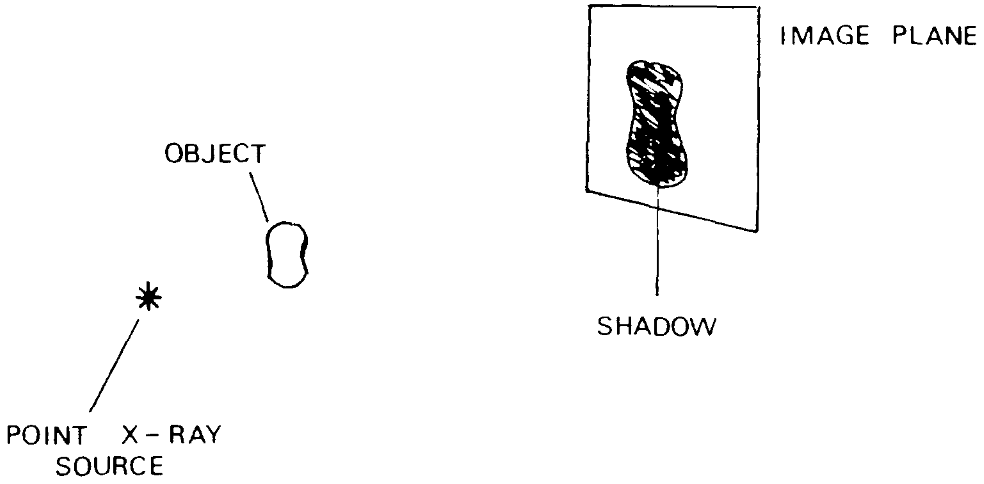

Fig(6.1) The concept of point projection backlighting.

6.2 Previous Work

Miyanaga et al (6.2) have used point projection radiography (without spectral resolution) to image an imploding microballoon using 1.2 Kev X-Rays from the tip of a Cu wire. They have also spectrally resolved the image of a micromesh with 63 μm grid seperation.

Other workers (6.2)(6.3) have used the point projection technique to probe steep density gradients near to the ablation surface by observing the refraction of the X -Rays.

A group from the Queen's University Belfast has also recently backlit microballoons with a point source of Tungsten x-rays.(6.4)

6.3 Comparison of Extended and Point Source Backlights

The use of a point source has several distinct advantages over an extended source (6.1). First, the laser energy required to produce the backlight is reduced because of the small focal spot; secondly large magnifications (100) can be obtained without sacrificing the light collection efficiency, as the source and object can be brought close together without affecting the object; lastly the backlight is uniform and does not contain hot spots of emission found in extended sources.

However, there is a disadvantage to the technique: we find that X-Ray refraction effects are far more important for a point source. Detailed mathematical explanations of this effect are given in references (6.2)(6.3). The following simpler first order explanation has been given by Key (6.5).

Consider the arrangement in Fig(6.2). We can consider the point P to be either a point source or as a pinhole. For the point source case (uppermost on the diagram) we consider one point Q in the image plane A. Rays from P could have reached it along path 1, where the density gradient is small; or they could have travelled along path 2, through a steep density gradient near the ablation surface, being refracted through an angle θ. From the diagram, as in practice $R \gg D$,

$$\theta \sim \phi \tag{6.1}$$

therefore the resolution on target, Δy_p, is of order

$$\Delta y_p \sim D\theta \tag{6.2}$$

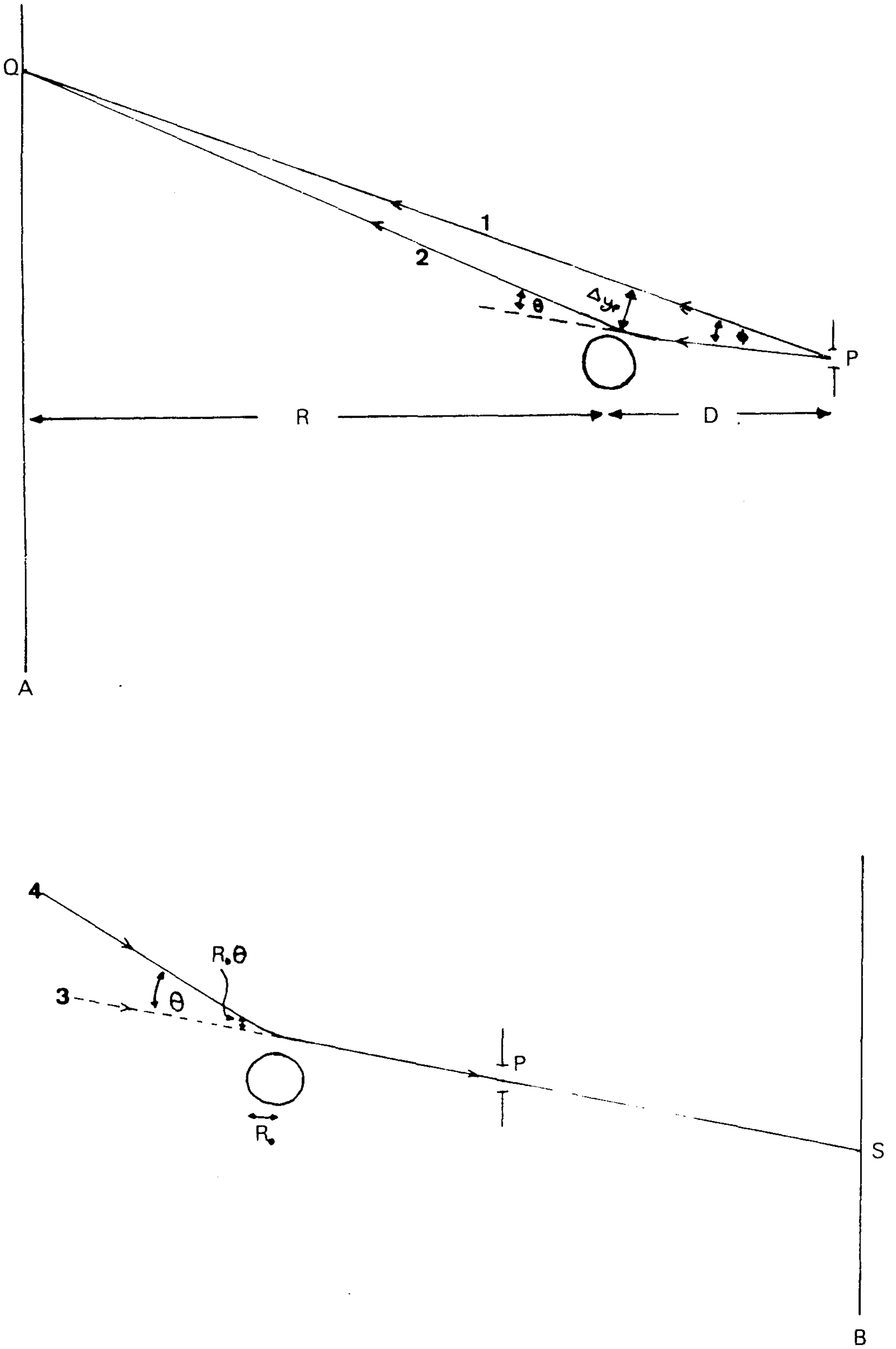

Fig(6.2) First order estimation of refraction effects for point sources (upper diagram) and extended sources (lower diagram).

Now consider the extended source case (lower on the diagram). Our image plane is now the plane B. For one point S on the image plane the rays could have travelled the straight course 3 or have been refracted through the density gradient, 4. In this case we see that the resolution on the target, Δy_e, is

$$\Delta y_e \sim R_0\theta \qquad (6.3)$$

where R_0 is the radius of the target. Therefore

$$\frac{\Delta y_e}{\Delta y_p} = \frac{R_0}{D} \qquad (6.4)$$

In practice $R_0 \sim 100$ μm and $D \sim 2$ mm and thus the refraction effects are of order 20 times more significant for point sources.

6.4 Experiments

Two seperate point projection experiments will be discribed in this chapter; the first carried out at the RAL's CLF, and the second was performed on the 'Phoenix' Laser System at The Lawrence Livermore National Laboratory, California, USA.

The two experiments have essentially the same set up and the Rutherford experiment is shown in Fig(6.3). The differences between the experiments are the laser beam parameters, targets and detector (photocathode or film), and these will be described in the appropriate sections.

6.5 The RAL experiment

This aim of this experiment was to observe laser accelerated foils by point projection radiography; measure

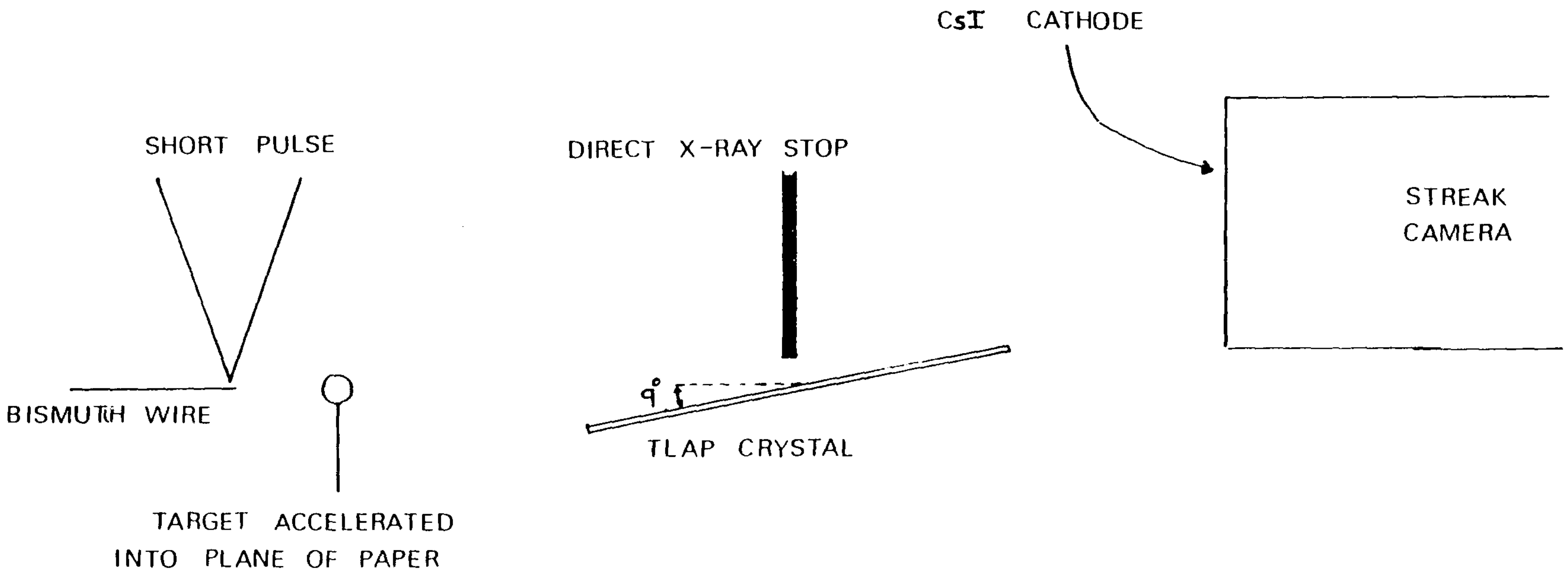

Fig(6.3) Experimental set up for the Rutherford point projection experiment.

the spatial resolution and determine how much of a problem self emission from the target posed.

For good spatial resolution we need to use a high energy backlight to minimise refraction effects. The maximum angle of refraction has been measured to be between 3 (6.3) and 8 (6.2) mrad for 1.2 Kev X-Rays passing through the steepest density gradient in a plasma produced by focusing 5×10^{14} Wcm^{-2} onto a plastic target. In this experiments D ~ 1 → 2 mm, giving a resolution due to refraction effects of up to 16 μm for 1.2 Kev radiation. Now the refraction angle, θ, is related to the gradient of the refractive index:

$$\theta \ \alpha \ \frac{dn}{dr} \ \alpha \ \frac{1}{E^2_{bl}} \qquad (6.5)$$

where E_{bl} is the energy of the backlight. So for the 2.8 Kev radiation used in these experiments the angle of refraction is less than in those referenced above by a factor

$$\frac{1.2^2}{2.8^2} = 0.18 \qquad (6.6)$$

i.e. the upper limit on the resolution due to refraction is 3 μm.

6.6 Experimental set up

The point source of x-rays was produced by focusing 30 J of μm light onto the tip of a 10 μm diameter Bismuth wire. The focal spot size was 30 μm and the pulse length 200 ps. The x-rays produced were spectrally dispersed by a TLAP crystal onto the CsI photocathode of a streak camera in focus mode. The crystal was set halfway between the point source and the cathode (5 cm from both) at an angle of 9^0 so that the M band of Bismuth (4.4Å) was recorded with a dispersion of 4 Å cm^{-1}. A lead plate was placed 2 mm above the surface of the crystal to block the path of direct X-Rays.

The targets were positioned on a line from the point source to the crystal and were accelerated perpendicular to that line and parallel to the plane of the crystal. The drive beam was a 5ns pulse of 50 J of 1.05μm light.

6.7 Resolution

To measure the resolution of the point source a mesh of 10 μm wires and 15 μm spaces was placed between the point source and the detector at the object position. The result is shown in Fig(6.4) along with the densitometer tracing. From this we can see that the resolution is certainly better than 10 μm. However, from the densitometer tracing we see that light does reach the part of the shadow corresponding to the centre of the wire; i.e. part of the source must extend further out than a radius of 5 μm.

Knowing the film response (6.6) we can convert the density plot to relative intensity above background Now the opaque wire can be represented as an inverted top hat function in transmission. If we deconvolve the observed intensity distribution with the transmission function of the wire we obtain the relative intensity of the point source as a function of distance, as shown in Fig(6.5). We can

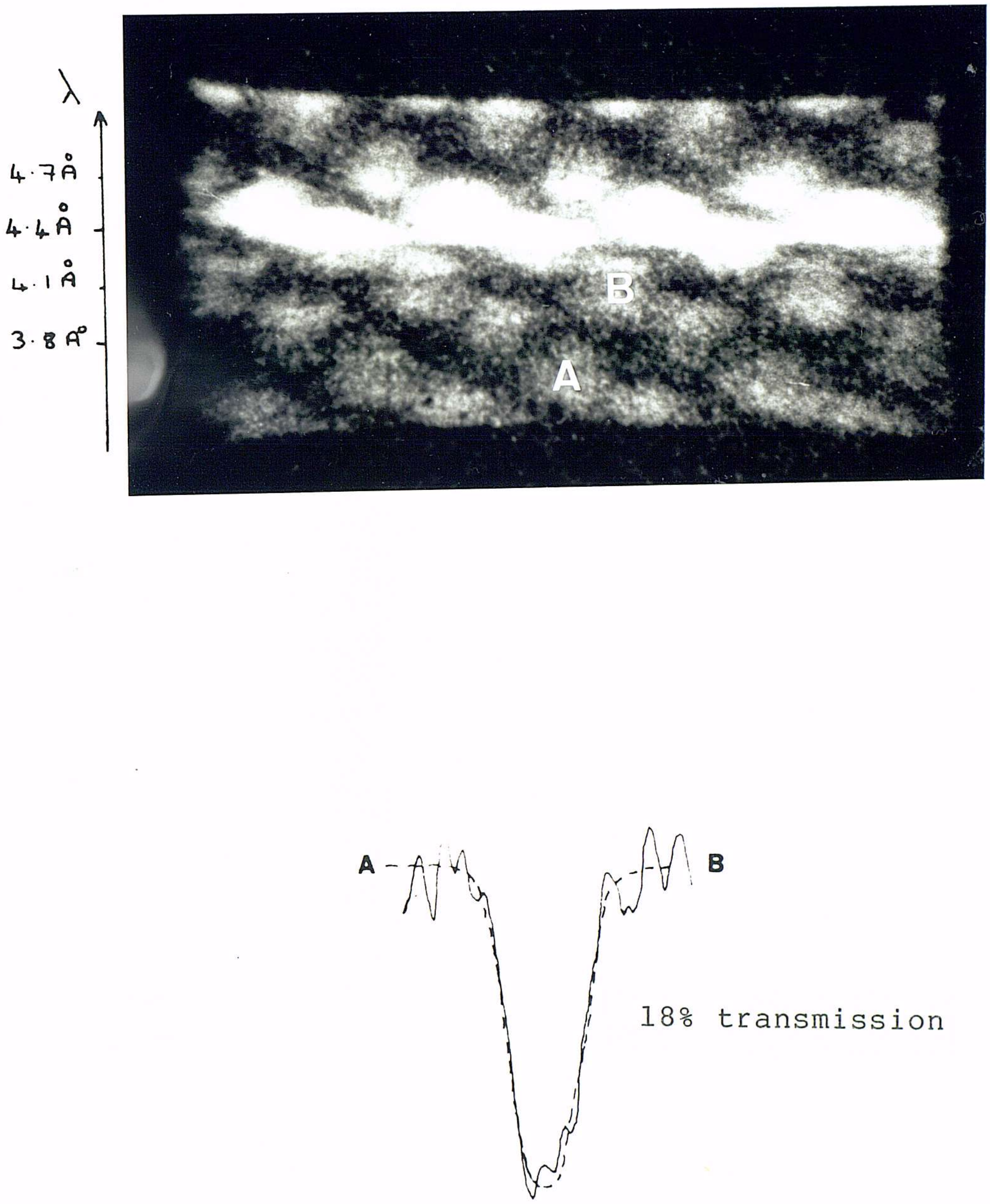

Fig(6.4) Shadow of the resolution grid in the Bi spectrum.

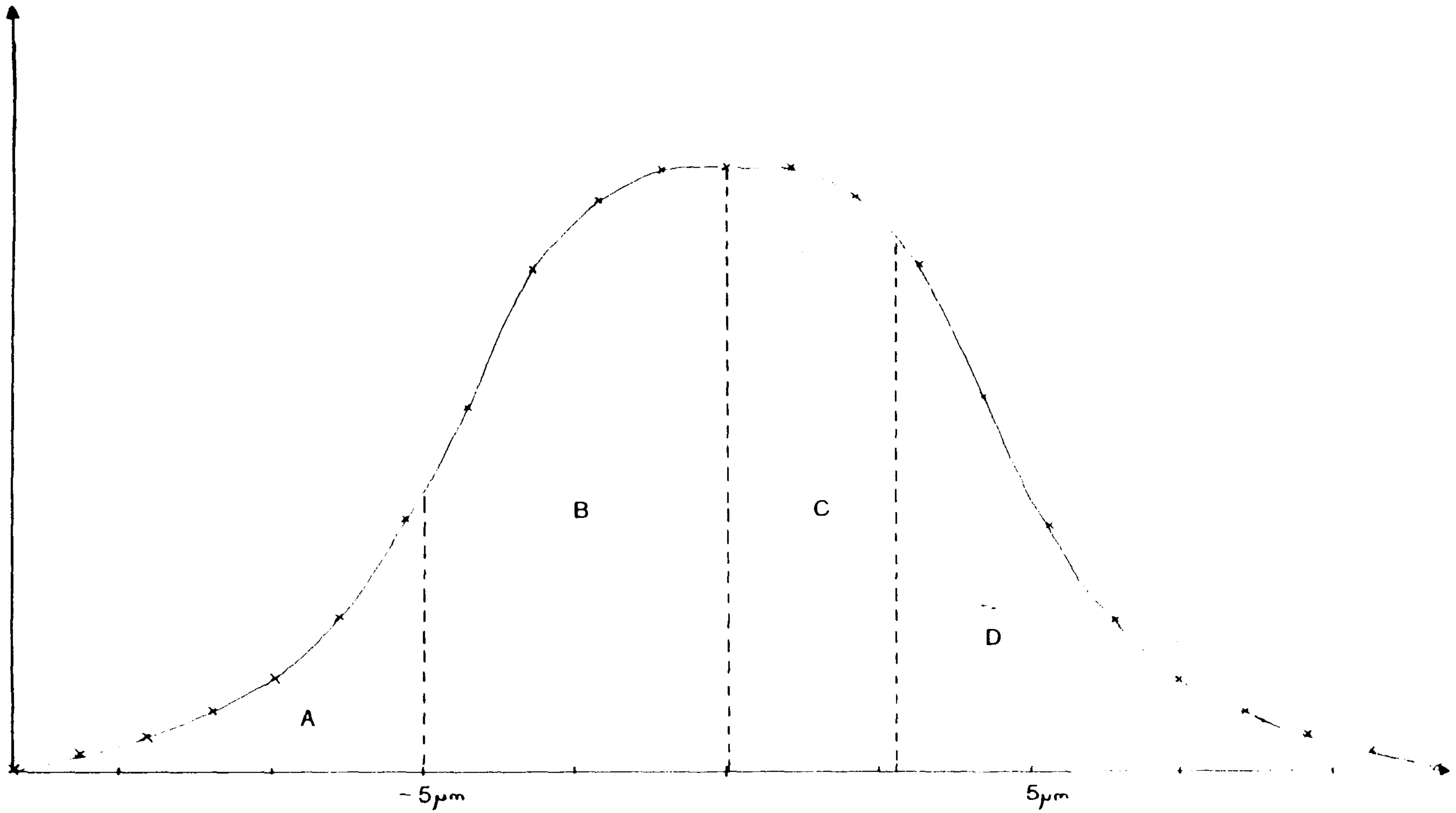

Fig(6.5) Intensity of the point source as a function of distance.

quickly check the accuracy of the deconvolution by calculating the relative intensity at the centre of the shadow. From Fig(6.5) this should simply be the ratio of the areas

$$\frac{A}{A + B} = 0.19 \qquad (6.7)$$

compared to the 0.18 observed.

Also, using Fig(6.5) we can make a formal definition of the resolution as the width of an opaque wire such that the relative intensity at the centre of the shadow is 0.5 that far from the shadow. This again can be simply measured from Fig(6.5), it occurs when the two areas C and D are equal. With this definition we find the resolution to be 5 μm. A similar calculation in the centre of the Bi m band (4.4Å) yields a resolution of 7μm.

The magnification in the RAL experiment varied between 60 and 100. Lower magnifications could not be obtained due to technical problems with the motor driving the backlighting lens; this also prevented an accurate knowledge of the magnification on a shot to shot basis.

6.8 Results

First an unirradiated plastic $(CH)_n$ foil was imaged side on as shown in Fig(6.6). The transmission of the foil to the 4.4Å x-rays is 40%, compared to the 25% calculated from the mass attenuation coefficient of the plastic; this is in reasonable agreement with the data found from the resolution results, i.e. some of the source extends beyond

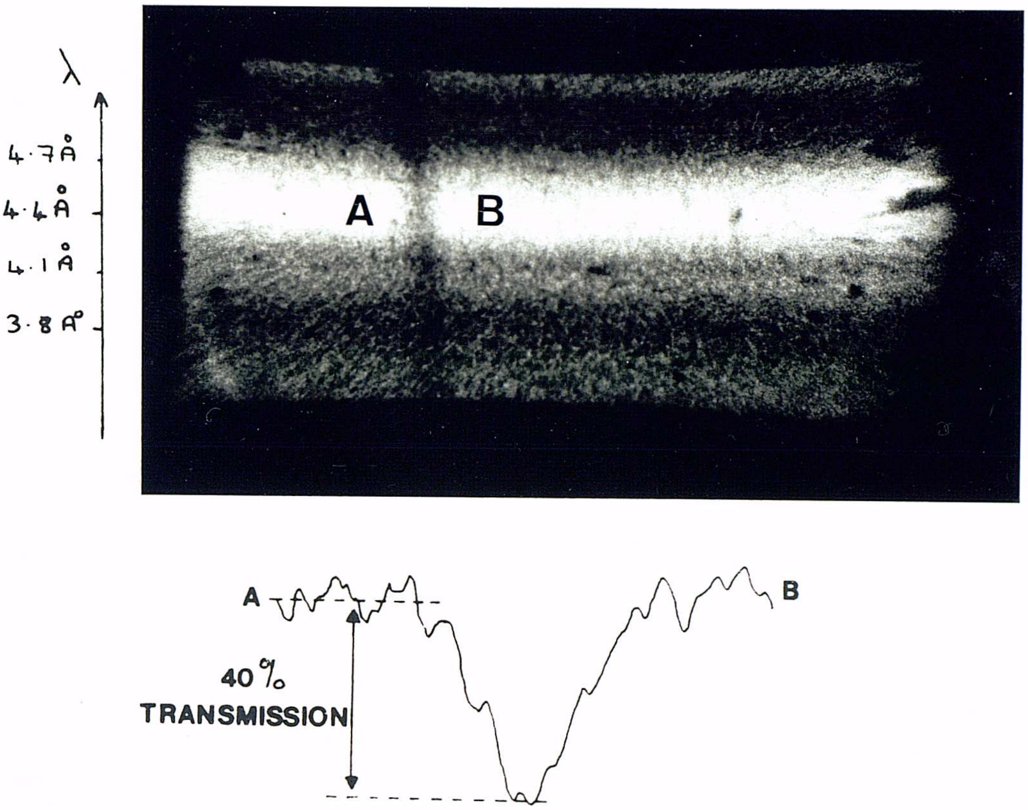

Fig(6.6) Shadowgraph of an unirradiated 10μm thick plastic foil.

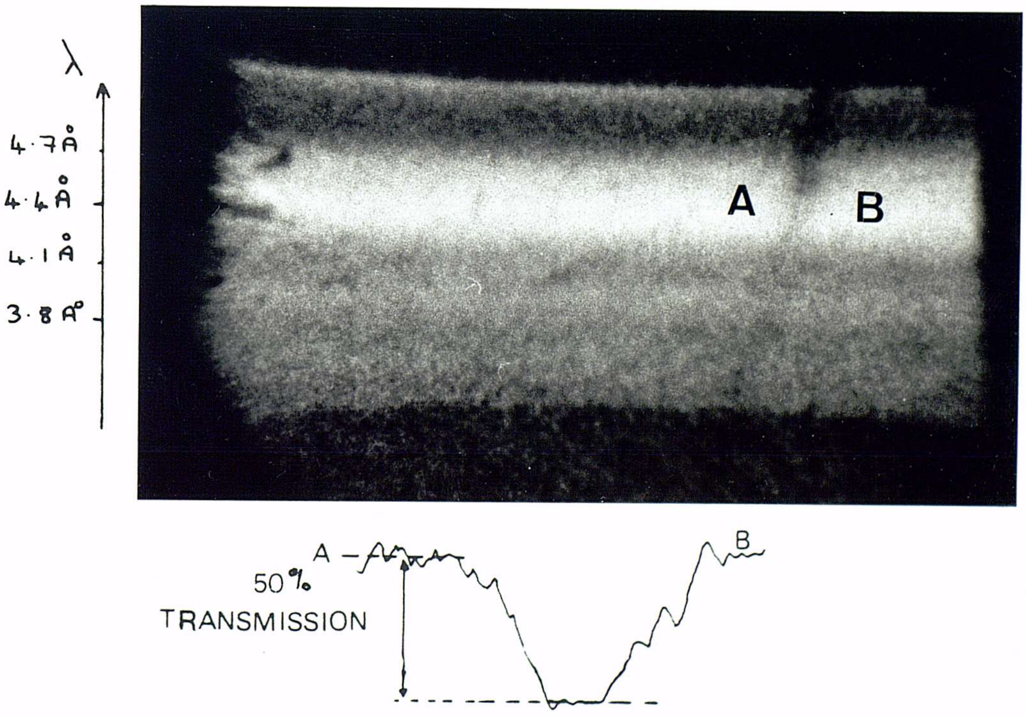

Fig(6.7) Shadowgraph of the irradiated plastic foil probed at 5ns after the start of the drive pulse.

a diameter of 10μm.

Fig(6.7) shows the image of a plastic $(CH)_n$ foil irradiated with 50 J and probed at 5 ns after the start of the drive pulse. From this picture we can gain some information about the relative magnitude of the self emission from the target. A densitometer tracing through the shadow of the foil in the centre of the Bi m band shows that the transmission is 50%. Now the self emission from the target will contribute a uniform background of light over the whole of the film. Let this background intensity be S, and the intensity of the backlight at 4.4Å be 1; then we have the equation

$$\frac{0.4 + S}{1 + S} = 0.50$$

i.e.

$$S = 0.2$$

i.e. the backlight is 5 times brighter than the self emission under these conditions. However this figure is very sensitive to the value of the transmission, and is therefore unlikely to be accurate.

However, as mentioned in section (4.1) the main problem encountered looking side on to a foil is that buckling of the foil may obscure what is happening at the ablation surface. One way of attempting to overcome this was to use the target design shown in Fig(6.8). Here the 10μm region of KCl absorbs 83 % of the light (the total absorption is 95 %) just above the Cl K edge at 4.4 Å. Thus

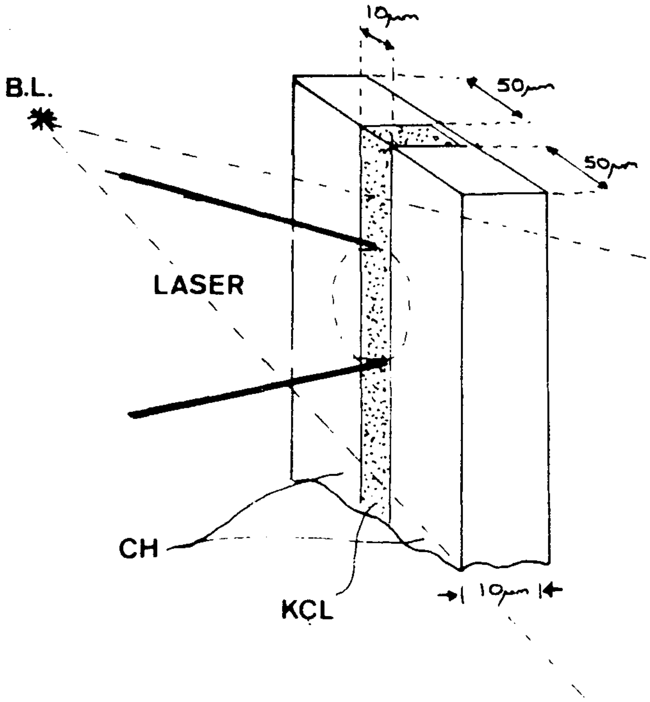

Fig(6.8) Target design for observing a thin absorbing region of the target.

over half of the m band of Bi the dominant contribution to the shadow will come from the thin KCl region, overcoming the difficulties mentioned above.

However, if such a target is irradiated there is a lot of emission from the Cl He like ions, totally wiping out the shadow of the target, as shown in Fig(6.9). The solution to this is to cover the front surface of the Chlorine doped target with a layer of $(CH)_n$ type plastic, thus keeping the self emission low but maintaining the thin absorbing region; and this essentially the experiment attempted at the Lawrence Livermore Laboratory, as described below.

6.9 The Livermore Experiment

A follow up experiment to that described above was carried out on the 'Phoenix' Laser system at the Lawrence Livermore National Laboratory. The basic principles were the same, but with the following modifications.

First a smaller backlighting wire was used (5μm) to see if this gave improved resolution. The smallest wire available was Tungsten; this was coated with Bismuth to increase the spread in wavelength over which x-rays were produced.

The target design for this experiment is shown in Fig(6.10). The low self emission ablator was 20μm of paraffin wax, and this covered a sandwich of chlorinated plastic between two layers of $(CH)_n$ plastic.

The diffracting crystal was Germanium (1,1,1) , 2d = 6.5Å. Instead of using a photocathode as a detector, Kodak

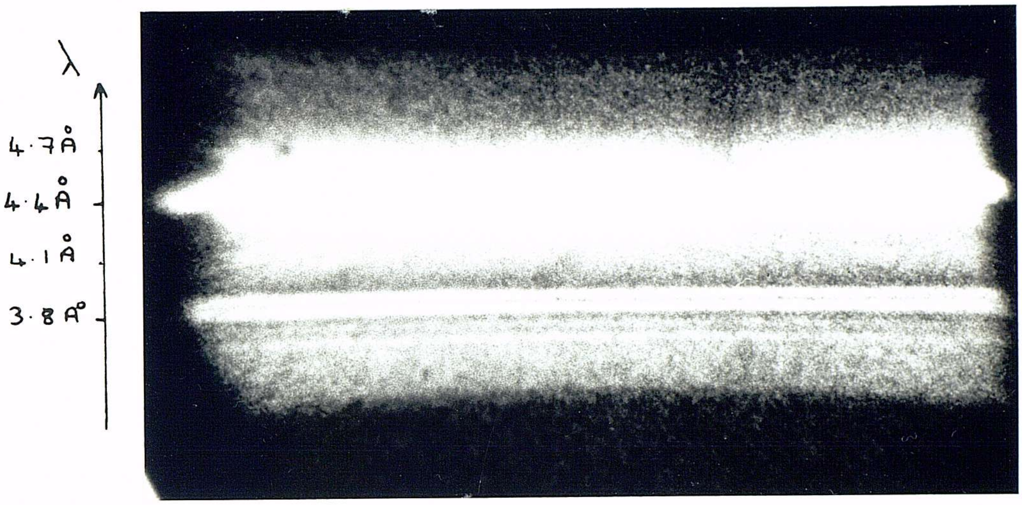

Fig(6.9) Shadowgraph of the irradiated target shown in Fig(6.8).

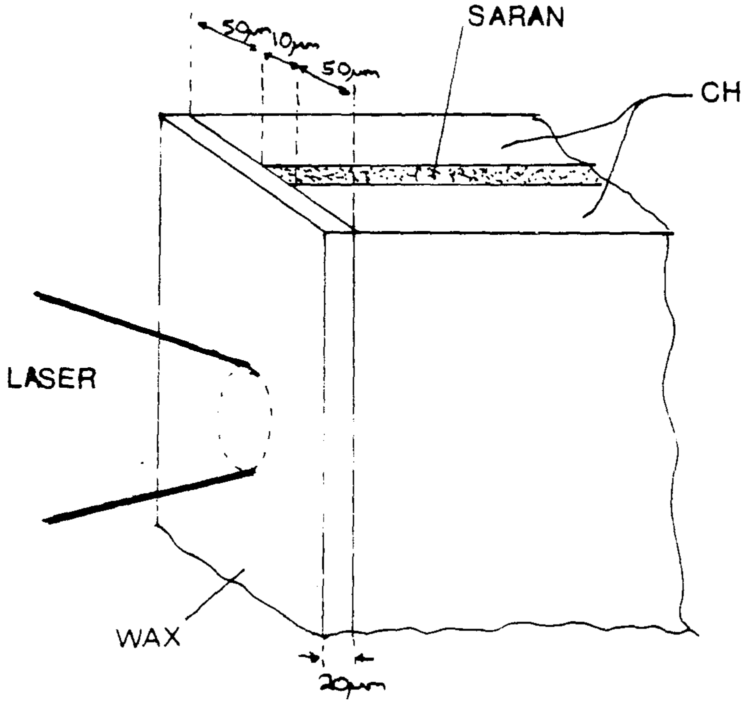

Fig(6.10) Target design for the Livermore experiment.

DEF x-ray film was used to reduce the noise level.

6.10 Illumination conditions

The drive beam was a 2ns pulse of 1.05μm light of energy 50 - 100 J on a spot diameter of 400μm. On the Phoenix system at the time of the experiment a short pulse backlight was not available; a 1ns pulse of 30 J of 0.53μm light was focused down to a spot of 20μm diameter. Although this length of backlight prevented good time resolution it still enabled an investigation of spatial resolution and relative self emission brightness to be performed.

6.11 Magnification

A plan view of the experiment is shown in Fig(6.11). The two beams enter from diametrically opposite points on the chamber. One of the problems encountered early on in the experiment was damage to the final green mirror due to the main drive beam passing out through the green beam entrance lens. To prevent this beam stops were placed behind the target and backlight. Due to the physical dimensions of the target this limited the maximum magnification to 12 by restraining the point source to target distance to 1cm. From section (6.3) we see that this causes resolution problems for irradiated targets due to x-ray refraction, and limits the resolution to 20μm.

6.12 Resolution of unirradiated targets

The resolution was measured by backlighting a grid of

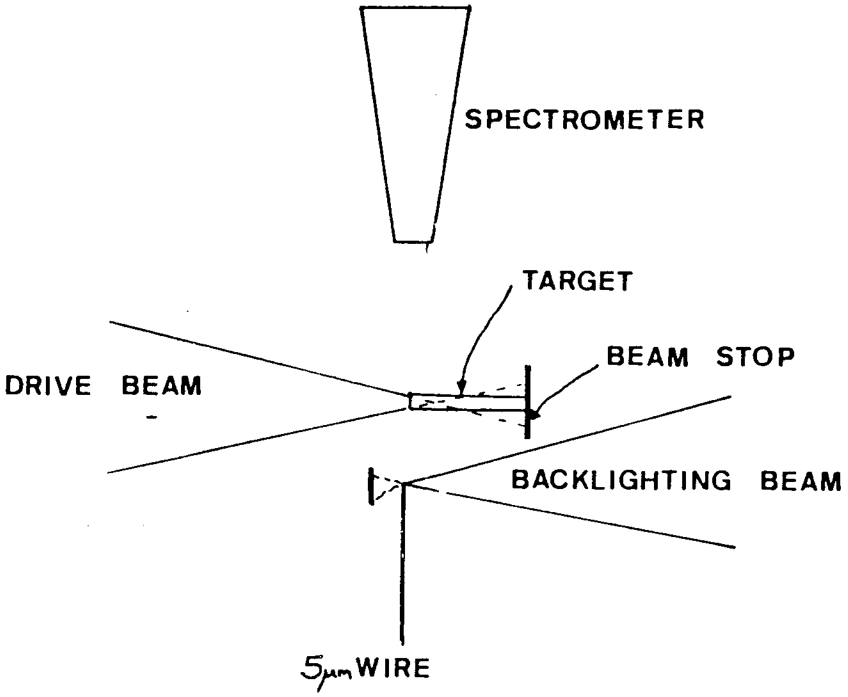

Fig(6.11) A plan view of the Livermore experiment.

20μm Molybdenum wires seperated by 125μm. The resolution grid is effectively black at the recorded wavelengths (10μm of Mo has a transmission of 10^{-11} at 4Å). The magnification on this shot varies in the spectral direction between 7 and 4.

The spectrum consists of lines and continuum. The lines are Tungsten lines and the continuum is due to the bands (or unresolved transitional arrays as they are known). The line widths on film are 80μm. The Stark, Doppler and crystal broadenings are negligible. Thus this broadening corresponds to a source size of 40μm (60^0 incidence angle on film). However the 20μm wires can clearly be seen on parts of the spectrum.

The reason is that the source size for the lines is greater than for the quasi continuum. The spectral lines around 4.4Å do not show the grid (see Fig(6.12), whereas the continuum close by does. Using an independently measured film calibration for DEF (6.7) we can calculate the resolution (defined at 50% transmission) for the continuum around 4.4Å; it is found to be 10μm, similar to that found in the RAL experiment.

6.13 Results

Fig(6.13) shows a picture of a backlit unirradiated target. The 20μm ablator is visible on the front surface of the target. There is a clear jump in the transmission of the target at the Cl K edge.

Targets were then irradiated as shown in Fig (6.14).

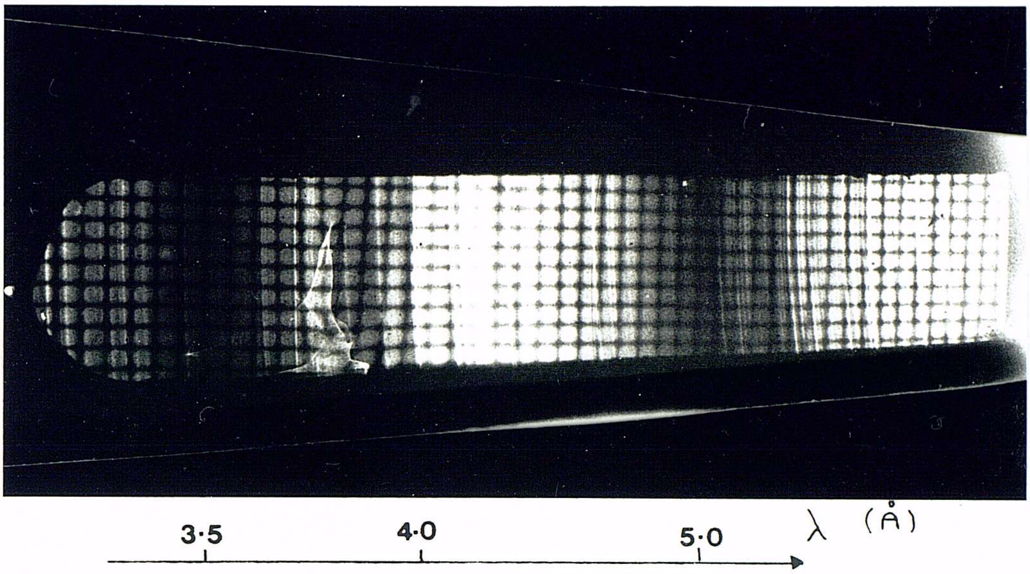

Fig(6.12) Shadowgraph of the grid in the Livermore experiment.

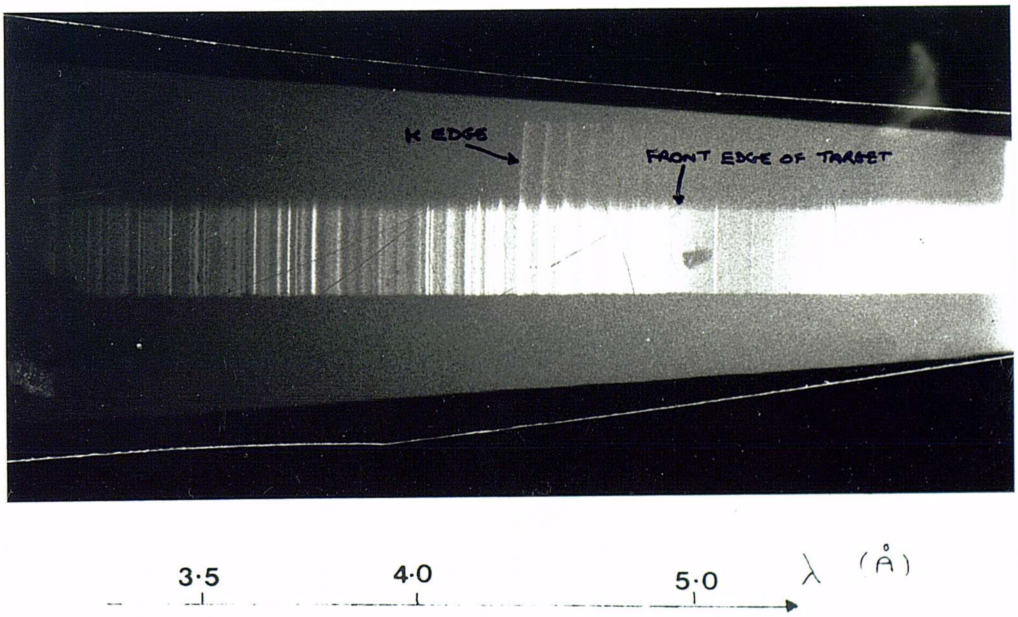

Fig(6.13) Backlit unirradiated target showing the absorption due to the Cl K edge.

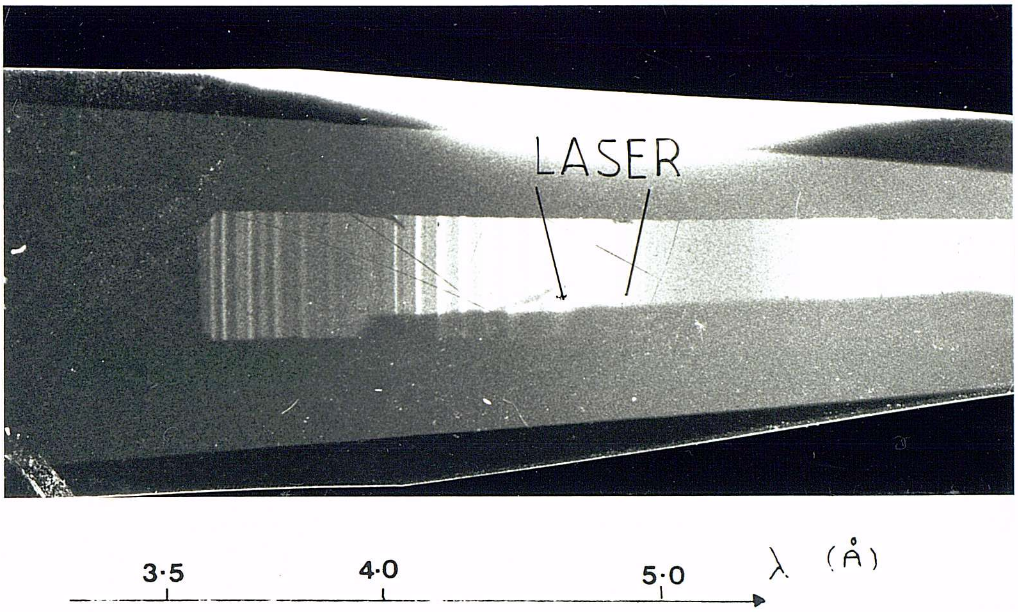

Fig(6.14) Irradiated target showing the effects of refraction of the x-rays.

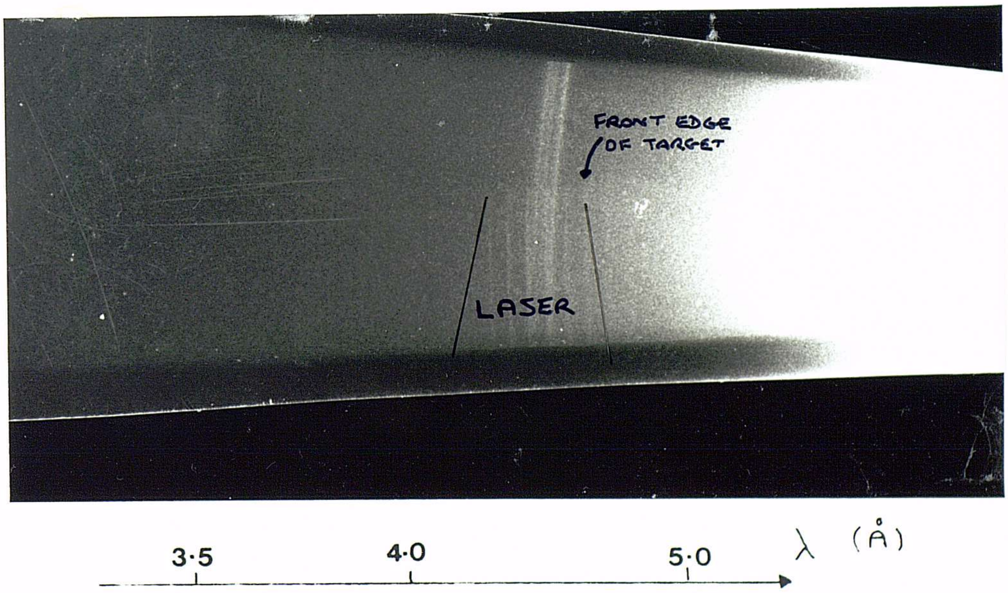

Fig(6.15) Irradiated target showing Cl emission lines.

It can be seen that the irradiated region has apparently move out towards the laser. This is the effect of the x-ray refraction, which makes an absorbing region with a large density gradient (i.e. close to the ablation surface) appear larger by refracting the x-rays down the density gradient. The observed expansion is 20μm, in good agreement with the predicted magnitude. Thus for good resolution, assuming constant target to detector distance, we must ensure the point source is close to the target, i.e. we need to work in the high magnification mode, as in the RAL experiment.

The relative intensity of the self emission was so low as to be immeasurable. The only sign was of Cl line emision on one shot, Fig(6.15); this could have been due to the paraffin wax ablator being melted by the 1.05μm alignment beam.

6.14 The backlighting spectrum

It can be seen from Figs(6.13) (6.14) and (6.15) that the backlighting spectrum consists mainly of Tungsten lines rather than the Bi band around the region of interest at 4.4Å. Presumably the wires were not coated with sufficient Bismuth and this will need to be investigated in future experiments.

6.15 Conclusions

These two experiments have shown that, using spectrally resolved point projection radiography, spatial resolutions as good as 5μm can be obtained, though the resolution can deteriorate to 10μm in the brightest parts of the m band of Bismuth. Irradiated targets have been backlit with 2.8 Kev x-rays and self emission is shown not to be a problem if the target is $(CH)_n$ plastic, or coated with $(CH)_n$ plastic. Uncoated targets containing Chlorine, a good absorber at this energy, emit too many x-rays to be shadowgraphed. It is shown that the source to target distance must be kept small (2mm) if the resolution due to x-ray refraction is not to exceed that due to the finite source size.

CHAPTER SEVEN

CONCLUSIONS AND SUGGESTIONS FOR FURTHER WORK

The work described in Chapter Two shows that for ablative compressions with six beam f/1 optics the best attainable uniformity is of order 25%, and occurs at a defocus of 4.5. The absorbed fraction at this defocus is 20% compared with 33% at obscuration for irradiances around $10^{14}Wcm^{-2}$. These results have already proved valuable in subsequent implosion experiments performed at the CLF. Comparison with theoretical models shows qualitative agreement in that they predict a minimum in non uniformity at defoci greater than obscuration; though the value of the defocus and absolute magnitude of the non uniformity are not in very good agreement. This is attributed to the fact that the models assume the electron density distribution is spherically symmetric, which is clearly not the case with non uniform energy deposition.

Further work should include a similar experiment on the 12 beam f/2.5 system that has recently come on line at the CLF. For accurate theoretical modelling a 2-D code with raytracing is needed, though the prospect of such a facility still seems some way off.

Chapter Three presents the results of ρr variations caused (unintentionally) by modulations in the beams driving the targets. The measured variations in ρr are less than those predicted from 2-D simulations, and this could be due to physical processes ignored in the code which could become important at the high intensity regions found in the ring structure.

Further work should include studies of the R-T instability instigated by controlled modulations in clean beams (i.e. similar experimental arrangements as for some thermal smoothing experiments, but with shorter wavelength modulations in the beam. Also this work shows the necessity of good quality final lenses.

The results presented in Chapter Four are the first pictures of the R-T instability in ablatively accelerated mass modulated microballoons. The growth rate is measured to be 0.6 of the classical, and a transmission shadowgraph has shown clear evidence of mass redistribution. Spherical effects are shown to be insufficient in explaining the larger growth rate than that measured by Cole et al; it is postulated that radiative preheat could have decompressed the target, and hence lower the growth rate, in his experiment.

This experiment gives rise to great scope for further work. Recent improvements in target manufacture now mean that mass modulated targets can be made with far lower amplitudes than those used in this thesis, so experiments can be performed for lower initial perturbations, eradicating complications due to secular growth. Also a full scan in perturbation wavelength is needed.

If improvements can be made in the length of the backlight, or in the use of diagnostics such as fast gated intensifiers(7.1) or framing cameras(7.2), then it may be possible to probe the instability further into the implosion to look for spherical effects.

As well as discussing the important experimental parameters involved in the technique, Chapter Five also includes the first results of laser accelerated targets backlit by fusion alpha particles. It is shown that this technique may act as a valuable complement to the study of R-T unstable planar targets due to the good temporal resolution obtainable, the accuracy in the measured $\Delta(\rho r)$ if low 10^{13} Wcm^{-2} irradiances are used, and its ability to detect small scalelength variations in ρr (although not resolve them).

It has been shown that the technique is experimentally feasable; i.e. laser accelerated targets have been backlit with alpha particles. The resultant residual range spectra showing that mass redistribution took place in both plane and corrugated accelerated foils, indicating the presence of the R-T instability.

The demonstration of such a novel technique obviously affords opportunities for much further work. A detailed study of both planar and mass modulated low Z targets, probing with alphas at different times, should be undertaken, as well as a study of the effects of clean and modulated beams. The spatial resolution should be quantified by backlighting unirradiated targets with large mass modulations of differing periodicity, and noting the smallest observable wavelength. The isotropy of the parent distribution should also be investigated to determine the limits it places on the accuracy of measurement of $\Delta(\rho r)$ in the foil.

Chapter Six reports on two preliminary experiments using point sources of X-rays to backlight laser irradiated targets with spectral resolution. It is shown that resolutions of order 5 - 10 μm can be obtained. Self emission is not a problem under the particular experimental conditions for $(CH)_n$ targets. The point source must be kept close to the target to minimise refraction effects.

The lessons learnt from the problems encountered in these two experiments should prove valuable in future point projection radiography experiments.

References.

Chapter One:

(1.1) J.L.Tuck, "Thermonuclear Reaction Rates", Los Alamos Scientific Laboratory Report LAMS-1640 (March 1954).

(1.2) W.B.Thompson, "Thermonuclear Reaction Rates", Proc. Phys. Soc. 70B, 1 (1957).

(1.3) J.D.Lawson, Proc. Phys. Soc. London, B70, 6 (1957).

(1.4) K.Boyer, Aero. & Astro. 28 (July 1973).

(1.5) J.L.Emmett, J.Nuckolls and L.Wood, Sci. Am. 231, 24 (June 1974).

(1.6) J.Nuckolls, J.L.Emmett and L.Wood, Physics Today, 46 (August 1976).

(1.7) T.J.Goldsack, J.D.Kilkenny, B.J.MacGowan, S.A.Veats, P.F.Cunningham, C.L.S.Lewis, M.H.Key, P.T.Rumsby and W.T.Toner, Opt. Comm. 42(1), 55 (1982).

(1.8) T.J.Goldsack, J.D.Kilkenny, B.J.MacGowan, P.F.Cunningham, C.L.S.Lewis, M.H.Key and P.T.Rumsby, Phys. Fluids, 25(9), 1634 (1982).

(1.9) Yaakobi et al, Opt. Comm. 39, 178 (1981).

(1.10) J.Grun, R.Decoste, B.H.Ripin and J.Gardener, Appl. Phys. Lett. 39, 545 (1981).

(1.11) T.W.Johnston and J.M.Dawson, Phys. Fluids 16(5), 722 (1973).

(1.12) K.G.Estabrook, E.J.Valeo and W.L.Kruer, Phys. Fluids 18, 1151 (1975).

(1.13) D.W.Forslund, J.M.Kindel, K.Lee, E.L.Lindman and R.L.Morse, Phys. Rev. A 11, 679 (1975).

(1.14) J.P.Friedberg, R.W.Mitchell, R.L.Morse and L.I.Rudinski, Phys. Rev. Lett. 28, 795 (1972).

(1.15) K.Estabrook and W.L.Kruer, Phys. Rev. Lett. 40, 42 (1978).

(1.16) D.W.Forslund, J.M.Kindel and K.Lee, Phys. Rev. Lett. 39, 284 (1977).

(1.17) J.D.Hares, Ph.d Thesis, University of London (1980).

(1.18) R.G.Evans, A.J.Bennet and G.J.Pert, J.Phys D 15, 1673 (1982).

(1.19) J.H.Gardner and S.E.Bodner, Phys. Rev. Lett. 47, 1137 (1981).

(1.20) A.J.Cole, J.D.Kilkenny, P.T.Rumsby, R.G.Evans and M.H.Key, J.Phys.D. 15, 1689 (1982).

Chapter Two:

(2.1) I.N.Ross, J.Phys.D 16, 1245 (1983).

(2.2) P.T.Rumsby, RAL Annual Report to the Laser Facility Committee, RL-80-026 (1980).

(2.3) LLE Review, Volume 10, University of Rochester (1982).

(2.4) C.M.Dozier et al, J.Appl.Phys. 47, 3732 (1976).

(2.5) C.L.S.Lewis et al, RAL Annual Report to the Laser Facility Committee, RL-84-049 (1984).

(2.6) A.R.Bell and D.J.Nicholas, Rutherford Appleton Laboratory Report, RL-83-127 (1983).

(2.7) J.Dawson, P.Kaw and B.Green, Phys. Fluids 12, 875 (1969).

(2.8) M.Born and E.Wolf, "Principles of Optics", Oxford Pergamon Press (1975).

(2.9) P.Gottfeldt, RAL Annual Report to the Laser Facility Committee, RL-82-039 (1982).

(2.10) R.G.Evans, Private Communication (1984).

(2.11) B.J.MacGowan, Ph.d Thesis, University of London (1982).

Chapter Three:

(3.1) Lord Rayleigh,"Theory of Sound", Dover, New York, 2nd ed., Vol. 2 (1945).

(3.2) G.Taylor, Proc. Roy. Soc. (London) Ser. A, 201, 192 (1950).

(3.3) Chandrasekhar,"Hydrodynamic and Hydromagnetic Stability", Oxford University Press (1961).

(3.4) B.Daly, Phys. Fluids 10, 297 (1967).

(3.5) W.Crowley, Lawrence Livermore Report UCRL-72650 (1970).

(3.6) D.Youngs, Proceedings of Fronts and Interfaces, LANL (1983).

(3.7) J.Nuckolls, L.Wood, A.Thiessen and G.Zimmerman, Nature 239, 139 (1972).

(3.8) R.McCrory, L.Montierth, R.Morse and C.Verdon, Phys. Rev. Lett. 46, 336 (1981).

(3.9) J.D.Lindl and W.C.Mead, Phys. Rev. Lett. 34, 1273 (1975).

(3.10) K.O.Mikaelian, Phys. Rev. Lett. 48, 1365 (1982).

(3.11) W.Manheimer, D.Colombant and J.Gardner, Phys. Fluids 25, 1644 (1982).

(3.12) D.Colombant and W.Manheimer, Phys. Fluids 26, 3127 (1983).

(3.13) W.Manheimer and D.Colombant, Phys. Fluids 27, 983 (1984).

(3.14) H.Helmholtz (translation by J.A.Barth) Phil. Mag. Ser. 4 36, 337 (1868).

(3.15) Lord Kelvin, "Hydrodynamics and General Dynamics", Cambridge, England (1910).

(3.16) M.Emery, J.Gardner and J.Boris, Phys. Rev. Lett. 48, 677 (1982).

(3.17) S.Obenschain, J.Grun, B.Ripin and E.McLean, Phys. Rev. Lett. 46, 1402 (1981).

(3.18) M.Key, P.Rumsby, R.Evans, C.Lewis, J.Ward and R.Cooke, Phys. Rev. Lett. 45, 1801 (1980).

(3.19) J.D.Kilkenny, J.Hares, C.Lewis and P.Rumsby, J. Phys. D: Appl. Phys., 13, 1123 (1980).

(3.20) A.J.Cole, J.D.Kilkenny, P.T.Rumsby, R.G.Evans, C.J.Hooker and M.H.Key, Nature 299, 329 (1982).

(3.21) R.R.Whitlock et al, Phys. Rev. Lett. 52, 819 (1984).

(3.22) J.Grun et al, Phys. Rev. Lett. 53, 1352 (1984).

(3.23) P.T.Rumsby et al, Rutherford Appleton Laboratory Annual Report to the Laser Facility Committee, RL-83-043, 3-19 (1983).

(3.24) R.Eason, Private Communication (1984).

(3.25) R.G.Evans, A.J.Bennett and G.J.Pert, Phys. Rev. Lett. 49, 1639 (1982).

(3.26) G.J.Pert, J. Comp. Phys. 43, 111 (1981).

Chapter Five:

(5.1) W.Toner, Private Communication (1984).

(5.2) B.G.Cartwright, E.K.Shirk and P.B.Price, Nucl. Instr. and Meth. 153, 457 (1978).

(5.3) A.P.Fews, Ph.d Thesis, University of Bristol

(5.4) A.P.Fews and D.L.Henshaw, Nucl. Instr. and Meth. 197, 517 (1982).

(5.5) A.P.Fews et al, RAL Annual Report to the Laser Facility Committee, RL-82-039 (1982).

(5.6) A.P.Fews et al, RAL Annual Report to the Laser Facility Committee, RL-84-049 (1984).

(5.7) A.P.Fews et al, RAL Annual Report to the Laser Facility Committee, RL-83-043 (1983).

(5.8) W.T.Scott, Rev. Mod. Phys. 35, 231 (1963).

(5.9) S.J.Rose, Private Communication (1985).

Chapter six:

(6.1) M.Miyanaga, Y.Kato and C.Yamanaka, Appl. Phys. Lett. 42, 160 (1983).

(6.2) N.Miyanaga, Y.Kato and C.Yamanaka, Opt. Comm. 44, 48 (1982).

(6.3) R.Bennattar and J.Godart, Opt. Comm. 49, 43 (1984).

(6.4) C.L.S.Lewis et al, RAL Annual Report to the Laser Facility Committee, RL-84-049 (1984).

(6.5) M.H.Key, Private Communication (1985).

(6.6) A.J.Cole, Private Communication (1983).

(6.7) P.Rockett and C.R.Bird, KMS Fusion internal report (1984).

Chapter Seven

(7.1) A.Dymoke-Bradshaw et al, Annual Report to the Laser Facility Committee, RL-81-040 (1981).

(7.2) T.A.Hall et al, Annual Report to the Laser Facility Committee, RL-83-043 (1983).